List of symbols:

a_E , a_W and a_P : Coefficients defined on finite volume method

C : Air concentration

C_μ : Constant of k -ε turbulence models

$C_{\varepsilon 1}$ and $C_{\varepsilon 2}$: Constants of k -ε turbulence models

C_{mean} : Mean air concentration

d : Clear- water depth

D : Diffusion conductance at cell faces

D_H : Hydraulic diameter

D' : dimensionless turbulent diffusivity

D_0 : Constant and is function of mean air concentration

d_{ab} : air bubble diameter

d_i : Flow depth at the inception point

h : Flow depth of water flow inlet

H_{dam} : Elevation of the dam crest above the dam toe

H_{max} : maximum upstream head

H_{res} : residual head at the downstream end of the channel

H_0 : elevation of the free surface above the dam crest

F : convective mass flux per unit area at cell faces

f_e : Friction factor of air-water flows

f_{drag} : The drag function

F^* : Froude number defined in terms of the roughness height

Fr_0 : Froude number upstream of the drop

g : Gravitational constant

G_k : Production of turbulent kinetic energy

h : Step height

I : Turbulence intensity

k : Turbulence kinetic energy

K : Dimensionless function of mean air concentration

K' : dimensionless integration constant

K'' dimensionless integration constant

k_s : Surface roughness

l : Length of step

L_d : Drop length of a free-falling, ventilated nappe

L_i : Observed distance from the crest spillway to the inception point

L_{i*} : Calculated distance from the crest spillway to the inception point

L_{i**} : Computed distance from the crest spillway to the inception point

L_r : Roller length of hydraulic jump

N : Number of step

n : Exponent of power law

P : Pressure

P_e : Peclet number

q : Unit discharge

Re : Reynolds number

S : Modulus of strain tensor

S_{ij} : Strain tensor

S_ϕ : Source term

U_{avg} : Mean velocity of water flow inlet

u_i : Velocity components

u_j : Velocity components

u_m : Velocity of mixture

u_{qk} : Slip velocity between air and water

u_k : Velocity of phase k

$\overline{u_i' u_j'}$: Reynolds stresses

u_r : Bubble rise velocity

u_τ : Friction velocity

v' : Turbulent velocity normal to the free surface

V : Velocity of flow

V_k : Volume of phase k

V_{max} : Maximum velocity of flow

V_{90} : Characteristic velocity at $y=Y_{90}$

x : streamwise distance from the start of the growth of the boundary layer
x_i : Coordinate components
x_j : Coordinate components
y : transverse coordinate originating at the pseudo-bottom
y_b : Flow depth at end of step
y_c : critical flow depth
y_0 : Flow depth upstream of the drop
y_1 : flow depth downstream of the jet impact
y_2 : flow depth downstream of the hydraulic jump
y_p : pool depth
Y_{90} : characteristic distance where $C = 90\%$
y^+ : Wall function

Greek symbols

α_a : Volume fraction of air
α_k : Volume fraction of phase k
α_w : Volume fraction of water
δ : Boundary layer thickness
ρ : density
ρ_a : Density of air
ρ_k : Density of phase k
ρ_w : Density of water
ρ_m : Density of mixture
σ : Surface tension
σ_k and σ_ε : turbulence Prandtl numbers for k -ε turbulence models
θ : Slope channel
λ : Dimensionless function of mean air concentration
ν : Kinematic viscosity
μ : Molecular viscosity
μ_a : Dynamic viscosity of air

μ_w : Dynamic viscosity of water

$\mu_{eff.m}$: Effective viscosity of mixture

μ_{eff} : effective viscosity

μ_t : Turbulent viscosity

ε : Turbulence dissipation rate energy

ω : Specific dissipation rate

Γ : Diffusivity

ϕ : Scalar transport

δ_{ij} : Kronecker delta

κ : Constant of Von karman

ΔH : Total head loss

List of abbreviations

CFD : computational fluid dynamics

DNS : Direct numerical simulation

EVMs : Eddy-Viscosity Models

FVM : Finite volume method

LES : Large eddy simulation

NA1 : nappe flow with fully developed hydraulic jump

NA2 : nappe flow with partially developed hydraulic jump

MMF : Mixture multiphase flows

NA3 : nappe flow without hydraulic jump

QUICK : Quadratic upstream interpolation for convective kinetics

RANS : Reynolds-averaged Navier-Stokes

RSMs : Reynolds-Stress Models

TRA1 : Sub-regime of transition flow

TRA2 : Sub-regime of transition flow

VOF : Volume of fluid

RNG : Re-normalisation group k-ε Model

SST : Shear-Stress Transport k-ω model

TSTE : Taylor series truncation error

List of figures

List of tables

Table of contents

Chapter I: Bibliographic review

Chapter II: Numerical modelling of multiphase flow

Chapter III: Numerical simulation of flow over stepped spillways with uniform step height

Chapter IV: Numerical simulation of flow over stepped spillways with non uniform step height

References

Energy dissipation over dam spillways is usually achieved by a standard stilling basin at the downstream end of the spillway where a hydraulic jump is created to dissipate a large amount of energy in supercritical flow. Water flowing over a stepped chute can dissipate a major proportion of its energy. A stepped spillway is a modified chute spillway, in which the surface of spillway is provided with a series of steps from near the crest to the toe of the structure. The steps act as large rough elements which increase the air entrainment, the flow resistance and the energy dissipation significantly. The size of the downstream stilling basin can be reduced and the construction is cheaper (Rajaratnam, 1990 and Christodoulou, 1993). In addition, the cavitation risk is minimised due to the large amount of entrained air. Stepped spillways have become a popular method for flood releases at roller compacted concrete (RCC) dams and gabions dams. The compatibility of the stepped spillway design with RCC construction techniques results in low additional cost for the spillway.

A large number of studies demonstrate that the flow over stepped spillway can be divided into three flow regimes, i.e. nappe flow, transition flow and skimming flow regimes with increasing discharge. The changes between flow regimes depend on the spillway configuration including the channel slope, the step height and the discharge. In nappe flow, usually found on large steps or at low discharges, a free-falling jet impacts from step to step with a fully aerated nappe cavity. Skimming flows occur on small steps or at high discharges. The transition occurs at discharges higher than the maximum required for nappe flow but lower than for the onset of skimming flow (hanson 1994b and Ohtsu, and Yasuda, 1997).

For practical engineering purposes, skimming flows are more relevant than nappe flows.

At the upstream end of skimming flows over stepped spillways, the water surface is rather smooth without air entrainment. The boundary layer thickness is less than the flow depth and this zone is called the ‘non-aerated zone’. The boundary layer develops and reaches the flow depth after a few steps at a location called the inception point. Downstream of the inception point, flow is rapidly aerated. The free surface becomes wavy with significant air entrainment in this zone, called the ‘aerated zone’.

Historically, very active experimental research has been done on the air-water flow over stepped spillways, such as flow patterns, inception of air entrainment, air concentration profile, velocity distribution, pressure field and energy dissipation. The engineers have normally investigated the flow through laboratory experiments on scaled down models of spillways. The complexity of the flow structure which includes complicated boundary conditions, the curved free surface, and the unknown scale effects has caused uncertainties in transposing the experimental results to prototype scales. With the development of computational fluid dynamics (CFD) and high-performance computers, complex multiphase flows can be simulated numerically and with validation the results can be trusted to be reliable. Given reduced time demand and lower cost of the numerical method than physical experiments, simulation of the stepped spillway overflow has a significant advantage (Benmamar et *al*, 2003; Bombardelli et *al* 2010;Chen et *al* 2002...etc).

The present study is to model the complex flow pattern of two-phase turbulence flow in stepped spillways by using Fluent computational fluid dynamics. The objectives of this work can be listed as follows:

1. To investigate the effects of different discharges on the flow regimes at stepped spillways;
2. To evaluate the effect step height on the position of inception point and to validate the relationships developed by researchers for determining the distance from the spillway crest to the inception point;
3. To assess the effects of non-uniform step heights on the air-water flow properties down a stepped chute;
4. To present pressure contours and velocity vectors at the bed surface;
5. To determine the law of velocity profile and air concentration distribution.

In order to discuss the basics of the stepped weir problem, the present thesis is divided into a four chapters, chapter one starts with a detailed review of flow over stepped cascades and gives the literature survey of previous experimental and numerical work. In second chapter different tools such as turbulence models, multiphase models, numerical schemes and other options of the Fluent for modelling multiphase flow are presented. The results of numerical simulation flow in stepped spillway with uniform step height and non uniform step height are discussed in chapter three and four. The experimental data from the physical models of Hunt and kadavy (2009), Chanson and Toombes (2001) and Stephan Felder (2013) were chosen to verify the found numerical results. Finally, summary of the work are presented in conclusion.

Introduction

The stepped spillway finds its extensive applications in hydraulic and environmental engineering, which is used to dissipate the energy of released flood and also to be a landscape structure. This chapter describes the basic hydraulic characteristics of stepped spillways such as flow regime, mechanism of air entrainment, energy dissipation and also presents some results of experimental and numerical studies of flow over stepped spillways.

I.1 Stepped spillway

A stepped spillway is a modified chute spillway, in which the surface of spillway is provided with a series of steps from near the crest to the toe of the structure. The steps may be horizontal, inclined upward or downward, or pooled as shown in Figure I-1. If a uniform step geometry is employed then the overall slope of the channel is given by:

$$\tan\theta = \frac{h}{l}$$

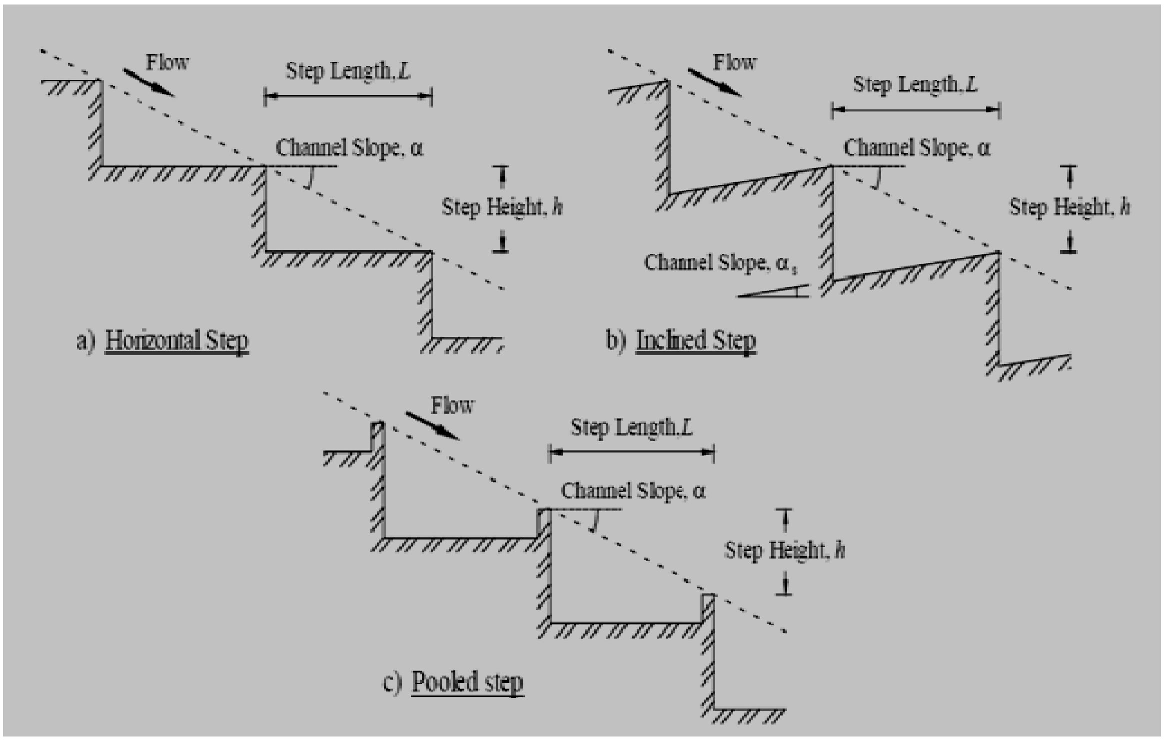

Figure I.1: Stepped cascade geometry (Toombes, 2002)

Dissipation of energy is caused by the steps. The steps act as small drops placed in series and each step acts as small stilling basin for the preceding step. This method of dissipation of energy either eliminates the requirement for stilling basin at the toe or considerably reduces the size of the stilling basin (figure I.2) (Dermawan and Legono, 2011, Gonzalez, and Chanson, 2007).

A:Stepped spillway of the Opuha embankment dam

B: Melton dam secondary spillway (Australia)

Figure I.2: stepped spillway without stilling basin (Gonzalez and Chanson, 2007)

Stepped spillways have regained popularity over the last two decades, thanks to financial benefits resulting mainly from the simple economic and the rapid construction procedure especially with the Roller Compacted Concrete (RCC) construction method.

I.2 Flow regime

A stepped chute consists of an open channel with a series of drops in the invert. For a given geometry, the flows on stepped spillways can be divided into different flow regimes, i.e. nappe flow, transition flow and skimming flow regimes with increasing discharge. The changes between flow regimes depend on the spillway configuration including the channel slope, the step height and the discharge (Felder, 2013).

I.2.1 Nappe flow

The nappe flow regime is defined as a succession of free-falling nappes. The flowing water bounces from one step to the next as a series of small free falls. Three types of nappe flow can be distinguished and presented in figure I.3: nappe flow with fully developed hydraulic jump (NA1) at low flow rates, nappe flow with partially developed hydraulic jump (NA2), and nappe flow without hydraulic jump (NA3) (Chanson, 2001).

Nappe flow on horizontal steps and inclined upward steps are characterised often by the presence of hydraulic jump (sub-regimes NA1 and NA2). Nappe flow with hydraulic jump are characterised by the occurrence of critical flow conditions at each step edge. Considering a horizontal step, the flow conditions near the end of the step change from subcritical to supercritical next the brink of the step. At the brink the pressure distribution departs from the hydrostatic pressure distribution and the flow depth y_b equals:

$$y_b = 0.715\, y_c \qquad (I-1)$$

where y_c is the critical flow depth.

Application of the equations of motion to the flow at the end of the step determines the drop length of a free-falling, ventilated nappe, L_d, from a step of height, h, as:

$$\frac{L_d}{h} = \left(\frac{y_c}{h}\right)^{(2/3)} \sqrt{\frac{h}{y_b}} \sqrt{1 + 2\frac{h}{y_b}} \qquad (I-2)$$

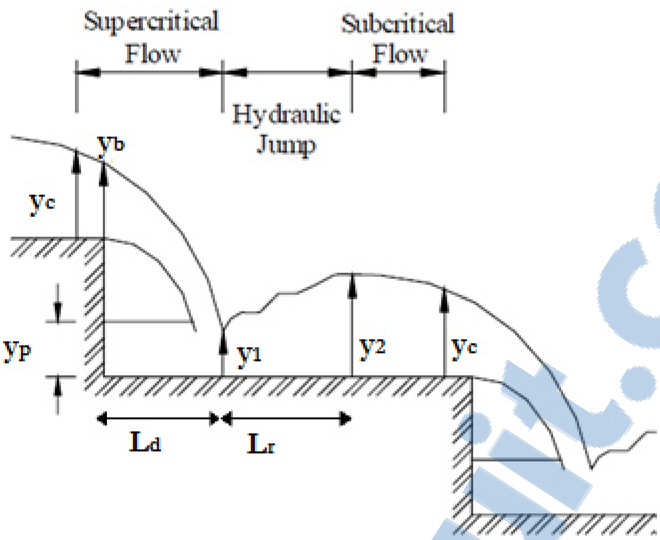

(a) Fully-developed Hydraulic Jump (NA1)

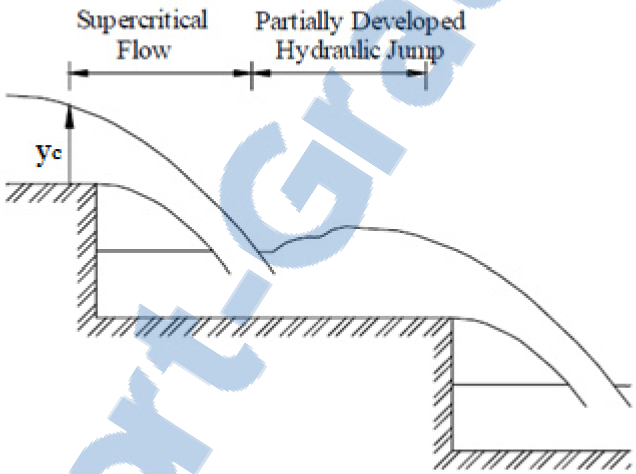

(b) Partially-developed Hydraulic Jump (NA2)

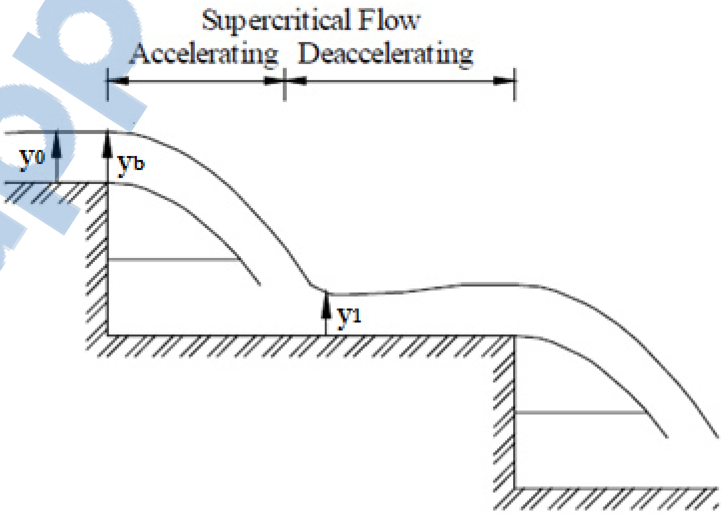

(c) No Hydraulic Jump (NA3)

Figure I.3: Nappe flow regimes on a stepped cascade (Toombes , 2002)

Downstream of nappe impact, the roller length of fully-developed hydraulic jump may be estimated as (Chanson, 2001):

$$\frac{L_r}{y_1} = 8\left(\left(\frac{y_c}{y_1}\right)^{3/2} - 1.5\right) \qquad (I-3)$$

The momentum equation was developed by White (in Chanson, 2001) to estimate the energy loss at the base of an over fall. His results gave the flow depth downstream of the jet impact, y_1, as:

$$\frac{y_1}{y_c} = \frac{2}{\frac{3}{2} + \sqrt{2\frac{h}{y_c} + 3}} \qquad (I-4)$$

The flow depth downstream of the hydraulic jump, y_2, is calculated by applying the continuity and momentum equations across the jump. Neglecting bed and wall friction, for a horizontal step, this yields:

$$\frac{y_2}{y_1} = \frac{1}{2}\left(\sqrt{1 + 8\left(\frac{y_c}{y_1}\right)^3} - 1\right) \qquad (I-5)$$

At the nappe impact, a force is required to divert the jet from its impact angle to a direction parallel to the step invert. This is applied in the form of a reaction force from the invert and a pressure from the pool of water beneath the falling nappe. The momentum equation was developed by Moore (in Chanson, 2001) to yield, y_p, as:

$$\frac{y_p}{y_c} = \sqrt{\left(\frac{y_1}{y_c}\right)^2 + 2\left(\frac{y_c}{y_1}\right) - 3} \qquad (I-6)$$

Rand (in Chanson, 2001) reanalysed several experiments to yield the following empirical correlations for flow with an aerated nappe:

$$\frac{y_1}{h} = 0.54\left(\frac{y_c}{h}\right)^{1.275} \qquad (I-7)$$

$$\frac{y_2}{h} = 1.66\left(\frac{y_c}{h}\right)^{0.81} \qquad (I-8)$$

$$\frac{y_p}{h} = \left(\frac{y_c}{h}\right)^{0.66} \qquad (I-9)$$

$$\frac{L_d}{h} = 4.30\left(\frac{y_c}{h}\right)^{0.81} \qquad (I-10)$$

For flat horizontal steps, Chanson (1994 a) developed a condition for nappe flow regime with fully developed hydraulic jump based upon the drop length and hydraulic jump length:

$$\left(\frac{y_c}{h}\right) < 0.0916\left(\frac{h}{l}\right)^{-1.276} \qquad (I-11)$$

In the sub-regime NA2, the hydraulic jump roller is greater than the length of the step then a fully developed hydraulic jump cannot form on the step. The hydraulic jump that does form may be classified as partially developed. Peyras et *al*. (1992) suggested that equations (I.1) to (I.9) were developed for Nappe Flow Regime with fully developed hydraulic jump (NA1) could also be applied to nappe flows with partially developed hydraulic jumps with reasonable accuracy.

In a nappe flow without hydraulic jump, the flow is basically supercritical at any point. Crtitical flow conditions are not observed at the step brink. Application of the Momentum Equation to the flow upstream of the drop for supercritical flow yields (Toombes, 2002):

$$1 + 2Fr_0^2 = \sqrt{2}\,Fr_0\left(\sqrt{\frac{1 + Fr_0^2}{2 - y_b/y_0}} + \sqrt{\frac{1 + Fr_0^2}{2}}\right) \qquad (I-12)$$

where y_0 and Fr_0 are the depth and Froude number upstream of the drop.
Hager (1983) suggested equation (I-13) as an acceptable approximation, with a deviation of at most 1%.

$$\frac{y_b}{y_0} = \frac{Fr_0^2}{Fr_0^2 + \frac{4}{9}} \qquad (I-13)$$

I.2.2 Transition flow

For a given chute geometry, low discharges flowed down the chute as a succession of clear, distinct free-falling nappes. For an intermediate range of flow rates, a transition flow regime is observed. The transition flows is characterized by a pool of recirculating waters and often a very small air cavity, and significant spray and water deflection immediately downstream of inception point. Ohtsu and Yasuda (1997) were the first to mention the existence of a distinct "transition flow" regime (between nappe and skimming flows).

The transition flows can be divided into two types of transition flows (Chanson, and Toombes,2004): sub-regime TRA1 and sub-regime TRA2.

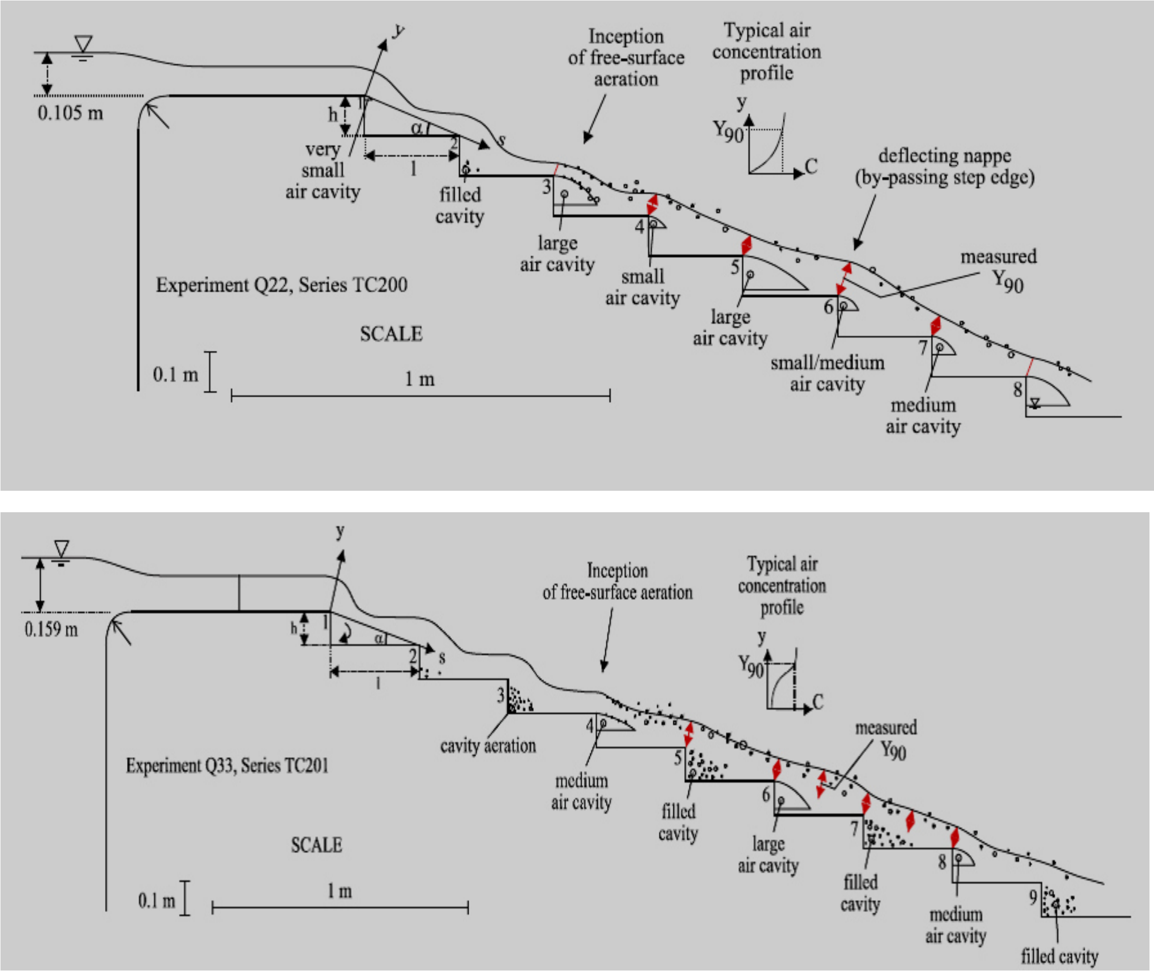

Figure I.4: Longitudinal free-surface profiles and air cavities in transition flows, Top: sub-regime TRA1, Bottom: sub-regime TRA2 (Chanson and Toombes,2004)

In the lower range of transition flows (sub-regime TRA1), the longitudinal flow pattern was characterised by an irregular alternance of small to large air cavities downstream of the inception point of free-surface aeration (Fig. I.4, top). For example, a small air cavity could be observed followed by a larger nappe cavity at the downstream step, then a smaller one. In the upper range of transition flow rates (sub-regime TRA2), the longitudinal flow pattern was characterised by an irregular alternance of air cavities (small to medium) and filled cavities (Fig. I.4 bottom).

In transitions flows, air–water velocity profiles exhibited flat distributions at step edges. Chanson and Toombes (2004) proposed formulae from experiment for two chute slopes: θ = 15.9° and 21.8°:

$$\frac{V}{V_{max}} \sim 0.8 + 0.1\left(\frac{y}{Y_{90}}\right) \quad \text{sub} - \text{regime TRA1} \ (y/Y_{90} < 2) \qquad (I-14)$$

$$\frac{V}{V_{max}} \sim 0.95\left(\frac{y}{Y_{90}} + 0.3\right)^{0.07} \quad \text{sub} - \text{regime TRA2} \ (y/Y_{90} < 1.6) \qquad (I-15)$$

Where y is distance measured normal to the pseudo-invert (Figure. I.5), Y_{90} is the characteristic distance where C = 90%,

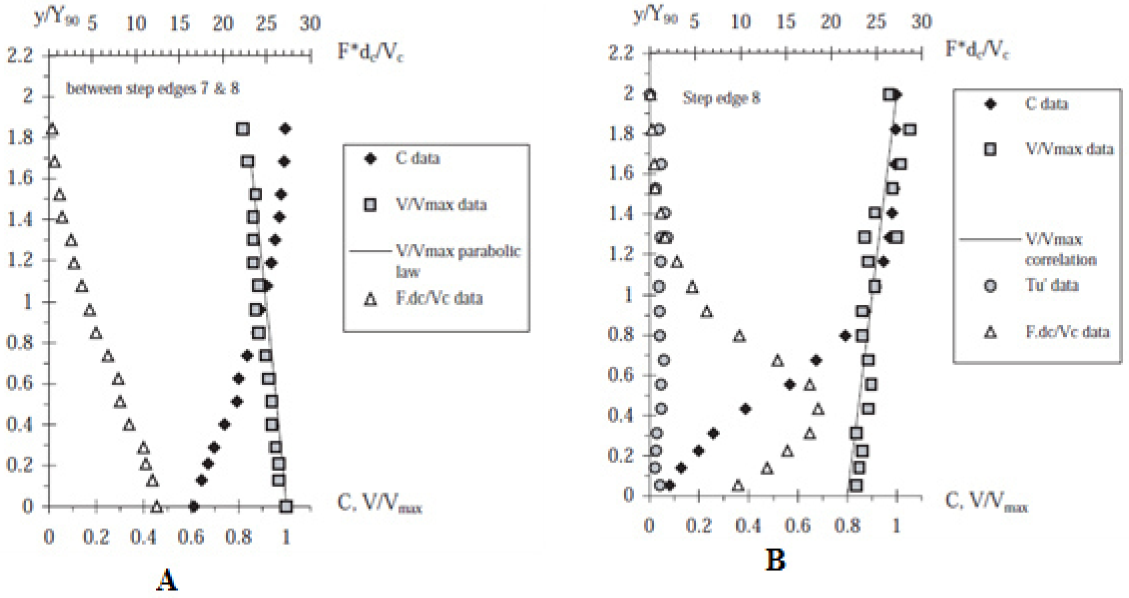

Figure I.5: Velocity profile in transition flows, A: sub-regime TRA1, B: sub-regime TRA2 (Chanson, and Toombes,2004)

Chanson and Toombes (2004) presented two equations which showed the lower and upper limits of transition flows (figure 1.6):

$$\frac{y_c}{h} > 0.9174 - 0.381\frac{h}{l} \qquad \text{Lower limit} \ (0 < h/l < 1.7) \qquad (I-15)$$

$$\frac{y_c}{h} < \frac{0.9821}{\left(\frac{h}{l} + 0.388\right)^{0.384}} \qquad \text{Upper limit} \ (0 < h/l < 1.5) \qquad (I-16)$$

From the study of Ohtsu and Yasuda (1997), two empirical equations able to evaluate the upper limit for the nappe flow regime and the lower limit for the skimming flow regime were defined, respectively, as follows;

$$\frac{y_c}{h} = \frac{1}{\left[0.57\left(\frac{h}{l}\right)^3 + 1.3\right]} \qquad (I-17)$$

$$\frac{y_c}{h} = 0.862\left(\frac{h}{l}\right)^{-0.165} \qquad (I-18)$$

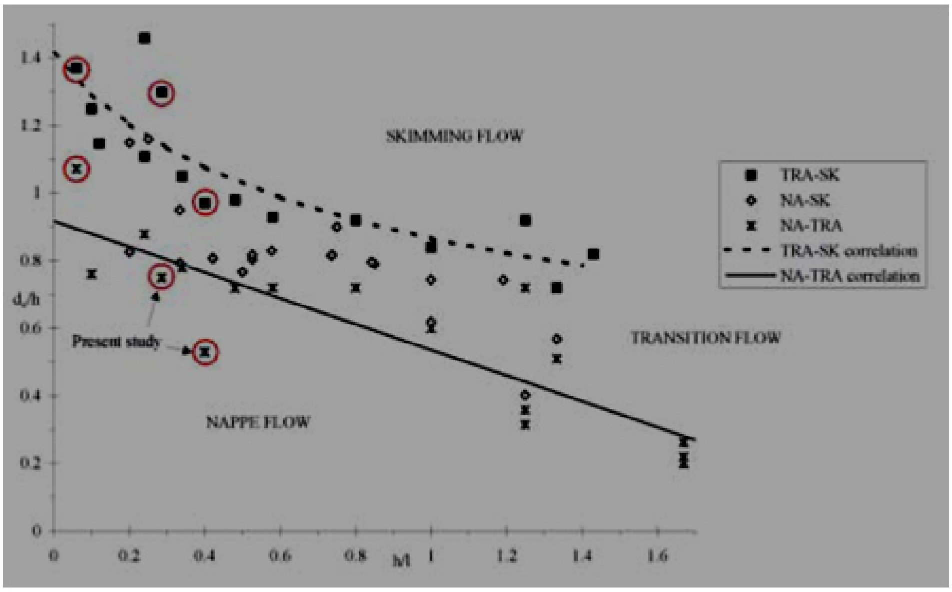

Figure I.6: Experimental observations of lower and upper limits of transition flows – Comparison with Eqs. (I.15) and (I.16) (Chanson, and Toombes,2004)

I.2.3Skimming flow

In the skimming flow regime, the external edges of the steps form a pseudo-bottom over which the flows pass. Beneath this, horizontal axis vortices develop, filling the zone between the main flow and the step (Fig. I.7).

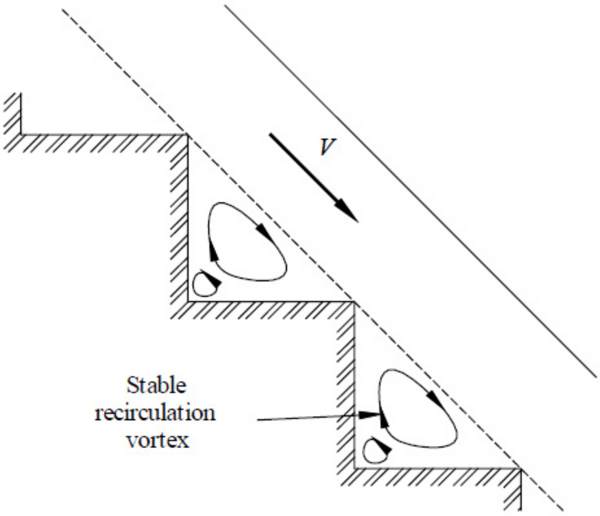

Figure I.7: Skimming flow regime

These vortices are maintained through the transmission of shear stress from the fluid flowing past the edges of the steps. In addition small-scale vorticity will be generated continuously at the corner of the steps.

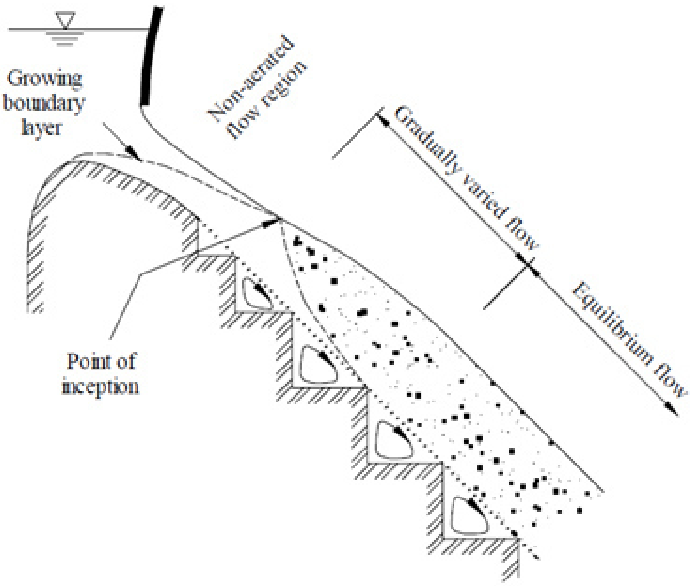

Figure I.8: Flow regions typical of skimming flow (Toombes , 2002)

Flow over the cascade is highly turbulent. The turbulent boundary layer grows from the start of the upstream channel (see Figure I.8). As the boundary layer nears the free surface, the turbulence initiates natural free-surface aeration, caused by turbulent velocities acting normal to the air-water boundary. The location where the boundary layer reaches the free surface is called the Point of Inception (Chanson,1994b and 1997; Keller and Rastogi, 1977). The flow is smooth and glassy upstream of the point of inception. Downstream, a layer containing an air-water mixture forms, increasing in thickness with distance from the point of inception. The flow eventually becomes approximately uniform, with the air concentration and velocity distribution on each step identical to adjacent steps (although not necessarily constant along the step). This region is called the Equilibrium Flow Region.

In the developing flow region, the flow consists of a turbulent boundary layer next to the invert and an ideal-fluid flow region above. In the boundary layer, the velocity distribution follows closely a power law:

$$\frac{V}{V_{max}} = \left(\frac{y}{\delta}\right)^{1/\mathrm{n}} \quad 0 \le y/\delta \le 1 \qquad (\mathrm{I}-19)$$

Where *y* is the transverse coordinate originating at the pseudo-bottom, *δ* is the boundary layer thickness defined as the perpendicular distance from the pseudo-bottom to the point where the velocity is 0.99 V_{max} . Its growth may be estimated as (Chanson, 2004):

$$\frac{\delta}{x} = 0.06106(\sin\theta)^{0.133}\left(\frac{x}{h\cos\theta}\right)^{-0.17} \qquad (I-20)$$

x is the streamwise distance from the start of the growth of the boundary layer, h is the step height and θ is channel slope. V_{max} is the free-stream velocity may be deduced from the Bernoulli equation:

$$V_{max} = \sqrt{2g(H_{max} - y\cos\theta)} \qquad (I-21)$$

Where H_{max} is the upstream total head and *y* is the local flow depth.

The inception point in stepped spillway chutes as defined by Chanson (Chanson, 1994b) is the location where the turbulent boundary layer reaches the free surface and its characteristics are L_i and d_i. L_i is the distance from the start of the growth of the boundary layer and d_I is the depth of flow at the point of inception. For smooth spillway, Wood et *al* (1983) proposed an approach for determining the distance between the spillway crest and the inception point:

$$\frac{L_i}{k_s} = 13.6(\sin\theta)^{0.0796}(F^*)^{0.713} \qquad (I-22\ a)$$

$$\frac{d_i}{k_s} = \frac{0.233}{(\sin\theta)^{0.04}}(F^*)^{0.643} \qquad (I-22\ b)$$

Where F^* is defined as :

$F^* = q/[g(\sin\theta)\{k_s\}^3]^{0.5}$ and k_s is the surface roughness.

For stepped spillway, Chanson (1994b and 2001) developed a method to determine the position of the start of air entrainment with slopes greater or equal than 22°:

$$L_i = 9.719\ (\sin\theta)^{0.0796}(F^*)^{0.713}\ k_s \qquad (I-23\ a)$$

$$\frac{d_I}{k_s} = \frac{0.4}{(\sin\theta)^{0.04}}(F^*)^{0.64} \qquad (I-23\ b)$$

Where:

L_i = distance from the crest spillway to the inception point

d_I = flow depth at the inception point

$k_s = h\ cos\theta$

h = step height

θ = channel slope

F* = Froude number defined in terms of the roughness height:

$F^* = q/[g(\sin\theta)\{\mathrm{k_s}\}^3]^{0.5}$

q = unit discharge

g = gravitational constant

Boes and Hager (2003) also developed a relationship to determine the distance between the start of the turbulent boundary layer and the inception point:

$$L_i = \frac{5.9\, y_c^{6/5}}{(\sin\theta)^{7/5} h^{1/5}} \qquad (I-24)$$

In fully developed air-water flows, the velocity distribution may be approximated by a power law:

$$\frac{V}{V_{90}} = \left(\frac{y}{\mathrm{Y}_{90}}\right)^{1/\mathrm{n}} \qquad (\mathrm{I}-25)$$

Where V_{90} is the characteristic velocity at $y=Y_{90}$. The exponent n is obtained from experiments data. Chanson and Toombes (2001) found n = 5.1 and 6 for y_c/h values of 1.5 and 1.1, respectively. Hunt and Kadavy (2010a and 2010b) taken n=6.0 with slope 14°. Matos (Chanson and Toombes, 2001) obtained n=5. Felder and Chanson (2009 and 2011) proposed n=10 for $y/Y_{90}<1$.

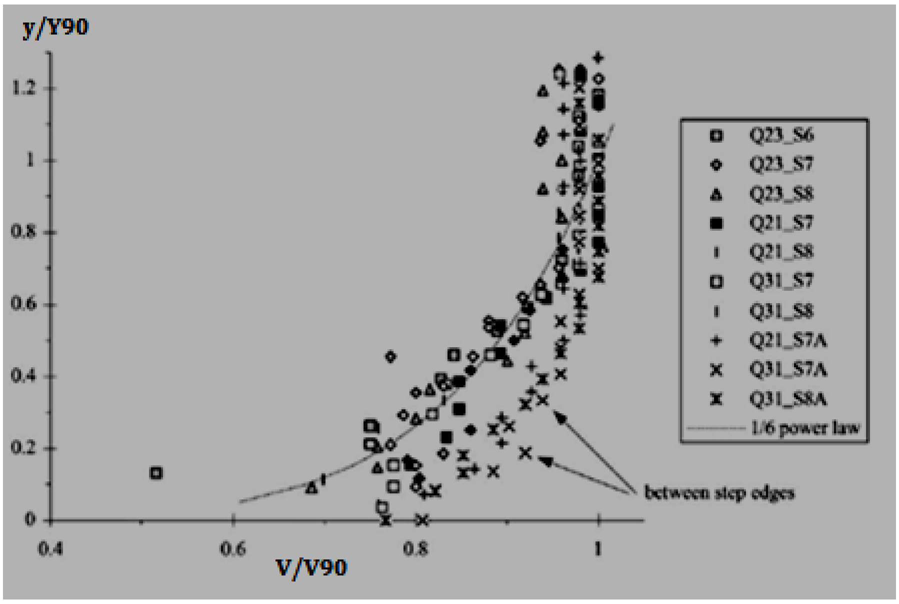

Figure I.9: Dimensionless air–water velocity distributions in skimming flow (Chanson and Toombes, 2002)

I.3 Air entrainment

Stepped chute flows are characterised by a high level of turbulence, and large amounts of air are entrained. Air bubble entrainment is caused by turbulent velocities acting at the air-water free surface. Through this interface, air is continuously trapped and released. Air entrainment occurs when the turbulent kinetic energy is large enough to overcome both surface tension and gravity effects. The turbulent velocity normal to the free surface v' must overcome the surface tension pressure and be greater than the bubble rise velocity component for the bubbles to be carried away. These conditions are:

$$v' > \sqrt{\frac{8\,\sigma}{\rho d_{ab}}} \quad \text{and} \qquad (I-26)$$

$$v' > u_r \cos\theta \qquad (I-27)$$

where σ is the surface tension, d_{ab} the air bubble diameter, and u_r the bubble rise velocity. For bubble sizes in the range 1 to 100 mm, calculations using the equations (I-26) and (I-27) suggest that air entrainment occurs for turbulent velocities v' greater than 0.1 to 0.3 m/s and air bubbles in the range 8-40 mm (Chanson 2001).

I.3.1 Air entrainment in nappe flow

A number of different mechanisms contribute to air entrainment in nappe Flow Regime (see Figure I.10). These may include:

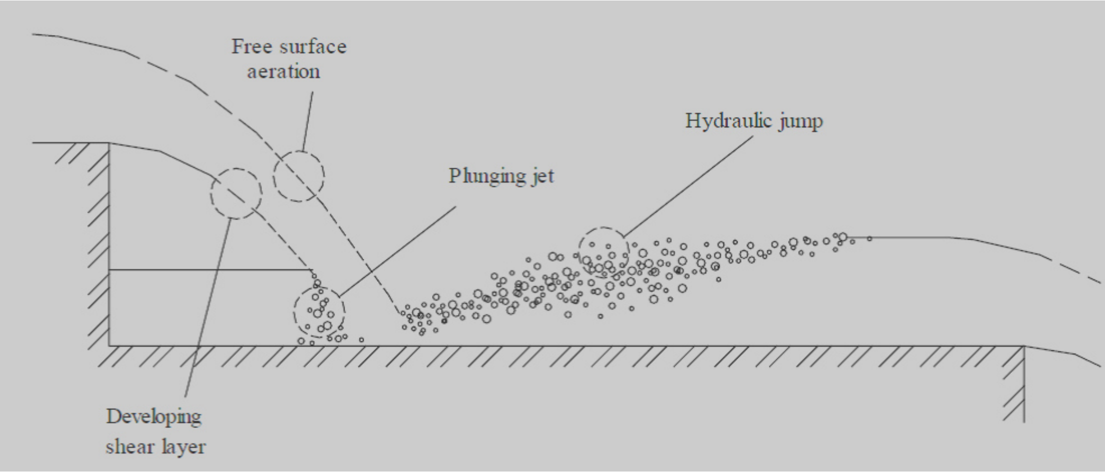

Figure I.10: Aeration mechanisms typical of Nappe Flow Regime NA1 (Toombes, 2002)

- Air entrainment by plunging jet where the free-falling nappe impacts into the recirculating pool. For deep-pooled steps, most of the air entrainment results from this mechanism;
- For Flow Regimes NA1 and NA2, large volumes of air may be entrained in the hydraulic jump that occurs downstream of the nappe impact;
- While there is no hydraulic jump for Regime NA3, high velocity flow may be characterised by significant flow fragmentation or pulverisation downstream of the nappe impact, with a large number of air-bubbles and significant spray generated;
- Turbulent water jets discharging into air are often characterised by substantial free surface aeration. The air-water shear layer at the lower interface of the free-falling nappe entrains a significant volume of air. Unless the free-falling nappe is long (large step height or high velocity), the total effect of air-entrainment at the lower nappe will be small; and
- Due to the turbulent flow on the step, air is also entrained at the free surface at the end of the step and at the upper interface of the free-falling nappe. Again, unless the free falling nappe or the regions downstream of the hydraulic jump or spray region are long, the effect of free surface aeration will be small.

I.3.2 Air entrainment in transition flow

In the transition flow regime, air bubble entrainment takes place along the jet upper nappe and in the spray region downstream of the stagnation point. The flow is highly turbulent, and air and water are continuously mixed. The distributions of air concentration may be fitted by an analytical solution of the air bubble advective diffusion equation (Chanson and Toombes, 2004):

$$\mathrm{C} = \mathrm{K}\left[1 - \exp\left(-\lambda \frac{\mathrm{y}}{\mathrm{y}_{90}}\right)\right] \qquad (\mathrm{I}-28)$$

where y is distance measured normal to the pseudo-invert, Y_{90} is the characteristic distance where $C = 90\%$, and K and λ are function of the mean air content only:

$$C_{mean} = K - \frac{0.9}{\lambda}$$

$$K = \frac{0.9}{1 - e^{-\lambda}}$$

I.3.3 Air entrainment in skimming flow

In the skimming flow regime, air entrainment occurs when the turbulent boundary layer thickness coincides with the water depth (Chanson, 1997). This location is called the inception point (e.g. **Figure I.8**). At the inception point upstream, the flow is smooth and glassy whereas at the downstream of the inception point the flow is fully developed and substantial air entrainment is observed. Turbulence acting next to the free-surface is large enough to overcome both surface tension for the entrainment of air bubbles and buoyancy to carry downwards the bubbles. The diffusion of air bubbles may be approximated by a simple diffusion model (Chanson, 1997):

$$\mathrm{C} = 1 - \mathrm{tangh}^2\left(\mathrm{K}' - \frac{\mathrm{y}}{2\,\mathrm{D}'\mathrm{Y}_{90}}\right) \qquad (\mathrm{I}-29)$$

Where

C is the void fraction (or air concentration),

tangh is the hyperbolic tangent function,

y is the distance normal to the pseudo-invert formed by the step edges,

Y_{90} is the distance where C= 90%

D' is a dimensionless turbulent diffusivity

K' is an integration constant, and

D' and K' are function of the mean air content only, where C_{mean} is the depth averaged air content defined in terms of Y_{90}.

$$\mathrm{C}_{\mathrm{mean}} = \frac{1}{\mathrm{Y}_{90}} \int_0^{\mathrm{Y}_{90}} \mathrm{C}\,\mathrm{dy} \qquad (\mathrm{I}-30)$$

$$\mathrm{D}' = \frac{0.848\mathrm{C}_{\mathrm{mean}} - 0.00302}{1 + 1.1375\mathrm{C}_{\mathrm{mean}} - 2.2925\mathrm{C}_{\mathrm{mean}}^2} \qquad (\mathrm{I}-31)$$

$$\mathrm{K}' = 0.32745015 + \frac{0.5}{\mathrm{D}'} \qquad (\mathrm{I}-32)$$

Typical values are listed in Table I.1 (Toombes, 2002). Chanson and Toombes (2001) proposed a number of advanced void fraction distribution models, based on the air-bubble diffusion model of Chanson (1995) (Equation (I-29)), but allowing for non-constant turbulent diffusivity. A good representation of experimental data for skimming flow on stepped cascades was obtained by assuming that the turbulent diffusivity:

$D' = D_0\left(1-2\left(\frac{y}{Y_{90}}-\frac{1}{3}\right)^2\right)^{-1}$, yielding:

$$C = 1-\tanh^2\left(K''-\frac{\frac{y}{Y_{90}}}{2D_0}+\frac{\left(\frac{y}{Y_{90}}-\frac{1}{3}\right)^3}{3D_0}\right) \qquad (I-33)$$

where y is distance measured normal to the pseudo-invert, Y_{90} is the characteristic distance where C = 90%, K'' is an integration constant and D_0 is a function of the of the mean air concentration C_{mean}:

$$K'' = 0.32745+\frac{1}{2D_0}-\frac{8}{81D_0} \qquad (I-34)$$

$$C_{mean} = 0.762(1.043-\exp(-3.61\,D_0)) \qquad (I-35)$$

Table I.1: Relationship between C_{mean} , D' and K'

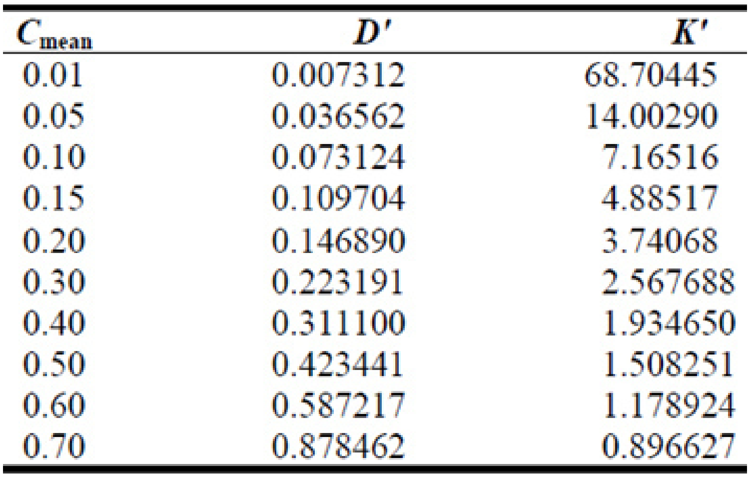

C_{mean}	D'	K'
0.01	0.007312	68.70445
0.05	0.036562	14.00290
0.10	0.073124	7.16516
0.15	0.109704	4.88517
0.20	0.146890	3.74068
0.30	0.223191	2.567688
0.40	0.311100	1.934650
0.50	0.423441	1.508251
0.60	0.587217	1.178924
0.70	0.878462	0.896627

I.4 Energy dissipation

When water is stored behind a dam or weir, the kinetic energy of the outflow must be safely dissipated to prevent erosion or other damage downstream. During the 20th Century, dam spillways have traditionally been designed as a smooth chute. Energy dissipation is achieved through the use of a separate dissipation structure at the base of the spillway, with the spillway itself contributing little towards the overall dissipation. Stepped spillways are advantageous because they have a significant energy dissipation effect, which in turn will reduce or eliminate the need for a downstream dissipation basin. Their effectiveness has at times been offset by the high cost of construction. Charles and

Kadavy (1996) found from experiments on a specific model study of a stepped spillway on a 2.5(H):1(V) slope that the energy dissipated with steps was two to three times as great as the energy dissipated with a smooth surface, the studies of Rajaratman (1990) and Christodoulou (1993) demonstrated also effectiveness the stepped chute for dissipation of kinetic energy, thereby reducing the required size of the stilling basin at the toe of the dam. Roshan et *al* (2010) showed that energy dissipation at lower flow rates were similar in both cases. However, in the skimming flow regime at higher discharges, energy dissipation was about 12% less in the 23-step model than in the 12-step model.

I.4.1 Nappe Flow

Energy dissipation on a cascade with nappe flow is achieved through a variety of mechanisms. These include jet break-up and jet mixing, impact of the nappe on the step, skin friction along the step and formation of a hydraulic jump (Regimes NA1 and NA2). Total head loss along the cascade, ΔH, is equal to the difference between the maximum upstream head, H_{max}, and the residual head at the downstream end of the channel, H_{res} .

$$\frac{\Delta H}{H_{max}} = 1 - \left(\frac{\frac{y_1}{y_c} + \frac{1}{2}\left(\frac{y_c}{y_1}\right)^2}{\frac{3}{2} + \frac{H_{dam}}{d_c}} \right) \quad \text{Un} - \text{gated spillway} \qquad (\text{I} - 36\ \text{a})$$

$$\frac{\Delta H}{H_{max}} = 1 - \left(\frac{\frac{y_1}{y_c} + \frac{1}{2}\left(\frac{y_c}{y_1}\right)^2}{\frac{H_{dam} + H_0}{y_c}} \right) \quad \text{Gated spillway} \qquad (\text{I} - 36\ \text{b})$$

where y_1 is the flow depth downstream of the falling nappe. H_{max} may be determined as $H_{max} = H_{dam} + 1.5\ y_c$ for an ungated channel or as $H_{max} = H_{dam} + H_0$ for a gated channel, where H_{dam} is the elevation of the dam crest above the dam toe and H_0 is the elevation of the free surface above the dam crest (Chanson, 2011).

By combining Equation (I-6) and Equation (I-36), the total energy dissipation for Nappe Regime with fully developed hydraulic jump becomes:

$$\frac{\Delta H}{H_{max}} = 1 - \left(\frac{0.54\left(\frac{y_c}{h}\right)^{0.275} + \frac{3.43}{2}\left(\frac{y_c}{h}\right)^{-0.55}}{\frac{3}{2} + \frac{H_{dam}}{y_c}} \right) \quad \text{Un} - \text{gated spillway} \qquad (\text{I} - 37\text{a})$$

$$\frac{\Delta \mathrm{H}}{\mathrm{H_{max}}} = 1 - \left(\frac{0.54\left(\frac{\mathrm{y_c}}{\mathrm{h}}\right)^{0.275} + \frac{3.43}{2}\left(\frac{\mathrm{y_c}}{\mathrm{h}}\right)^{-0.55}}{\frac{\mathrm{H_{dam}} + \mathrm{H_0}}{\mathrm{y_c}}} \right) \quad \text{gated spillway} \qquad (\mathrm{I}-37\ \mathrm{b})$$

Chanson (1994a) observed good agreement between Equation (I-37) and the experimental data of writers.

Equations (I-37 a) and (I-37 b) were obtained for nappe flows with fully developed hydraulic jumps. Peyras et *al.* (1992) performed experiments for nappe flows with fully and partially developed hydraulic jumps. The rate of energy dissipation of nappe flows with partially developed hydraulic jumps was within 10% of the values obtained for nappe flows with fully developed hydraulic jump for similar conditions. Therefore, it is believed that equation (I-37) may be applied to most of the nappe flow situations with a reasonable accuracy.

Tatewar and Ingle (in Dermawan and Legono, 2011) proposed the energy loss over stepped spillway for jet (nappe) flow:

$$\frac{\Delta H}{H_0} = 1 - \left[\frac{\left(\frac{y_1}{h}\right) + 0.5D\left(\frac{h}{y_1}\right)^2}{N + 1.5\left(\frac{y_1}{h}\right)} \right] \qquad (I-40)$$

$$\left(\frac{y_1}{h}\right) = 0.54D^{0.425} \qquad (I-41)$$

$$D = \frac{q^2}{gh^3} \qquad (I-42)$$

$\mathrm{H_0}$ is the energy in the flow at the crest stepped spillway.

Chamani and Rajaratnam (in Dermawan and Legono, 2011) pointed out that if the uniform-flow assumption is extended to the last step, the total head loss would be equal to the spillway height and the relative energy loss can be written as:

$$\frac{\Delta H}{H_0} = \frac{N}{N + 1.5\left(\frac{y_c}{h}\right)} \qquad (I-43)$$

where N is number of step.

I.4.2 Skimming flow

In skimming flow regime, the steps act as large roughness. Most of the energy is dissipated to maintain stable horizontal vortices beneath the pseudo-bottom formed by the external edges of the steps. The vortices are maintained through the transmission of turbulent shear stress between the skimming stream and recirculating fluid underneath. At the downstream end of the chute, the residual head equals (Chanson, 2001):

$$H_{res} = d\ \cos\alpha + \frac{q^2}{2gd^2} \qquad (I-44)$$

Where d is the clear-water depth

$$d = \int_0^{Y_{90}} (1 - C)\, dy \qquad (I-45)$$

For a very long chute in which the flow reaches uniform equilibrium at the downstream end, the total head losses ($\Delta H = H_{max} - H_{res}$) equals:

$$\frac{\Delta H}{H_{max}} = 1 - \frac{\left(\frac{f_e}{8\sin\theta}\right)^{1/3}\cos\theta + \frac{1}{2}\left(\frac{f_e}{8\sin\theta}\right)^{-2/3}}{\frac{3}{2} + \frac{H_{dam}}{y_c}} \quad \text{Un}-\text{gated spillway} \qquad (I-46)$$

$$\frac{\Delta H}{H_{max}} = 1 - \frac{\left(\frac{f_e}{8\sin\theta}\right)^{1/3}\cos\theta + \frac{1}{2}\left(\frac{f_e}{8\sin\theta}\right)^{-2/3}}{\frac{H_{dam} + H_0}{y_c}} \quad \text{gated spillway} \qquad (I-47)$$

Where H_{max} is the maximum head available, H_{dam} is the dam crest head above the downstream toe, H_0 is the reservoir free-surface elevation above the chute crest, f_e is the friction factor of air-water flows. For an un-gated channel, the maximum head available and the weir height are related by: $H_{max} = H_{dam} + 1.5\, y_c$. For a gated chute, the relationship is : $H_{max} = H_{dam} + H_0$. Equation (I-47) may be approximated for a very-high dam as:

$$\frac{\Delta H}{H_{max}} = 1 - \left[\left(\frac{f_e}{8\sin\theta}\right)^{1/3}\cos\theta + \frac{1}{2}\left(\frac{f_e}{8\sin\theta}\right)^{-2/3}\right]\frac{y_c}{H_{dam}} \qquad (I-48)$$

From equation (I-48), the rate of energy dissipation increases with the height of the dam. In practice, however, it is more appropriate to consider the dimensionless residual head (Chanson, 2001):

$$\frac{H_{res}}{y_c} = \left(\frac{f_e}{8\sin\theta}\right)^{1/3}\cos\theta + \frac{1}{2}\left(\frac{f_e}{8\sin\theta}\right)^{-2/3} \qquad (I-49)$$

Chanson (2001) has computed the rate of energy dissipation (equation I-46 and I-47) for a steep slope (θ=52°) using two values of the friction factor: f_e=0.03 and f_e=0.2, that represent an average flow resistance on smooth spillways and on stepped chutes respectively. His results are compared with experimental data, showing a larger dissipation on stepped channels for the same discharge and weir height. The agreement between data and equations (I-46 and I-47) is fair although there is a considerable scatter.

Hunt and Kadavy (2010a) reported that the energy loss follows a linear trend upstream of the inception point (see figure I.11 top). The energy loss relationship upstream of the inception point provided by Hunt and Kadavy (2010a) is:

$$\frac{\Delta H}{H_0} = 0.3\frac{L}{L_i} \qquad (I-50)$$

Downstream of the inception point, Hunt and Kadavy (2010b) was approximated the relative energy loss by the following relationship (figure I.11 bottom):

$$\frac{\Delta H}{H_0} = 1-\left(\frac{L}{L_i}+0.51\right)^{-0.87} \qquad (I-51)$$

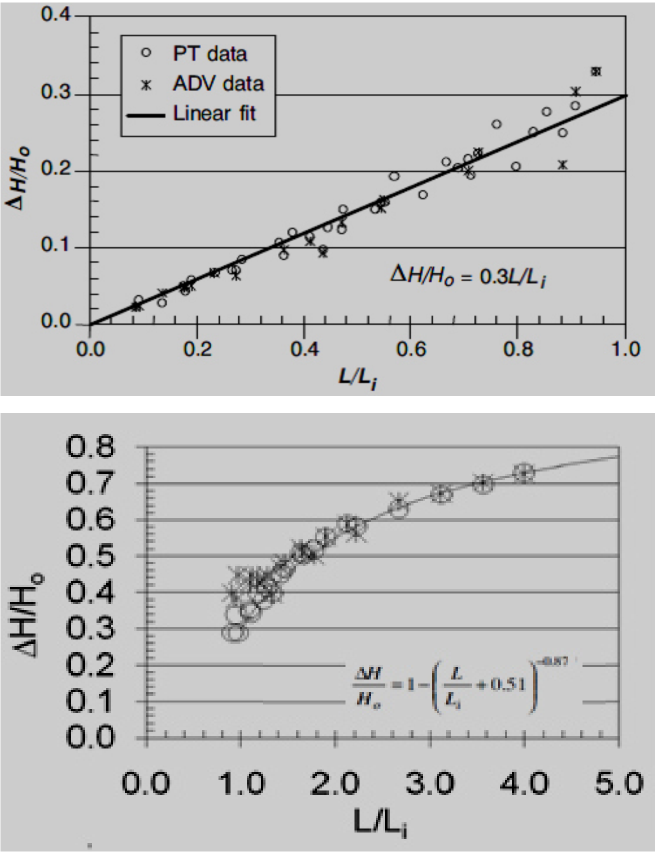

Figure I.11: Relative energy loss down the spillway chute, top : upstream of inception point, bottom : downstream of the inception point (Hunt and Kadavy, 2010a and 2010b)

I.4.3 Comparison of energy dissipation between nappe and skimming flow

Several researchers (Chanson 2010a and 2010b; Peyras et *al.*1992) suggested that higher energy dissipation is achieved in nappe flow than in skimming flow situations. For small stepped weirs, the flow might not be fully developed at the toe of the spillway in a skimming flow regime. A nappe flow regime is preferable for greater energy dissipation. However for long chutes, uniform flow conditions are obtained at the toe of the spillway and a skimming flow regime enables higher energy dissipation than a nappe flow regime.

I.5 Numerical Model

The topic of the flow over stepped spillway was the object of several experimental works, with the development of computational fluid dynamics (CFD) branch, flow over stepped spillway can be simulated to validate experimental results. Chen et *al.* (2002), simulated flow over a stepped spillway using the k –ε turbulence model. They used the unstructured grid to fit the irregular boundaries and volume of fluid method (VOF) to solve the complex free-surface problem. From figure I.12, they found that, the calculated free surface water agrees well with that of the measurement.

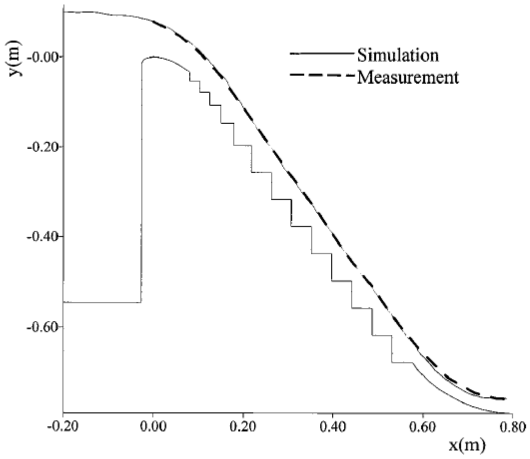

Figure I.12: Free surface water obtained by simulation and experiment (Chen et *al.* 2002)

Benmamar et *al.* (2003) developed a numerical model for the two-dimensional flow boundary layer in a stepped channel with steep slope, which was based on the implicit finite difference scheme. Bombardelli et *al.* (2010) Simulated non-aerated region of the skimming flow in steep stepped spillways using 3D-FLOW. This work discusses important aspects of the flow, such as the values of the exponents of the power-law velocity profiles, and the characteristics of the development of the boundary layer in the spillway. They observed no significant differences in the simulations with *k*–*ε* model closure and the *k*–*ε* RNG model (seen figure I.13).

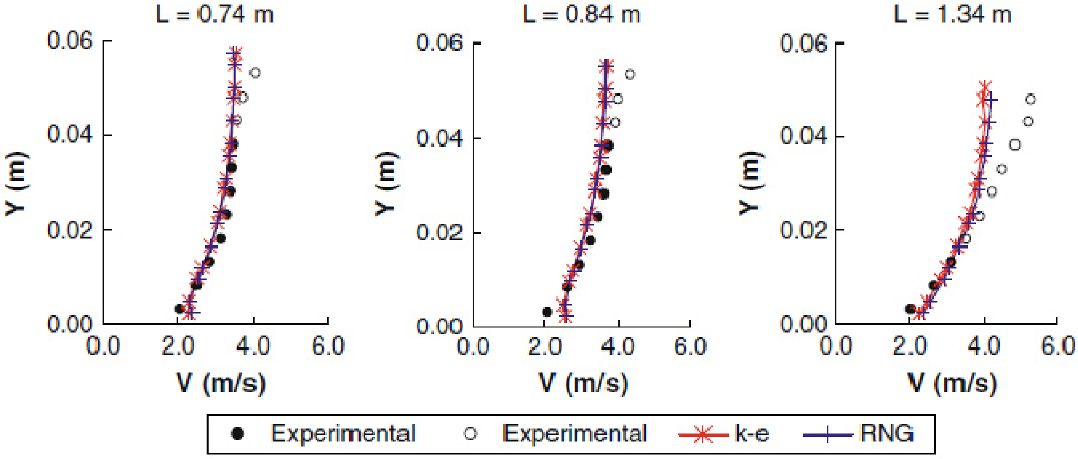

Figure I.13: Comparison among experimental and numerical results obtained using the *k*–*ε* and RNG*k*–*ε* turbulence models regarding water velocities (Bombardelli et *al.* 2010).

Carvalho and Amador (2008) also simulated the flow in the non-aerated region by using the FLOW-3d with the finite difference method (FDM). Their numerical results were compared with the physical data and found a good agreement in the non-aerated region.

Afshin and Mitra (2012) used FLUENT commercial software for examining the performance of the volume of fluid (VOF) and mixture models in simulating skimming flow over stepped spillway(e.g figure I.14).

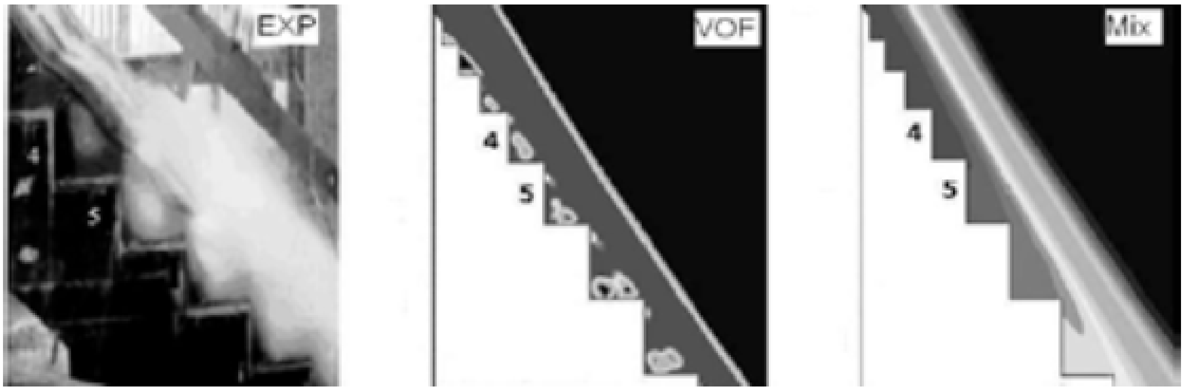

Figure I.14: Air entrainment simulated by the mixture and VOF models and experimented in a laboratory (Afshin and Mitra 2012)

Cheng et *al.* (2006) used a mixture model to reproduce the flow over a stepped spillway, including also the interaction between entrained air and cavity recirculation in the flow, velocity distribution and the pressure profiles on the step surface. The RNG (k- ε) model was chosen and their numerical results successfully reproduced the flow over the stepped spillway of the physical model (figure I.15).

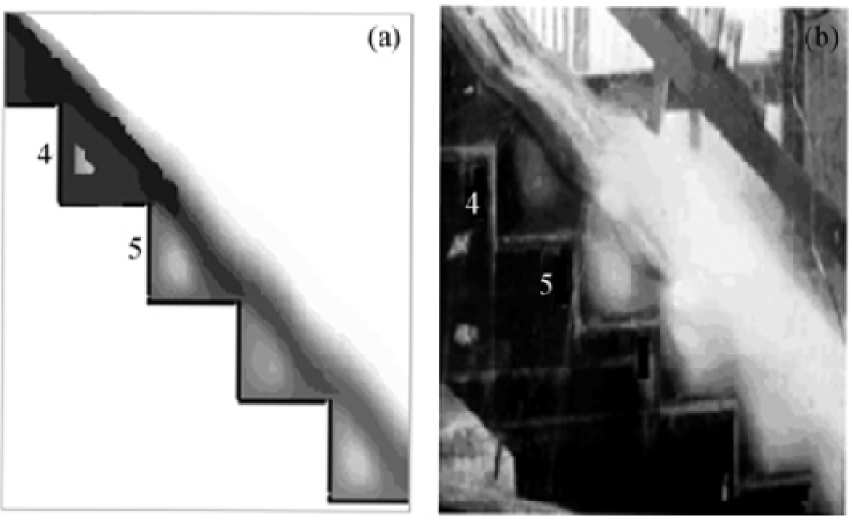

FigureI.15 : Air entrainment over the stepped spillway:
(a) Calculated; (b) measured (Cheng et *al.* 2006)

Iman and Mehdi (2010) evaluated energy dissipation in stepped spillways by taking into account parameters such as; number of steps, step height , horizontal step length , characteristic height of the step , flow discharge per unit and overall slope of stepped spillway by numerical method.

Chinnarasri et *al.* (2012) studied the flow behaviour through smooth, 25-step and 50-step spillways using a multiphase flow model with the realisable k–ε model. Their numerical results were verified by comparison with the large-scale physical model. They were found that, the maximum velocity from the smooth spillway was higher than in stepped spillway (figure I.16). Thus, the stepped spillway was more efficient than the smooth spillway in reducing the flow velocity.

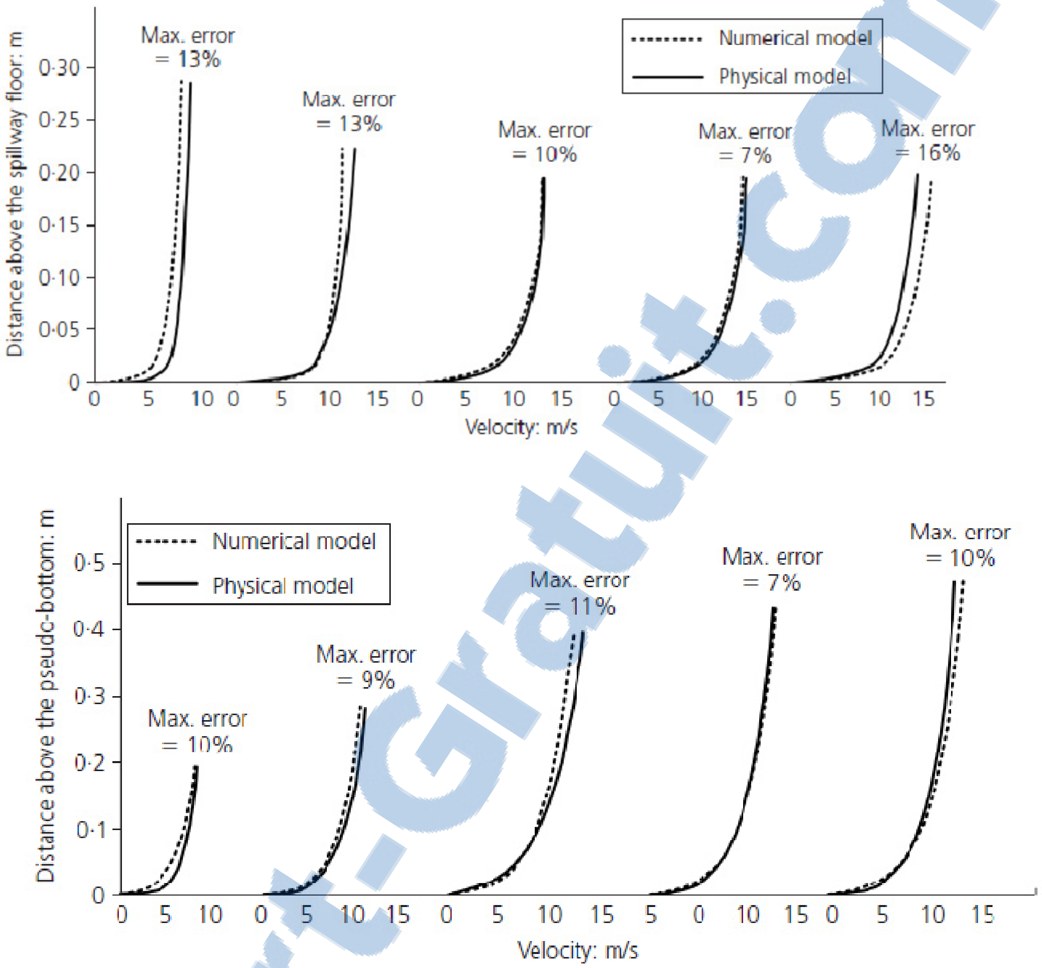

Figure I.16: Velocity profile at five locations, Top: smooth spillway, Bottom: 25 step spillway (Chinnarasri et *al.* 2012)

Numerical study of Mohammed et *al.* (2012) was performed to simulate and investigate flow characteristics over a steeply sloping stepped spillway. They used VOF model to simulate interaction between air and water and Turbulence was encountered by both RNG k-ε and Large Eddy Simulation (LES). They compared numerical results with the experimental data in two respects: location of inception of aeration (figure I.17) and air concentration distribution (figure I.18).

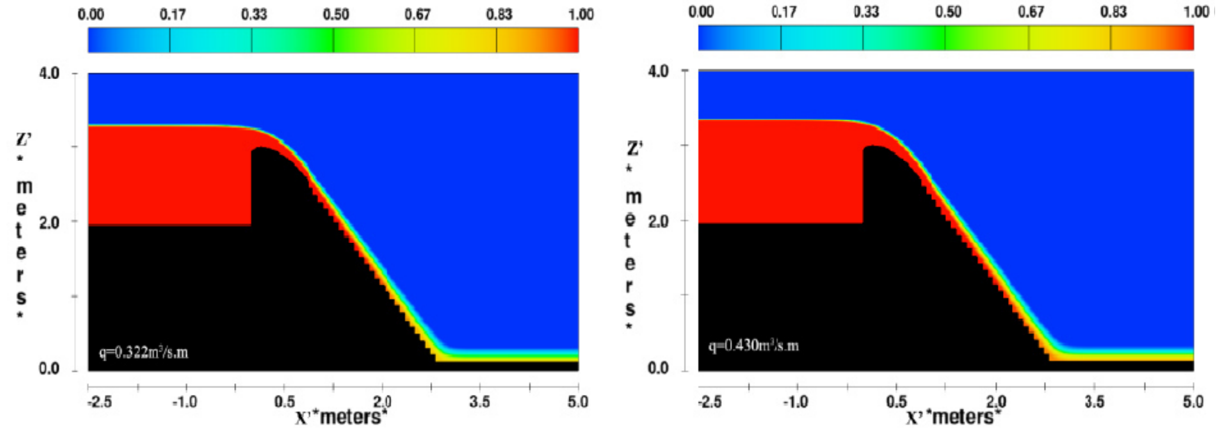

Figure I.17: Air entrainment simulated by VOF model (Mohammed et al 2012)

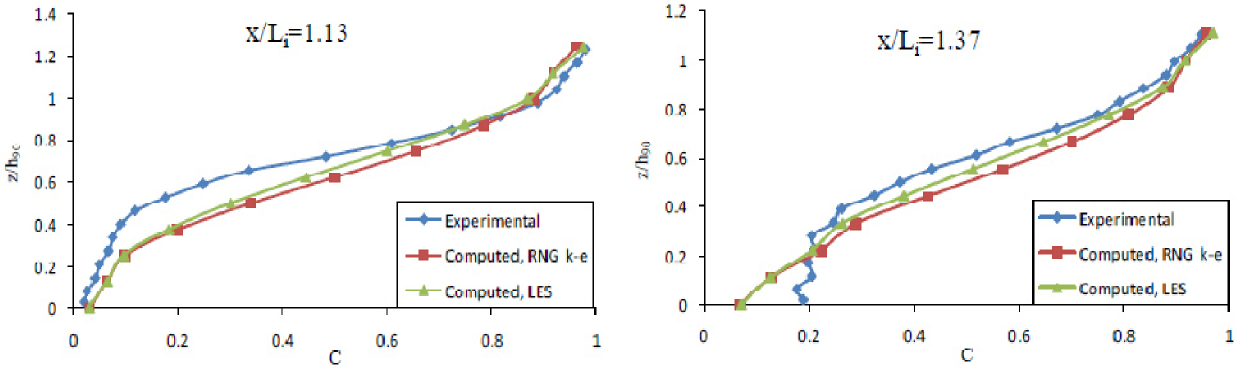

Figure I.18: Measured and numerically-derived Air concentration distribution at different positions (Mohammed et *al* 2012)

Introduction

All the free surface flows (open channel flows) are governed by the Navier-stokes equation. These include conservation of mass and momentum. These equations are in the form of partial differential equations.

The topic of the flow over stepped spillway was the object of several experimental works, with the development of computational fluid dynamics (CFD) branch, flow over stepped spillway can be simulated to validate experimental results.

In the last few decades, the computational fluid dynamics, CFD, has imposed itself as one of the best tools for the prediction of flow fields with accuracy and detail (Versteeg, and Malalasekera. 2007). The CFD methodology is based on computer codes which are being improved for increasing the range of application of such computer models. The application of such codes involves calibration and validation processes before the prediction stage.

In the present study, the numerical procedures for the stepped channel flow simulations were conducted using the FLUENT computational fluid dynamics (2006).

II.1 The Software FLUENT

Fluent Version 6.3 is a CFD computer code developed and marketed by Fluent Inc. (2006). The code solves the equations for conservation of mass, momentum and energy for single phase flow or multiphase flow using a Finite Volume technique. Different types of discretization schemes (Quadratic upwind differencing scheme (QUICK), First Order upwind scheme, Second Order upwind scheme, Power Law etc.) are available in it. A number of turbulence models such as Spalart-Allmaras model, k - ε , Re-normalisation group (RNG) k - ε , realizable k - ε , $k - \omega$ model ,shear stress transport $k - \omega$ model, etc. are offered by this numerical code (Usman,2010). This code gives a number of models for simulation of two phases flow such as VOF, Mixture and Eulerian. First the fluid domain is divided into a large number of discrete control volumes (also known as cells) using a pre-processor code which creates a computational mesh on which the equations can be solved. The meshing software available with Fluent is called Gambit. This software can create a two-dimensional (2D) surface mesh using triangular or quadrilateral elements, or a three-dimensional (3D) volume mesh using a combination of hexahedral, tetrahedral or prism elements.

Once the fluid domain has been meshed the governing equations (in integral form) for the conservation of mass, momentum, energy and any other relevant variables are applied to each discrete control volume and used to construct a set of non-linear algebraic equations for the discrete dependent variables. Fluent then solves the complete set of coupled equations for all the control volumes on the mesh using either a segregated solver or a coupled solver. In all the calculations reported here only the segregated solver has been used. In this approach the governing equations are solved sequentially. Since these equations are non-linear they first have to be linearized. This can be done either implicitly or explicitly, although when using the segregated solution method within Fluent the code automatically linearises each discrete governing equation implicitly with respect to that equation's dependent variable. This produces a scalar system of equations containing only one equation per computational cell. A point implicit (Gauss-Siedel) linear equation solver is then used in conjunction with an algebraic multigrid (AMG) method to solve the resultant scalar system of equations for the dependent variable in each cell. Since the equations are non-linear several iterations of the solution loop must be performed before a converged solution is obtained (Fluent Inc 2006).

The segregated solver thus solves for a given fluid variable (for example u – the *x* component of velocity) by considering all cells at a single time. It then solves for the next fluid variable (for example v– the *y* component of velocity) by again considering all cells at the same time. Each iteration of the solution loop thus consists of the following steps:

1. The values of the fluid variables at the cell centers are updated based on the current solution values.
2. The u_i velocity components of the momentum equation are each solved in turn using the current values for the pressure and the mass fluxes through each of the cell faces.
3. The pressure correction equation (a form of the continuity equation) is then solved to obtain the necessary corrections to the pressure and velocity fields so that the continuity equation is satisfied.
4. Where appropriate, additional scalar equations (such as those describing transport of turbulence quantities) are solved.
5. A check for convergence is made.

6. The above steps are repeated until the convergence criteria are met (all residuals less than 10^{-3})

II.2 Governing equations

The Reynolds-averaged Navier-Stokes (RANS) equations for multiphase recirculating free-surface flow over the chute and stepped spillways are written as follows:

Continuity equation:

$$\frac{\partial u_i}{\partial x_i} = 0 \qquad (II-1)$$

Momentum equation:

$$\frac{\partial u_i}{\partial t} + u_j \frac{\partial u_i}{\partial x_j} = F_i - \frac{1}{\rho}\frac{\partial p}{\partial x} + \nu \frac{\partial}{\partial x_j}\left(\frac{\partial u_i}{\partial x_j} + \frac{\partial u_j}{\partial x_i}\right) - \frac{\partial \overline{u_i' u_j'}}{\partial x_j} \qquad (II-2)$$

Where u_i and u_j are velocity components, p is the pressure, x_i and x_j coordinate components, ρ is density of fluid, ν is kinematic viscosity and $\overline{u_i' u_j'}$ is Reynolds stresses. In RANS these governing equations are averaged to give mean velocity values. In this way turbulent velocities are converted into two components, one is the average velocity and the other is its fluctuation. This fluctuation is modelled. While taking average of these equations, additional unknown terms are generated in these equations which are termed as Reynolds stresses. These stresses are solved with the help of turbulence models.

II.3 Multiphase flow model

A multiphase flow can be defined as a mixture of flow which consists of more than two phases. For the flow over stepped spillway, free surface flow with high turbulence of air is of interests. Both air and water cannot be ignored from the model because of their influence on the fluid dynamic behaviour. Then, in the numerical model, the multiphase flow model should be used in simulation. The multiphase flow model which available in FLUENT are Volume of Fluid model (VOF), Mixture multiphase flow model (MMF) and Eulerian model.

II.3.1 Volume of fluid (VOF) model

The VOF model was proposed by Hirt and Nichols (1981). The flow involves existence of a free surface between the flowing fluid and the atmospheric air above it. The flow is generally governed by the forces of gravity and inertia. In VOF model, a single set of momentum equations is solved for two or more immiscible fluids by tracking the volume fraction of each of the fluids throughout the domain. In each cell, the sum of the volume fractions of air and water is unity. So, an additional variable, the volume fraction of air or water is introduced. If α_w denotes the volume fraction of water, then the volume fraction of air α_a can be given as (Fluent Inc 2006):

$$\alpha_a = 1 - \alpha_w \qquad (II-3)$$

Continuity equation

$$\frac{\partial \alpha_w}{\partial t} + \frac{\partial}{\partial x_i}(\alpha_w u_i) = 0 \qquad (II-4)$$

The value of α_w in a cell represents the fractional volume of the cell occupied by water. In particular, a unit value of α_w will correspond to a cell full of water, while $\alpha_w = 0$ will indicate that the cell is full of air. Cells with α_w values between 0 and 1 must then contain a free surface. Thus, the coarse interface information can be known according to the value of α_w.

Momentum equation

$$\frac{\partial \rho u_i}{\partial t} + u_j \frac{\partial u_i}{\partial x_j} = \rho F_i - \frac{\partial p}{\partial x} + \frac{\partial}{\partial x_j}\left[\mu\left(\frac{\partial u_i}{\partial x_j} + \frac{\partial u_j}{\partial x_i}\right)\right] - \frac{\partial \rho \overline{u_i' u_j'}}{\partial x_j} \qquad (II-5)$$

The density of water and air (ρ_w , ρ_a) and the dynamic viscosity of water and air (μ_w , μ_a) are written as follows.

$$\rho = \alpha_w \rho_w + (1 - \alpha_w)\rho_a \qquad (II-6)$$

$$\mu = \rho_w \mu_w + (1 - \alpha_w)\mu_a \qquad (II-7)$$

II.3.2 Mixture model

The mixture model is a simplified multiphase model that can be used to model multiphase flows where the phases move at different velocities, but assume local equilibrium over short spatial length scales. The coupling between the phases should be strong. It can also be used to model homogeneous multiphase flows with very strong coupling and the phases moving at the same velocity. In addition, the mixture model can be used to calculate non-Newtonian viscosity.

The mixture model can model n phases (fluid or particulate) by solving the momentum, continuity, and energy equations for the mixture, the volume fraction equations for the secondary phases, and algebraic expressions for the relative velocities. Typical applications include sedimentation, cyclone separators, particle-laden flows with low loading, and bubbly flows where the gas volume fraction remains low.

The mixture model is a good substitute for the full Eulerian multiphase model in several cases. A full multiphase model may not be feasible when there is a wide distribution of the particulate phase or when the interphase laws are unknown or their reliability can be questioned. A simpler model like the mixture model can perform as well as a full multiphase model while solving a smaller number of variables than the full multiphase model (Fluent Inc 2006).

The mixture model allows you to select granular phases and calculates all properties of the granular phases. This is applicable for liquid-solid flows.

Continuity equation

$$\frac{\partial \alpha_m}{\partial t} + \frac{\partial}{\partial x_i}\left(\alpha_m u_{m,i}\right) = 0 \qquad (II-8)$$

where the density of mixture (ρ_m) and the velocity of mixture (u_m) are defined as

$$\rho_m = \sum_{k=1}^{n} \alpha_k \rho_k \qquad (II-9)$$

$$u_m = \frac{1}{\rho_m}\sum_{k=1}^{n} \alpha_k \rho_k \, u_k \qquad (II-10)$$

where α_k and ρ_k are the volume fraction and density of phase k , respectively. The velocity of mixture (u_m) represents the velocity of the mass centre of the mixture flow.

Momentum equation

$$\frac{\partial \rho_m u_{m,i}}{\partial t} + \frac{\partial}{\partial x_j}\left(\rho_m u_{m,i} u_{m,j}\right) =$$

$$\rho_m F_i - \frac{\partial p}{\partial x} + \frac{\partial}{\partial x_j}\left[\mu_{eff}\left(\frac{\partial u_{m,i}}{\partial x_j} + \frac{\partial u_{m,j}}{\partial x_i}\right)\right] - \frac{\partial \rho_m \overline{u'_{m,i} u'_{m,j}}}{\partial x_j} \qquad (II-11)$$

Continuity equation for phase k

From the continuity equation for secondary phase *k,* the volume fraction equation for secondary phase *k* can be obtained:

$$\frac{\partial}{\partial t}(\alpha_k \rho_k) + \frac{\partial}{\partial x_i}(\alpha_k \rho_k u_{m,i}) = -\frac{\partial}{\partial x_i}(\alpha_k \rho_k u_{M,k}) \qquad (II-12)$$

Relative velocity

Before solving the continuity equations (II-12) for phase *k* and the momentum equations (II-11) for the mixture, the diffusion velocity (u_{Mk}) has to be determined. The diffusion velocity of a phase is usually caused by the density differences, resulting in forces on the bubbles different from those on the fluid. The additional force is balanced by the drag force.

$$u_{M,k} = u_{qk} - \sum_{k=1}^{n} \frac{\alpha_k \rho_k}{\rho_m} u_{qk} \qquad (II-13)$$

where u_{qk} is the slip velocity between air and water, defined as the velocity of air relative to the velocity of water. Following Manninen *et al.* (in Fluent Inc 2006), u_{qk} is defined as:

$$u_{qk} = \frac{(\rho_m - \rho_k) d_k^2}{18 \mu_{eff.m} f_{drag}} \left[g (u_m . \nabla) u_m - \frac{\partial u_m}{\partial t} \right] \qquad (II-14)$$

where $\mu_{eff.m}$ is the effective viscosity of mixture and d_k is the diameter of the particles (or bubbles) of secondary phase k . The drag function (f_{drag}) is taken from Clift *et al.* (in Fluent Inc 2006).

$$f_{drag} = \begin{cases} 1 + 0.15\, Re^{0.637} & Re \leq 1000 \\ 0.0182\, Re & Re > 1000 \end{cases} \qquad (II-15)$$

The mixture model differs from the VOF model in two respects:

- The mixture model allows the phases to be interpenetrating.
- The mixture model allows the phases to move at different velocities, using concept of slip velocity.

II.3.3 Eulerian model

The Eulerian model is the most complex of the multiphase models. It can model multiple phases (the phases can be liquids, gases, or solids in nearly any combination) by solving a set of *n* momentum and continuity equations for each phase. Coupling is achieved through the pressure and interphase exchange coefficients. The manner in which this coupling is handled depends upon the type of phases involved; granular (fluid-solid) flows are handled differently than non-granular (fluid-fluid) flows. For granular flows, the properties are obtained from application of kinetic theory. Momentum exchange between the phases is also dependent upon the type of mixture being modelled. Applications of the Eulerian multiphase model include bubble columns, risers, particle suspension, and fluidized beds (Fluent Inc 2006).

The volume of phase k (V_k) is defined as

$$V_k = \int_V \alpha_k dV \qquad (II-16)$$

where the volume fraction of phase k (α_k)

$$\sum_{k=1}^{n} \alpha_k = 1 \qquad (II-17)$$

continuity equation

$$\frac{\partial \rho_k \alpha_k}{\partial t} + \frac{\partial}{\partial x_i}(\rho_k \alpha_k u_i) = 0 \qquad (II-18)$$

momentum equation

$$\frac{\partial \rho_k \alpha_k u_i}{\partial t} + u_j \frac{\partial \rho_k \alpha_k u_i}{\partial x_j} = \rho_k \alpha_k F_i - \frac{\partial \alpha_k p}{\partial x} + \frac{\partial}{\partial x_j}\left[\mu\left(\frac{\partial u_i}{\partial x_j} + \frac{\partial u_j}{\partial x_i}\right)\right] - \frac{\partial \rho_k \alpha_k \overline{u_i' u_j'}}{\partial x_j} \qquad (II-19)$$

II.4 Turbulence models

The most fundamental approach for the turbulence study is the direct numerical simulation (DNS). The DNS solves the 3D Navier-Stokes equations directly without using any turbulence model. The results from the DNS are the most accurate when compared with the experimental data. However, the disadvantage of the DNS is the need of the extremely high computing capacity and CPU time. The DNS hence can be used only with a simple geometry and flows with low Reynolds numbers. The large eddy simulation (LES) is similar to the DNS but the model is used for the small eddies. The accuracy of the LES is consequently lower than the DNS. The approach considered in this work is Reynolds-averaged Navier-Stokes (RANS) turbulence modeling. The RANS turbulence model is suitable for the engineering problems. It has more advantage than the DNS and the LES in the sense that it requires less computational time and computing power. The most popular RANS model is the linear k - ε turbulence model.

RANS turbulence modeling can be classified into two groups: Eddy-Viscosity Models (EVMs) and Reynolds-Stress Models (RSMs). EVMs are based on the Boussinesq (in Versteeg, and Malalasekera. 2007) hyposthesis where the Reynolds stresses are proportional to the rates of strain as follows:

$$-\rho\overline{u_i'u_j'} = \mu_t\left(\frac{\partial u_i}{\partial x_j}+\frac{\partial u_j}{\partial x_i}\right)-\frac{2}{3}\rho k\delta_{ij} \qquad (II-20)$$

Where μ_t is the eddy viscosity, k is the kinetic energy of turbulence is defined as

$$k=\frac{1}{2}\overline{u_i'u_i'}$$

δ_{ij} is the Kronecker delta (δ_{ij}=1 if i = j and δ_{ij}=0 if i≠j)

In Reynolds stress transport model, a transport equation is solved for each term in Reynolds stress tensor. One more equation for ε is also required. As a result, five additional transport equations are to be resolved in Reynolds stress transport model in 2D cases and seven transport equations are solved for three dimensional flow cases.

The turbulence models available in Fluent (2006) are:

- Spalart-Allmaras model;
- *k* –ε models (standard *k* –ε model , Renormalization-group theory based (RNG) *k* –ε model and Realizable *k* –ε model);
- *k* -ω models (standard *k* -ω model and Shear-Stress Transport (SST) *k*- *ω* Model);
- Reynolds stress model

II.4.1 Spalart-Allmaras model

The Spalart-Allmaras model is a relatively simple one-equation model as it solves only one equation for the kinematic eddy (turbulent) viscosity $\tilde{\nu}$. The Spalart-Allmaras model was designed specifically for aerospace applications involving wall-bounded flows and has been shown to give good results for boundary layers subjected to adverse pressure gradients. It is also gaining popularity for turbomachinery applications (Fluent Inc 2006).

II.4.2 Standard *k* -ε turbulence model

Launder and Spalding (1974) developed the St *k*-ε model. The assumption is that the flow is fully turbulent and the effects of molecular viscosity are negligible. Therefore, the standard *k- ε model* is valid only for fully turbulent flows.

Turbulence kinetic energy equation (k):

$$\frac{\partial}{\partial t}(\rho k)+\frac{\partial}{\partial x_i}(\rho k u_i)=\frac{\partial}{\partial x_j}\left[\left(\mu+\frac{\mu_t}{\sigma_k}\right)\frac{\partial k}{\partial x_i}\right]+G_k-\rho\varepsilon \qquad (II-21)$$

Turbulence dissipation rate energy equation (ε):

$$\frac{\partial}{\partial t}(\rho\varepsilon)+\frac{\partial}{\partial x_i}(\rho\varepsilon u_i)=\frac{\partial}{\partial x_j}\left[\left(\mu+\frac{\mu_t}{\sigma_\varepsilon}\right)\frac{\partial\varepsilon}{\partial x_i}\right]+C_{\varepsilon 1}\frac{\varepsilon}{k}G_k-C_{\varepsilon 2}\rho\frac{\varepsilon^2}{k} \qquad (II-22)$$

Where, G_k is production of turbulent kinetic energy which can be given as

$$G_k=\mu_t\left(\frac{\partial u_i}{\partial x_j}+\frac{\partial u_j}{\partial x_i}\right)\frac{\partial u_i}{\partial x_j} \qquad (II-23)$$

μ_t is the turbulent viscosity that satisfies

$$\mu_t=\rho C_\mu\frac{k^2}{\varepsilon} \qquad (II-24)$$

C_μ=0.09 is a constant determined experimentally;

σ_k and σ_ε are turbulence Prandtl numbers for k and ε equation respectively, σ_k =1.0, σ_ε=1.3, $C_{\varepsilon 1}$ and $C_{\varepsilon 2}$ are ε equation constants, $C_{1\varepsilon}$=1.44, $C_{2\varepsilon}$=1.92.

II.4.3 Re-normalisation group (RNG) *k-ε* Model

This is an improved version of standard *k-ε* model and has been developed using a statistical approach termed as Re-normalization Group Theory (RNG). This model has a broader range of application as compared to standard *k-ε* model and also yields more accurate results than standard *k-ε* model for certain flow situations. In it the impact of turbulent eddies have been incorporated which increases its accuracy in case of swirling flows. RNG *k-ε* model gives good results in case of low Reynolds number (Usman, 2010).

$$\frac{\partial}{\partial t}(\rho k)+\frac{\partial}{\partial x_i}(\rho k u_i)=\frac{\partial}{\partial x_j}\left[\frac{\mu_{eff}}{\sigma_k}\frac{\partial k}{\partial x_i}\right]+G_k-\rho\varepsilon \qquad (II-25)$$

$$\frac{\partial}{\partial t}(\rho\varepsilon)+\frac{\partial}{\partial x_i}(\rho\varepsilon u_i)=\frac{\partial}{\partial x_j}\left[\frac{\mu_{eff}}{\sigma_\varepsilon}\frac{\partial\varepsilon}{\partial x_i}\right]+C_{\varepsilon 1}\frac{\varepsilon}{k}G_k-C^*_{\varepsilon 2}\rho\frac{\varepsilon^2}{k} \qquad (II-26)$$

$$\mu_{eff}=\mu\left[1+\sqrt{\frac{C_\mu}{\mu}}+\frac{k}{\sqrt{\varepsilon}}\right]^2 \qquad (II-27)$$

Where μ_{eff} is the effective viscosity and μ is the molecular viscosity

$$C^*_{\varepsilon 2}=C_{\varepsilon 2}+\frac{C_\mu\rho\eta^3(1-\eta/\eta_0)}{1+\beta\eta^3}$$

$$\eta = S\frac{k}{\varepsilon}$$

$$S = \sqrt{2\overline{S_{ij}}\,\overline{S_{ij}}}$$

Where S is the modulus of the rate of strain tensor expressed as

$$S_{ij} = \frac{1}{2}\left(\frac{\partial u_i}{\partial x_j} + \frac{\partial u_j}{\partial x_i}\right)$$

The values of the constants in above equations are:

C_μ=0.0845, $C_{\varepsilon 1}$=1.42 , $C_{\varepsilon 2}$=1.68 , σ_k=σ_ε=0.75, η_0=4.38 , β=0.012

II.4.4 Realizable *k*-ε model

The realizable *k*-ε model proposed by Shih et al (1995) is a development of the standard *k*-ε model. The transport equations for *k* and ε are as follows:

$$\frac{\partial}{\partial t}(\rho k) + \frac{\partial}{\partial x_i}(\rho k u_i) = \frac{\partial}{\partial x_j}\left[\left(\mu + \frac{\mu_t}{\sigma_k}\right)\frac{\partial k}{\partial x_i}\right] + G_k - \rho\varepsilon \qquad (II-27)$$

$$\frac{\partial}{\partial t}(\rho\varepsilon) + \frac{\partial}{\partial x_i}(\rho\varepsilon u_i) = \frac{\partial}{\partial x_j}\left[\left(\mu + \frac{\mu_t}{\sigma_\varepsilon}\right)\frac{\partial \varepsilon}{\partial x_i}\right] + \rho C_1 S\varepsilon - \rho C_2\frac{\varepsilon^2}{k + \sqrt{\nu\varepsilon}} \qquad (II-28)$$

$$C_1 = max\left[0.43, \frac{\eta}{\eta + 5}\right]$$

$$\eta = S\frac{k}{\varepsilon}$$

$$S = \sqrt{2\overline{S_{ij}}\,\overline{S_{ij}}}$$

Where S is the modulus of the rate of strain tensor expressed as

$$S_{ij} = \frac{1}{2}\left(\frac{\partial u_i}{\partial x_j} + \frac{\partial u_j}{\partial x_i}\right)$$

C_2 = 1.9, σ_k = 1.0, σ_ε = 1.2 are the model constants, *v* = kinematic viscosity,

II.4.5 Standard *k*- *ω* Model

The standard *k*- *ω* model is based on the Wilcox *k*- *ω* model (in Versteeg, and Malalasekera. 2007), which incorporates modifications for low-Reynolds-number effects, compressibility, and shear flow spreading. The Wilcox model predicts free shear flow spreading rates that are in close agreement with measurements for far wakes, mixing layers, and plane, round, and radial jets, and is thus applicable to wall-bounded flows and free shear flows. The standard *k*- ω model is an empirical model based on model transport equations for the turbulence kinetic energy (*k*) and the specific dissipation rate (ω), which can also be thought of as the ratio of *ε* to *k* . As the *k*- ω model has been modified over the years, production terms have been added to both the k and ω equations, which have improved the accuracy of the model for predicting free shear flows. The transport equation for *k* and ω for turbulent flows at high Reynolds is given by (Versteeg, and Malalasekera. 2007) :

$$\frac{\partial}{\partial t}(\rho k)+\frac{\partial}{\partial x_i}(\rho k u_i)=\frac{\partial}{\partial x_j}\left[\left(\mu+\frac{\mu_t}{\sigma_k}\right)\frac{\partial k}{\partial x_i}\right]+G_k-\beta^*\rho k\omega \qquad (II-29)$$

$$\frac{\partial}{\partial t}(\rho\omega)+\frac{\partial}{\partial x_i}(\rho\omega u_i)$$
$$=\frac{\partial}{\partial x_j}\left[\left(\mu+\frac{\mu_t}{\sigma_\omega}\right)\frac{\partial \omega}{\partial x_i}\right]+\gamma_1\left(2\rho S_{ij}\,S_{ij}-\frac{2}{3}\rho\omega\frac{\partial \mathrm{u_i}}{\partial \mathrm{x_j}}\delta_{ij}\right)-\beta_1\rho\omega^2 \qquad (II-30)$$

The model constants are as follows:

$$\sigma_\mathrm{k}=2\,,\sigma_\omega=2,\gamma_1=0.553,\beta^*=0.09 \text{ and } \beta_1=0.075$$

II.4.6 Shear-Stress Transport (SST) k- ω Model

Menter (1993) developed the SST *k-ω* model to blend effectively the robust and accurate formulation of the *k- ω* model in the near-wall region with the free-stream independence of the *k- ω* model in the far field. The differences between the SST *k- ω* model and the standard model are: (1) the gradual change from the standard *k- ω* model in the inner region of the boundary layer, to a high-Reynolds-number version of the *k- ω* model in the outer part of the boundary layer and (2) the modified turbulent viscosity formulation to account for the transport effects of the principal turbulent shear stress. The equation for *k* is the same as in the Standard *k- ω* model, equation (II.29), while the *ω* model can be shown as

$$\frac{\partial}{\partial t}(\rho\omega)+\frac{\partial}{\partial x_i}$$
$$=\frac{\partial}{\partial x_j}\left[\left(\mu+\frac{\mu_t}{\sigma_{\omega,1}}\right)\frac{\partial \omega}{\partial x_i}\right]+\gamma_2\left(2\rho S_{ij}\,S_{ij}-\frac{2}{3}\rho\omega\frac{\partial \mathrm{u_i}}{\partial \mathrm{x_j}}\delta_{ij}\right)-\beta_2\rho\omega^2$$
$$+\frac{2\rho}{\sigma_{\omega,2}\omega}\frac{\partial k}{\partial x_j}\frac{\partial \omega}{\partial x_j} \qquad (II-31)$$

The model constants are as follows (Versteeg, and Malalasekera. 2007):

$$\boldsymbol{\sigma_k = 2\,, \sigma_{\omega,1} = 2, \sigma_{\omega,2} = 1.17, \gamma_2 = 0.44, \beta^* = 0.09 \text{ and } \beta_2 = 0.083}$$

II.4.7 Reynolds Stress Transport Model (RSM)

Out of all the RANS turbulence models, this is the most detailed turbulence model. It is based on non-isotropic behavior of the eddy viscosity. It is a seven equation model which solves seven transport equations for calculation of various terms in Reynolds stress tensor along with one equation for dissipation rate of ε. If the flow is 2D then five extra equations are resolved in this model. Although it gives very good results in complex flow situations but the time consumption and computational cost is much higher (Usman,2010). Despite its detailed treatment of turbulence, it might not always provide results better than simpler models like one and two equation turbulence models. Despite this fact, the modeler is bound to use this model for the flows with anisotropic.

II.5 Near wall treatments

Turbulent flows are significantly affected by the presence of walls. Obviously, the mean velocity field is affected through the no-slip condition that has to be satisfied at the wall. However, the turbulence is also changed by the presence of the wall in non-trivial ways. Very close to the wall, viscous damping reduces the tangential velocity fluctuations, while kinematic blocking reduces the normal fluctuations. Toward the outer part of the near-wall region, however, the turbulence is rapidly augmented by the production of turbulence kinetic energy due to the large gradients in mean velocity (Fluent Inc 2006).

Numerous experiments have shown that the near-wall region can be largely subdivided into three layers. In the innermost layer, called the "viscous sublayer", the flow is almost laminar, and the (molecular) viscosity plays a dominant role in momentum and heat or mass transfer. In the outer layer, called the fully-turbulent layer, turbulence plays a major role. Finally, there is an interim region between the viscous sublayer and the fully turbulent layer where the effects of molecular viscosity and turbulence are equally important. Figure II.1 illustrates these subdivisions of the near-wall region, plotted in semi-log coordinates.

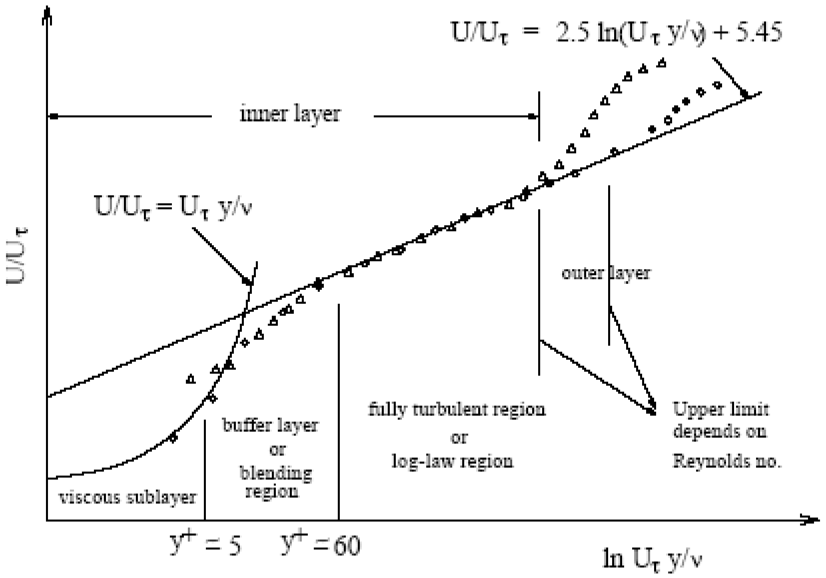

Figure II.1: Subdivisions of the Near-Wall Region

In Figure II.1, $y^+ = \rho u_\tau y/\mu$, where u_τ is the friction velocity, defined as $\sqrt{\tau_w/\rho}$

Wall functions are a collection of semi-empirical formulas and functions that in effect "bridge" or "link" the solution variables at the near-wall cells and the corresponding quantities on the wall. The wall functions comprise :

- laws-of-the-wall for mean velocity and temperature (or other scalars)
- formulas for near-wall turbulent quantities

Depending on the turbulent model you choose, **FLUENT** offers three to four choices of wall function approaches:

- Standard Wall Functions
- Non-Equilibrium Wall Functions
- Enhanced Wall Treatment

The standard wall function is based on the proposed of Launder and Spalding (1974). This function used the principle of the law of the wall for the mean velocity in the range of y^+ between 30 and 300. In the case of y^+ less than 30, the relation between the mean velocity and the position is considered as linear.

The law-of-the-wall for mean velocity yields

$$u^* = \frac{1}{\kappa} ln(Ey^*)$$

$$y^* = \frac{\rho C_\mu^{1/4} k^{1/2} y}{\mu}$$

$$y^{+} = \frac{\rho u_{\tau} y}{\mu}$$

where κ is von Karman constant and equals 0.4187, E is empirical constant and equals 9.793, k is the turbulent kinetic energy, y is distance from point to the wall, μ is dynamic viscosity and u_{τ} is friction velocity.

The non-equilibrium wall function is based on the law of the wall of Launder and Spalding (1974) for mean velocity. Kim and Choudhury (1995) modified the wall function into non-equilibrium by adding pressure-gradient effects. Moreover, the two layer- based concept was adopted to compute the budget of turbulent kinetic energy in the wall neighbouring cells.

Enhanced wall treatment is a near-wall modeling method that combines a two layer model with enhanced wall function. The two-layer model considers the mean velocity into laminar and turbulent. In the case of laminar, functions are solved as linear relation. For the case of turbulent, functions are solving by using logarithmic. Then combine both results and add blending function. These modifications become enhanced wall function (Fluent Inc 2006).

II.6 Finite volume method (FVM)

The Finite Volume Method, FVM, is a method for representing and evaluating partial differential equations as algebraic equations. It is one of the most versatile discretisation techniques used in CFD. The advantage of the finite volume method is that it is easily formulated to allow for unstructured meshes. Finite volume refers to the small volume surrounding each node point on a mesh. In this method, volume integrals in a partial differential equation that contain a divergence term are converted to surface integrals, using the divergence theorem. These terms are then evaluated as fluxes at the surfaces of each finite volume. Based on the control volume formulation of analytical fluid dynamics, the first step in the FVM is to divide the domain into a number of control volumes where the variable of interest is located at the centroid of the control volume as shown in figure II.2. The next step is to integrate the differential form of the governing equations over each control volume. Interpolation profiles are then assumed in order to describe the variation of the concerned variable between cell centroids (Duangrudee, 2012).

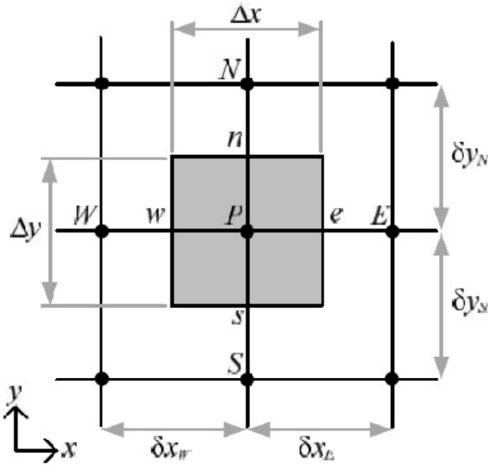

Figure II.2 Control volume (Duangrudee, 2012)

In general two techniques are used when assigning pressure and velocity values to nodes. In a collocated grid arrangement, pressure and velocity are assigned in the same nodes, in a staggered grid (e.g figure II.3) the velocities are defined on the faces of the pressure cells and vice versa. Staggered grids have an advantage over collocated arrangements originating from numerical issues in the discretization.

If one were to do a simple linear interpolation of pressure gradient in a cell with a collocated grid, the resulting expression is independent of the pressure in the actual cell itself. This can lead to oscillations of the pressure field in the solution, a so-called checkerboard pressure. Checkerboard pressures do not arise on staggered grids (Versteeg and Malalasekera. 2007).

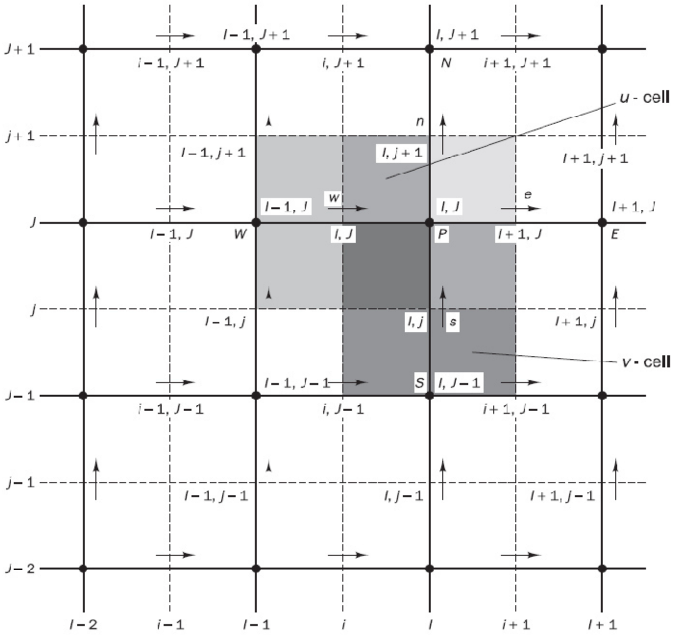

Figure II.3: Staggered grid for velocity components (Versteeg and Malalasekera. 2007)

The equations governing fluid flow can be written into a single general form which we shall call the general scalar transport equation:

$$\frac{\partial \rho\phi}{\partial t} + div(\rho\phi u) = div(\Gamma grad\phi) + S_{\phi} \qquad (II-30)$$

Where ρ is the density, **u** the velocity field and Γ the diffusivity.

II.6.1 The steady state diffusion of a property ϕ

To illustrate the basic concepts of the finite volume method, let’s consider the steady state diffusion of a property ϕ in a one-dimensional domain defined in Figure (II.4). The process is governed by:

$$\frac{d}{dx}\left(\Gamma\frac{d\phi}{dx}\right) + S_{\phi} = 0 \qquad (II-31)$$

where Γ is the diffusion coefficient and S_{ϕ} is the source term. Boundary values of ϕ at points A and B are prescribed.

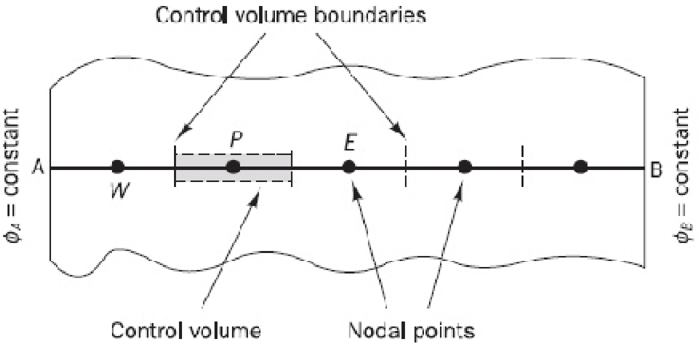

Figure II.4: Steady state diffusion of a property ϕ in a one-dimensional domain

The key step of the finite volume method is the integration of the governing equation (or equations) over a control volume shown in figrure(II.5) to yield a discretised equation at its nodal point *P*. For the control volume defined above this gives

$$\int_{\Delta V} \frac{d}{dx}\left(\Gamma\frac{d\phi}{dx}\right)dV + \int_{\Delta V} S_{\phi}dV = \left(\Gamma A\frac{d\phi}{dx}\right)_e - \left(\Gamma A\frac{d\phi}{dx}\right)_w + \overline{S_{\phi}}\Delta V = 0 \qquad (II-32)$$

Here *A* is the cross-sectional area of the control volume face, Δ*V* is the volume and D is the average value of source *S* over the control volume.

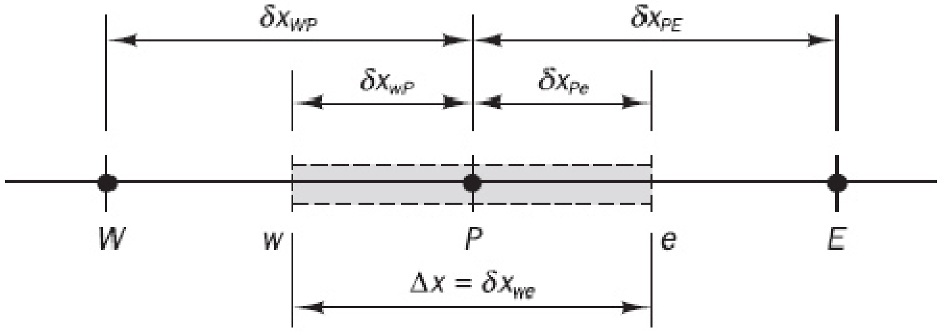

Figure II.5: Grid cells

To enable the calculation of the gradient dϕ /dx at the east and west boundaries of the cell, we need to make an assumption of the property ϕ profiles within the grid. A reasonable assumption would be that the property ϕ is varying linearly between grid points as shown in Figure (II.6).In a uniform grid linearly interpolated values for Γ_w and Γ_e are given by:

$$\Gamma_w = \frac{\Gamma_W + \Gamma_P}{2}$$

$$\Gamma_e = \frac{\Gamma_E + \Gamma_P}{2}$$

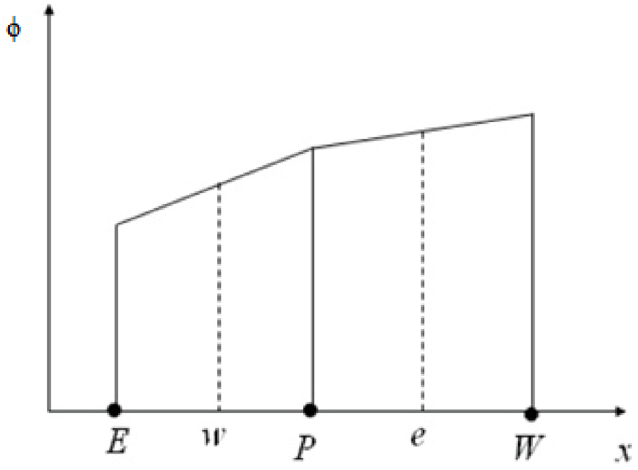

Figure II.6: Piecewise linear profile

And the diffusive flux terms are evaluated as

$$\left(\Gamma A \frac{d\phi}{dx}\right)_e = \Gamma_e A_e \left(\frac{\phi_E - \phi_P}{\delta x_{PE}}\right) \qquad (II-33)$$

$$\left(\Gamma A \frac{d\phi}{dx}\right)_w = \Gamma_w A_w \left(\frac{\phi_P - \phi_W}{\delta x_{WP}}\right) \qquad (II-34)$$

The source term S may be a function of ϕ and in this case it should be linearised as (Patankar, 1980):

$$\overline{S_\phi}\Delta V = S_u + S_P\phi_P \qquad (II-35)$$

Grouping all terms, we arrive at the following discretized equation for one-dimensional steady-state diffusion :

$$\Gamma_e A_e\left(\frac{\phi_E-\phi_P}{\delta x_{PE}}\right) - \Gamma_w A_w\left(\frac{\phi_P-\phi_W}{\delta x_{WP}}\right) + S_u + S_P\phi_P = 0 \qquad (II-36)$$

which can be rearranged into :

$$\left(\frac{\Gamma_e A_e}{\delta x_{PE}} + \frac{\Gamma_w A_w}{\delta x_{WP}} - S_P\right)\phi_P = \left(\frac{\Gamma_w A_w}{\delta x_{WP}}\right)\phi_W + \left(\frac{\Gamma_e A_e}{\delta x_{PE}}\right)\phi_E + S_u \qquad (II-37)$$

Equation (II-36) is often written in the canonical form

$$a_p\phi_p = a_W\phi_W + a_E\phi_E + S_u \qquad (II-38)$$

with coefficients

$$a_W = \frac{\Gamma_w A_w}{\delta x_{WP}}$$

$$a_E = \frac{\Gamma_e A_e}{\delta x_{PE}}$$

$$a_p = a_W + a_E - S_P$$

II.6.2 Steady-state convection and diffusion

Now, we extend the previous analysis of Equation (II-30) by including the convection term but continue to use a one-dimensional equation for simplicity. In the absence of sources, steady convection and diffusion of a property φ in a given one-dimensional flow field *u* is governed by:

$$\frac{d}{dx}(\rho u\phi) = \frac{d}{dx}\left(\Gamma\frac{d\phi}{dx}\right) \qquad (II-39)$$

The flow must also satisfy continuity, so

$$\frac{d}{dx}(\rho u) = 0 \qquad (II-40)$$

Integration of transport equation (II-39) over the control volume of Figure (II.3) gives

$$(\rho uA\phi)_e - (\rho uA\phi)_w = \left(\Gamma A\frac{d\phi}{dx}\right)_e - \left(\Gamma A\frac{d\phi}{dx}\right)_w \qquad (II-41)$$

And integration of continuity equation (II-40) yields:

$$(\rho u A)_e - (\rho u A)_w = 0 \qquad (II-42)$$

It is convenient to define two variables *F* and *D* to represent the convective mass flux per unit area and diffusion conductance at cell faces:

$$F = \rho u \quad and \quad D = \frac{\Gamma}{\delta x} \qquad (II-43)$$

The cell face values of the variables *F* and *D* can be written as

$$F_w = (\rho u)_w \quad and \quad F_e = (\rho u)_e$$

$$D_w = \frac{\Gamma_w}{\delta x_{WP}} \quad and \quad D_e = \frac{\Gamma_e}{\delta x_{PE}}$$

We develop our techniques assuming that $A_w = A_e = A$, so we can divide the left and right hand sides of equation (II-41) by area *A*. As before, we employ the central differencing approach to represent the contribution of the diffusion terms on the right hand side. The integrated convection–diffusion equation (II-41) can now be written as

$$F_e\phi_e - F_w\phi_w = D_e(\phi_E - \phi_P) - D_w(\phi_P - \phi_W) \qquad (II-44)$$

In order to solve equation (II-44) we need to calculate the transported property ϕ at the *e* and *w* faces. We have seen in the previous section how to represent the right hand side diffusion term from piecewise linear interpolation profile for ϕ. For the convection term the same choice of profile would at first seem natural. The result is

$\phi_e = \frac{1}{2}(\phi_E + \phi_P)$ et $\phi_w = \frac{1}{2}(\phi_P + \phi_W)$

Substitution of the above expressions into the convection terms of (II-44) yields

$$\frac{F_e}{2}(\phi_P + \phi_E) - \frac{F_w}{2}(\phi_W + \phi_P) = D_e(\phi_E - \phi_P) - D_w(\phi_P - \phi_W) \qquad (II-45)$$

This can be rearranged to give

$$\left[\left(D_w + \frac{F_w}{2}\right) + \left(D_e - \frac{F_e}{2}\right) + (F_e - F_w)\right]\phi_P = \left(D_w + \frac{F_w}{2}\right)\phi_W + \left(D_e - \frac{F_e}{2}\right)\phi_E \quad (II-46)$$

Identifying the coefficients of ϕ_W and ϕ_E as a_W and a_E, the central differencing expressions for the discretised convection–diffusion equation are:

$$a_P\phi_P = a_W\phi_W + a_E\phi_E \qquad (II-47)$$

Where :

$a_W = \left(D_w + \frac{F_w}{2}\right)$

$$a_E = \left(D_e - \frac{F_e}{2}\right)$$

$$a_P = a_W + a_E + (F_e - F_w)$$

The disadvantage of central differencing scheme is unstable when convective fluxes are supercritical, i.e., when $P_e = F / D \geq 2$. There is a possibility of a_E or a_W becoming negative. The Peclet number "P_e" is the ration of the strengths of convection and diffusion. In pure diffusion the Peclet number is equal to zero and ϕ will spread equally in all directions, whereas for a Peclet number of infinity ϕ will be transported exclusively in the direction of convection, away from its source. It is important for any interpolation scheme for convection (table II.1) to be able to reproduce, as faithfully as possible, the ratio of these two strengths.

Table II.1: The neighbour coefficients for different schemes

Scheme	a_W	a_E
Central differencing	$\left(D_w + \frac{F_w}{2}\right)$	$\left(D_e - \frac{F_e}{2}\right)$
Upwind differencing	$D_w + max(F_w\,, 0)$	$D_e + max(0, -F_e)$
Hybrid differencing	$max(F_w\,, (D_w + F_w/2), 0)$	$max(-F_e, (D_e - F_e/2), 0)$
Power law	$D_w\, max[0, (1 - 0{,}1\lvert P_{ew}\rvert^5)]$ $+ max\ (F_w, 0)$	$D_e\, max[0, (1 - 0{,}1\lvert P_{ee}\rvert^5)]$ $+ max\ (-F_e, 0)$

The accuracy of hybrid and upwind schemes is only first-order in terms of Taylor series truncation error (TSTE). The use of upwind quantities ensures that the schemes are very stable, but the first-order accuracy makes them prone to numerical diffusion errors. Such errors can be minimised by employing higher-order discretisation. The quadratic upstream interpolation for convective kinetics (QUICK) scheme of Leonard (in Versteeg and Malalasekera. 2007) uses a three-point upstream-weighted quadratic interpolation for cell face values. The face value of φ is obtained from a quadratic function passing through two bracketing nodes (on each side of the face) and a node on the upstream side. The discretised equations of the standard QUICK method have the following form for a general internal node point:

$$a_P\phi_P = a_W\phi_W + a_E\phi_E + a_{WW}\phi_{WW} + a_{EE}\phi_{EE} \qquad (II-48)$$

Where

$$a_p = a_W + a_E + a_p = a_{WW} + a_{EE} + (F_e - F_w) \qquad (II-49)$$

The neighbour coefficients of the standard QUICK scheme are:

$$a_{W=}D_w + \frac{6}{8}\alpha_w F_w + \frac{1}{8}\alpha_e F_e + \frac{3}{8}(1-\alpha_w)F_w \qquad (II-50)$$

$$a_{WW} = -\frac{1}{8}\alpha_w F_w \qquad (II-51)$$

$$a_E = D_e - \frac{3}{8}\alpha_e F_e - \frac{6}{8}(1-\alpha_e)F_e - \frac{1}{8}\,(1-\alpha_w)F_w \qquad (II-52)$$

$$a_{EE} = \frac{1}{8}(1-\alpha_e)F_e \qquad (II-53)$$

With

$$\alpha_w = 1\; for F_w\; > 0\; and\;\; \alpha_e = 1\; for\; F_e > 0$$

$$\alpha_w = 0\; for F_w\; < 0\; and\;\; \alpha_e = 0\; for\; F_e < 0$$

II.6.3 Algorithms for pressure-velocity coupling

The SIMPLE algorithm stands for Semi-Implicit Method for Pressure-Linked Equations. This is the most popular one of all the algorithms. This has been developed by Patanker and Spalding, (Patankar and Spalding 1972). They presented it for solving momentum equations in discretized form using iterative approach. For calculation of velocity fields through momentum equations, the pressure values must be known. In it, the condition of continuity is satisfied through pressure field. This pressure field is indirectly specified into the continuity equation. For this a complete set of discretized equations for momentum and continuity is first obtained and then solved for discretized equations (figure II.7). There is another algorithm termed as SIMPLER (Simple-Revised). This is a modified version of SIMPLE algorithm. In this algorithm the discretised continuity equation is used to derive a discretised equation for pressure, instead of a pressure correction equation as in SIMPLE. Thus the intermediate pressure field is obtained directly without the use of a correction (figure II.8). The PISO (Pressure Implicit with Splitting of Operators) is a pressure-velocity calculation procedure designed for non-iterative computation of the unsteady flow. The PISO algorithm provides improved performance over SIMPLE and SIMPLEC algorithms. The steady state PISO algorithm has an extra correction step in addition to SIMPLE algorithm which shows a robust convergence and requires less computational effort (Versteeg and Malalasekera. 2007). The PISO algorithm solves the pressure correction equation twice requiring additional storage for calculating the source term of the second pressure correction equation. Although this method involves additional computational effort, it has been found to be efficient and fast (figure II.9).

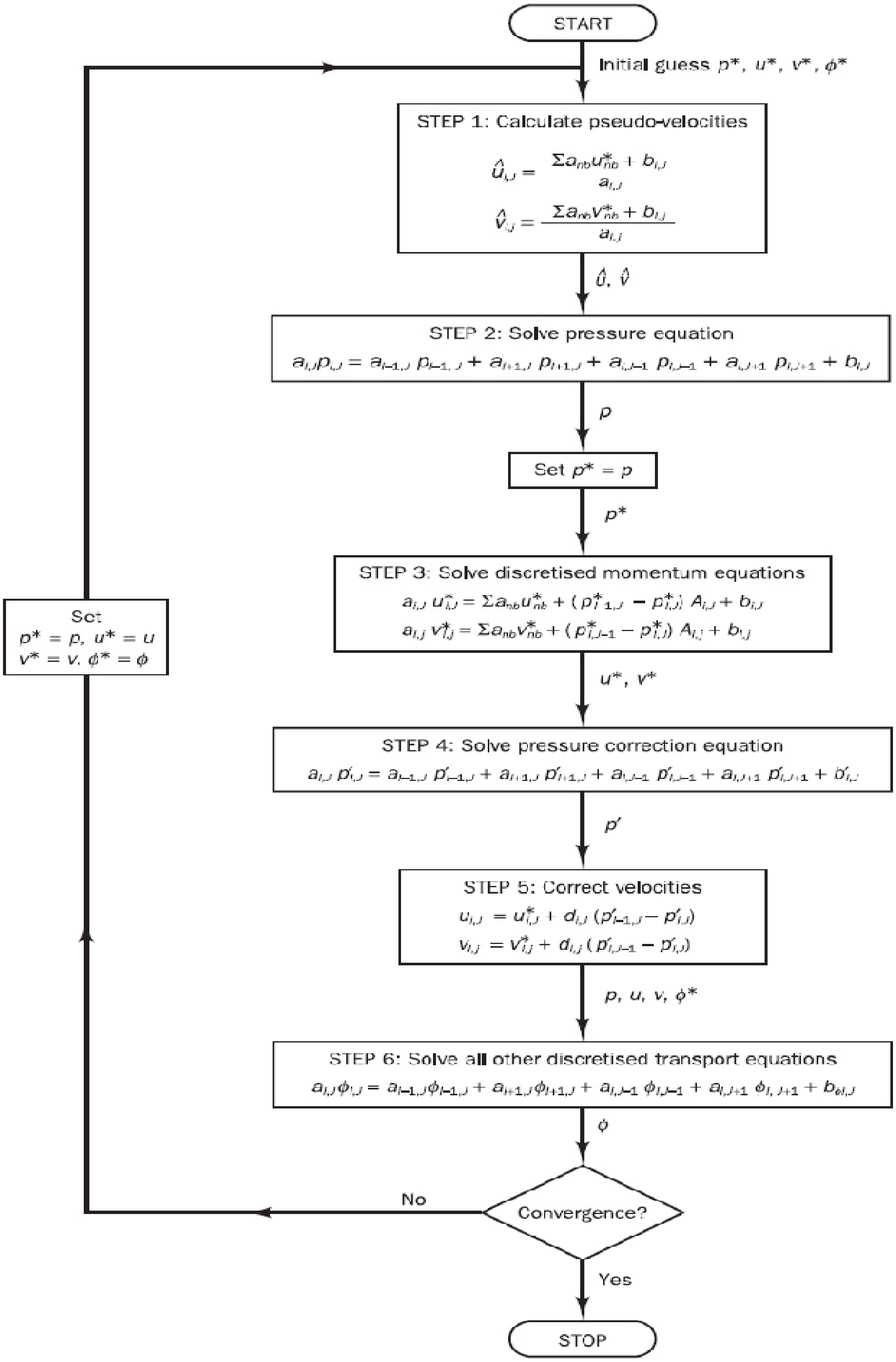

Figure II.7: The SIMPLE algorithm

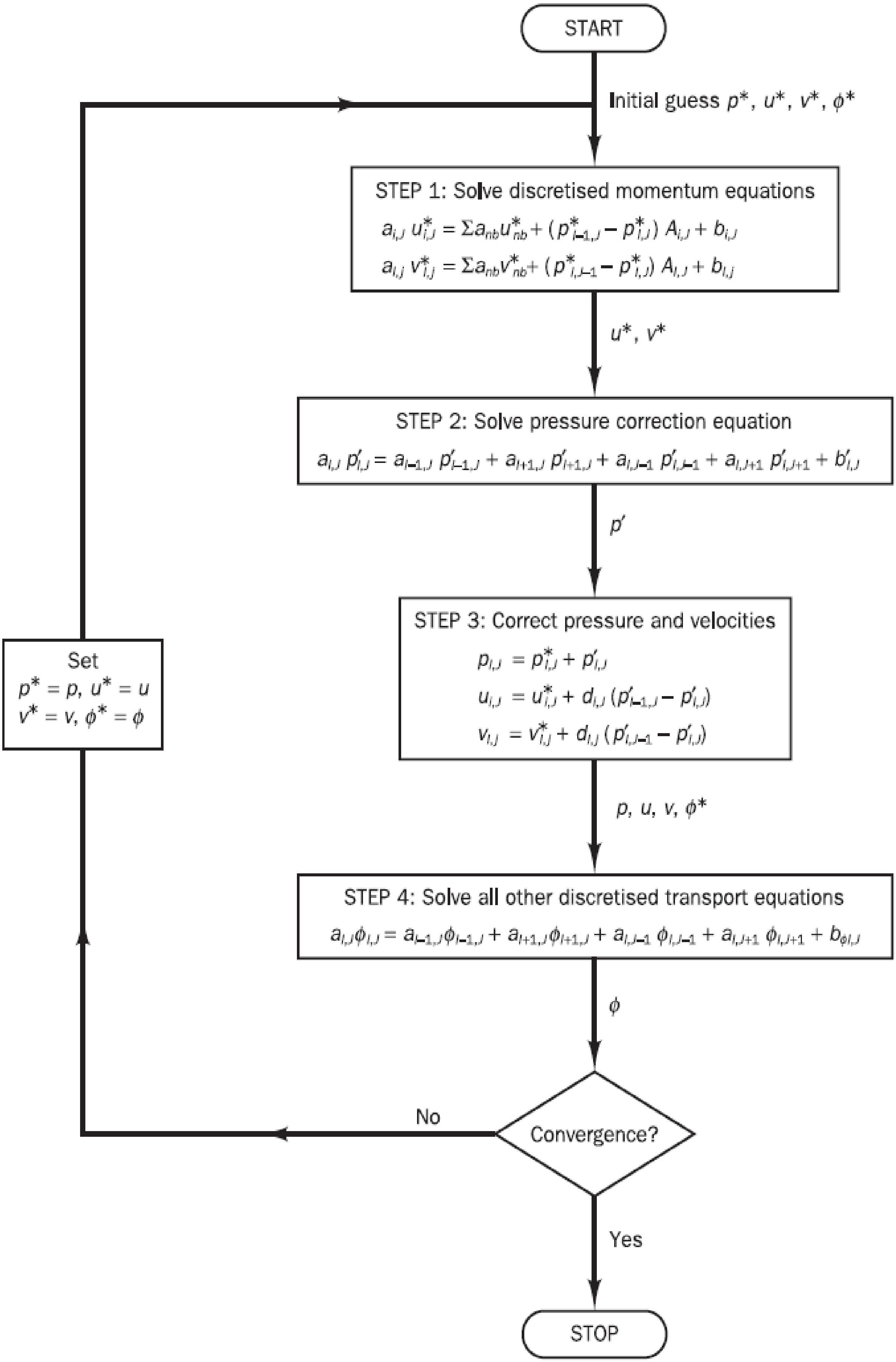

Figure II.8: The SIMPLER algorithm

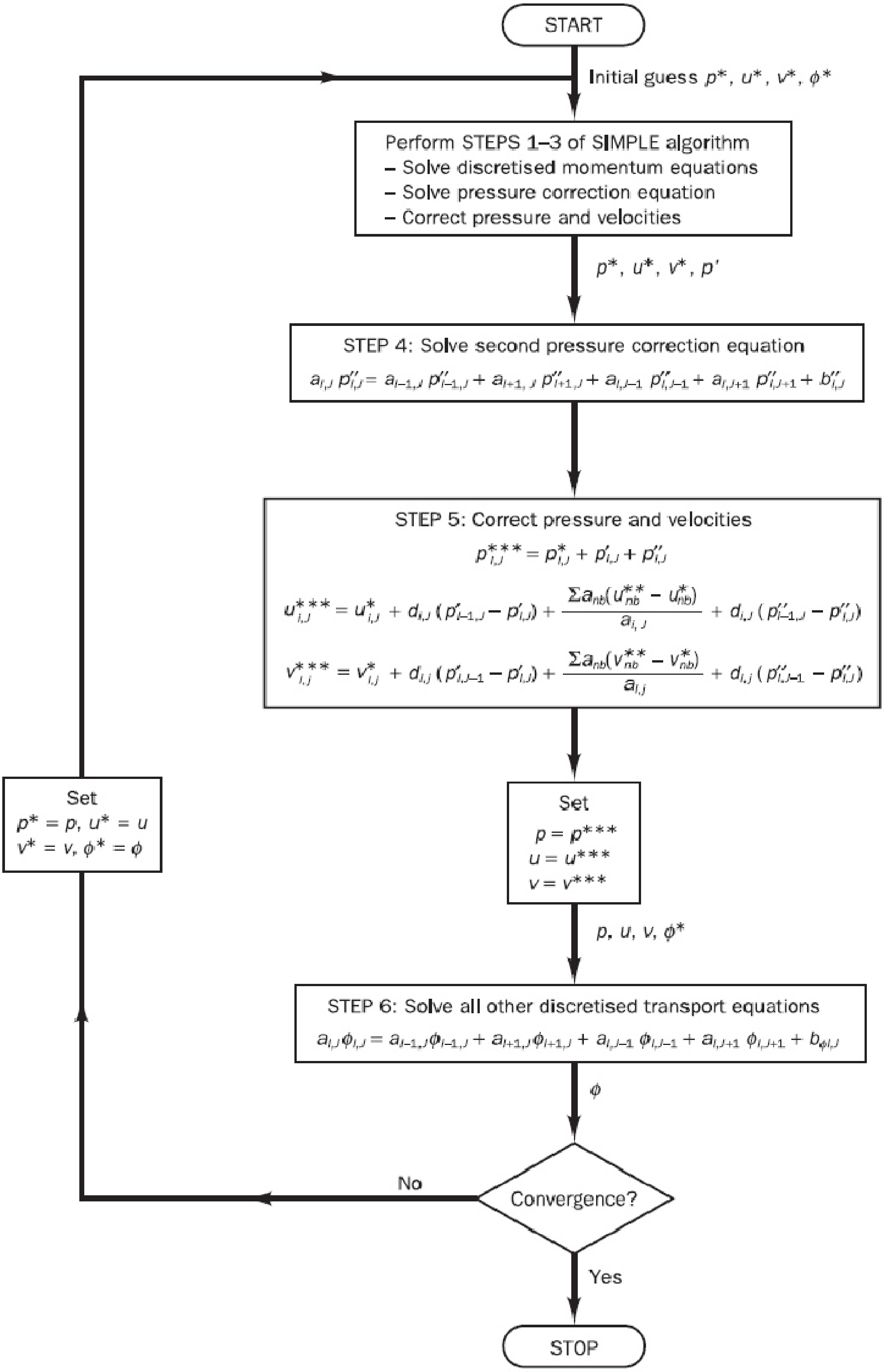

Figure II.9: The PISO algorithm

Introduction

This chapter presents the results of numerical simulation flow in stepped spillway with uniform step height obtained by using Fluent computational fluid dynamics (2006). The experimental data by Hunt and Kadavy (2009 and 2010a) and Chanson, H. and Toombes, L. (2001) were used for validation of flow simulation over the stepped spillway. The comparison includes the location of air entrainment, velocity profile, pressure and characteristic of turbulence.

III.1 Stepped spillway model (Description of physical model)

In order to validate the numerical results of the air-water two-phase flow over the stepped spillway, two physical models provided by Hunt and Kadavy (2009) and Chanson, H. and Toombes, L. (2001) are simulated by Fluent (2006).

The first physical model is shown in figure (III.1). This physical model was 10.8 m long and 1.5 m vertical drop. The channel slope is 14°. The stepped spillway contains 40 steps with 38 mm height and 152mm length by step for case 1. In the second case the stepped spillway contains 20 steps with 76 mm height and 304mm length by step. For the last case the stepped spillway contains 10 steps with 152mm height and 608mm length by step.

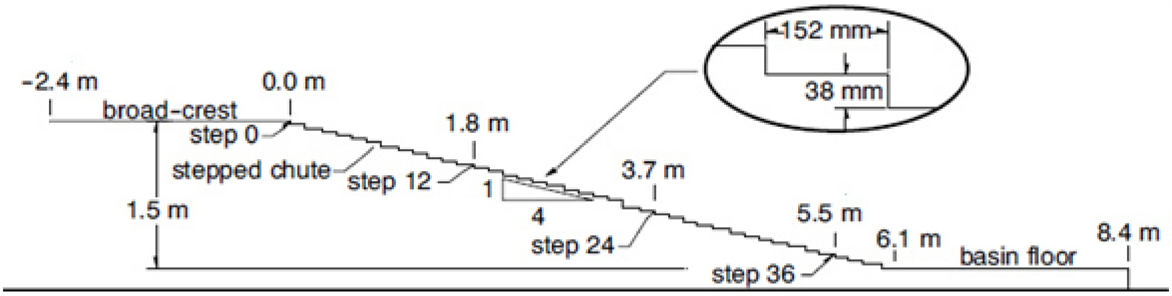

Figure III.1: Physical model provided by Hunt and Kadavy (2009)

Figure (III.2) present the second physical model. This physical model was 2.7-m long, 1-m wide, 21.8° slope chute. The broad-crested weir was1-m wide, 0.6-m long, with upstream rounded corner (0.057-m radius) followed by nine identical steps (height = 0.1 m, length = 0.25 m).

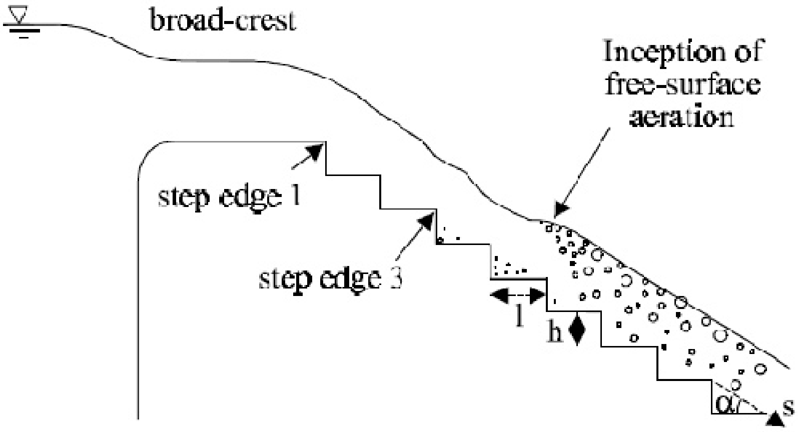

Figure III.2: Geometry of the stepped spillway used by Chanson, H. and Toombes, L. (2001)

III.2 Meshing the Geometry and boundary conditions:

The GAMBIT software was used to create and mesh the geometry. The geometry formation started first by making edges, then connecting edges to form faces. The 2D grid was used because the results from the physical model were collected only at the centerline. Also, the use of 2D grid takes much less time than 3D grid. The physical model constructed by Hunt and kadavy (2009) was discretised into structured grid (quadrilateral cell) with size of 0.01 m^2 (**figure III.3**).

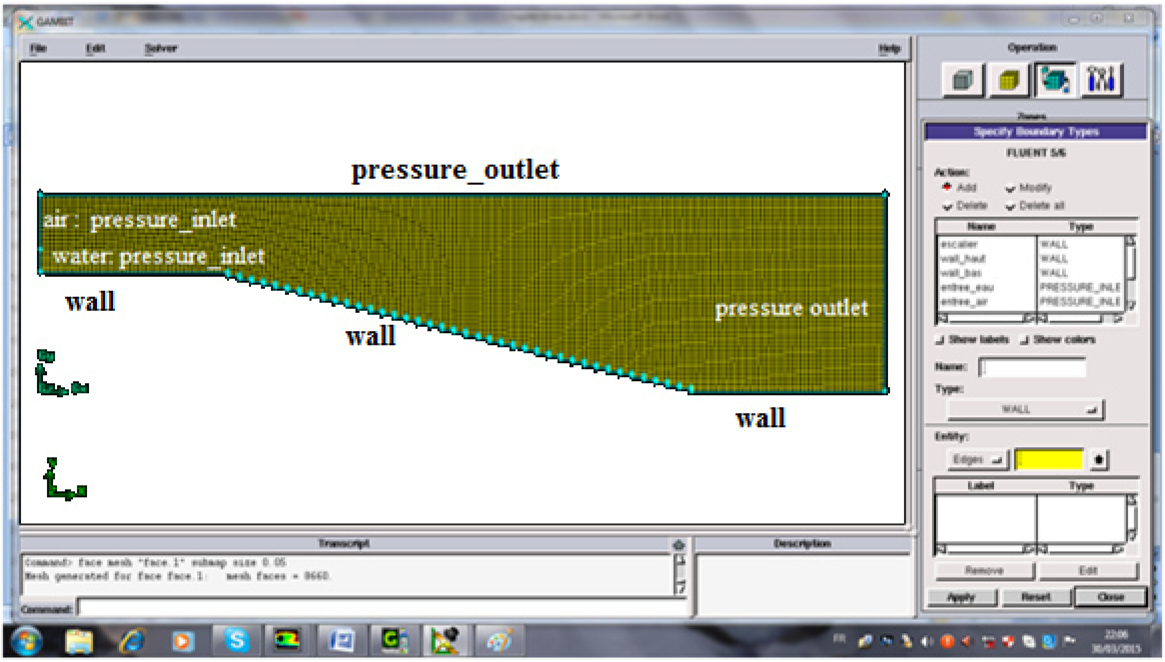

Name	Type
escalier	WALL
wall_haut	WALL
wall_bas	WALL
entree_eau	PRESSURE_INLE
entree_air	PRESSURE_INLE

```
Command> face mesh "face.1" submap size 0.05
Mesh generated for face face.1:   mesh faces = 8660.
```

Figure III.3: Mesh domain and boundary conditions by Gambit

The physical model of Chanson.H and Toombes.L (2001) was divided into unstructured grids (triangular cell) that had a high adaptability to the complex geometry and boundary. Triangular meshes with 0.015 m^2 are used (**figure III.4**).

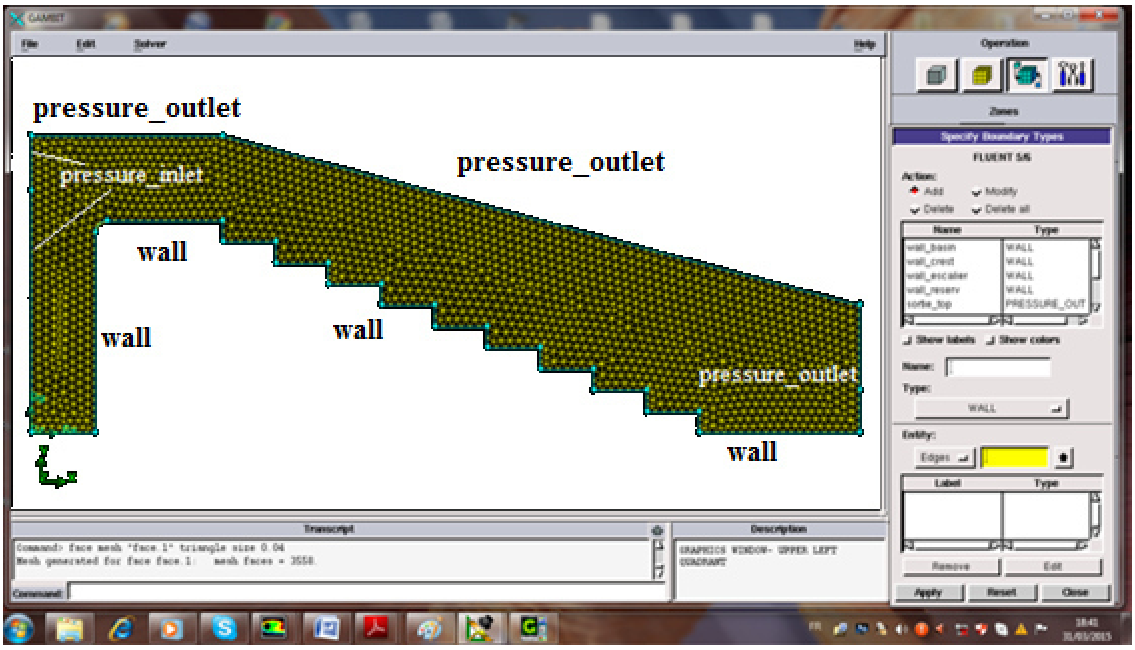

Name	Type
wall_basin	WALL
wall_crest	WALL
wall_escalier	WALL
wall_reserv	WALL
sortie_top	PRESSURE_OUT

```
Command> face mesh "face.1" triangle size 0.04
Mesh generated for face face.1:   mesh faces = 3558.
```

Figure III.4: Grid and boundary conditions by Gambit

Fluent computational fluid dynamics (CFD) is used to solve Navier-Stokes equations that are based on momentum and mass conservation of multi-phase flow over stepped spillway. Because the standard $k-\varepsilon$ model is still a good tool for numerical simulation of flow in stepped spillways and verified by experimental and field data (Chen et al, 2002), it is used to simulate turbulence. The volume fraction, momentum and turbulence closure equations were discretized by employing a conservative, second-order accurate upwind scheme. The pressure-velocity coupling algorithm is the pressure-implicit with splitting of operators (PISO). The boundary conditions in this study are pressure inlet as water inlet and air inlet, outlet as a pressure outlet type. We employed also the velocity inlet as water inlet and air inlet. All of the walls as a stationary, no-slip wall. The viscosity layer near to the wall dealt with the standard wall function. The boundary conditions for the turbulent quantities such as k and ε can be calculated from (Fluent Inc 2006):

$$k = \frac{3}{2}\left(U_{avg} I\right)^2 \qquad (III-1)$$

$$\varepsilon = C_u^{3/4} \frac{k^{3/2}}{0.07 D_H} \qquad (III-2)$$

Where, I is turbulence intensity can be estimated from the following formula derived from an empirical correlation for pipe flows:

$$I = 0.16(Re_{DH})^{-1/8} \qquad (III-3)$$

U_{avg} is the mean velocity of water flow inlet and D_H is the hydraulic diameter.

The numerical value of boundary conditions are listed in Table III.1

TableIII.1: Inflow conditions

models	**q** **(m^2/s)**	**U** **(m/s)**	**D_H= h** **(m)**	**I** **(-)**	**k $\times10^{-4}$** **(m^2/s^2)**	**$\varepsilon\times10^{-6}$** **(m^2/s^3)**
Hunt and Kadavy (2009)	0.11	0.85	0.13	0.037	13.97	907.55
	0.20	1.0	0.2	0.0347	17.92	885.23
	0.28	1.16	0.25	0.033	20.62	872.9
	0.42	1.35	0.32	0.0315	24.42	858.28
	0.62	1.5	0.42	0.03	28.72	844.46
	0.82	1.61	0.51	0.029	32.27	834.68
Chanson and Toombes (2001)	0.046	0.0427	1.075	0.0418	0.0479	0.0229
	0.052	0.0480	1.081	0.0411	0.0587	0.0308
	0.058	0.0532	1.088	0.0406	0.0702	0.0402
	0.064	0.0584	1.094	0.0401	0.0825	0.0509
	0.066	0.0602	1.096	0.0399	0.0868	0.0548
	0.071	0.0644	1.100	0.0396	0.0978	0.0652
	0.08	0.0721	1.109	0.0390	0.1187	0.0866
	0.085	0.0763	1.113	0.0387	0.1309	0.0999
	0.099	0.0879	1.125	0.0379	0.1673	0.1427
	0.103	0.0912	1.129	0.0378	0.1783	0.1564
	0.114	0.100	1.138	0.0373	0.2095	0.1978
	0.124	0.1081	1.146	0.0369	0.2394	0.2399
	0.130	0.1129	1.151	0.0367	0.2579	0.2671
	0.147	0.1262	1.163	0.0361	0.3128	0.3528
	0.164	0.1394	1.176	0.0356	0.3708	0.4507
	0.182	0.1530	1.189	0.0352	0.4355	0.5675

III.3Results and discussion

The aims of this work are to evaluate the effect step height on the position of inception point and to validate the relationships developed by researchers for determining the distance from the spillway crest to the inception point. Also to compare the velocity profile with one-sixth power law distribution and to present pressure contours and velocity vectors at the bed surface. The found numerical results are compared with the existing experimental results (Chanson and Toombes 2001; Hunt and Kadavy 2009 and 2010a).

III.3.1 Flow regime

Figure (III.5) shows the transition flow and skimming flow simulated by VOF model and obtained by experiments (Chanson and Toombes 2001). This figure shows good agreements between the numerical results and experimental results.

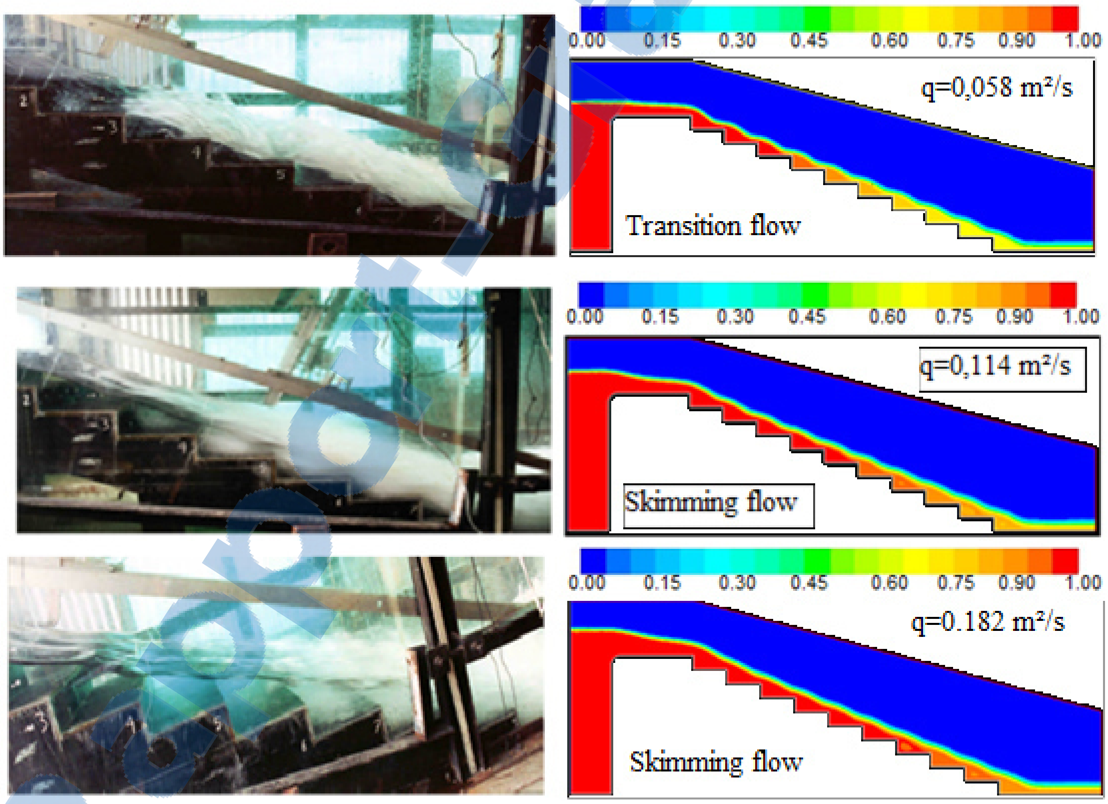

Figure III.5: Transition flow and skimming flow simulated by VOF model and obtained by experiments

From this figure, the transition flow observed for the low range of water discharge and the skimming flow occurred for upper range of water discharge. In skimming flows, the water skimmed smoothly over the pseudo bottom formed by the steps.

In transition flows, the water exhibited a chaotic behaviour associated with the intensive recirculation in cavities, strong spray and splashing. Skimming flow occurs when:

$$\frac{y_c}{h} > 1.2 - 0.325\frac{h}{l} \qquad (III-4)$$

III.3.2 Inception point of air entrainment

Figure III.6 presents a comparison the air entrainment simulated by VOF model and in experiments for unit discharge equal to 0.28m^2/s with step heights are 38 mm, 76 mm and 158 mm for flat sloped stepped spillway (Hunt and Kadavy 2009). As can be seen from this figure, the calculated inception point is well agreed with that of measurement. This figure shows that the step heights increases, the inception point was noted to move further upstream of the spillway crest.

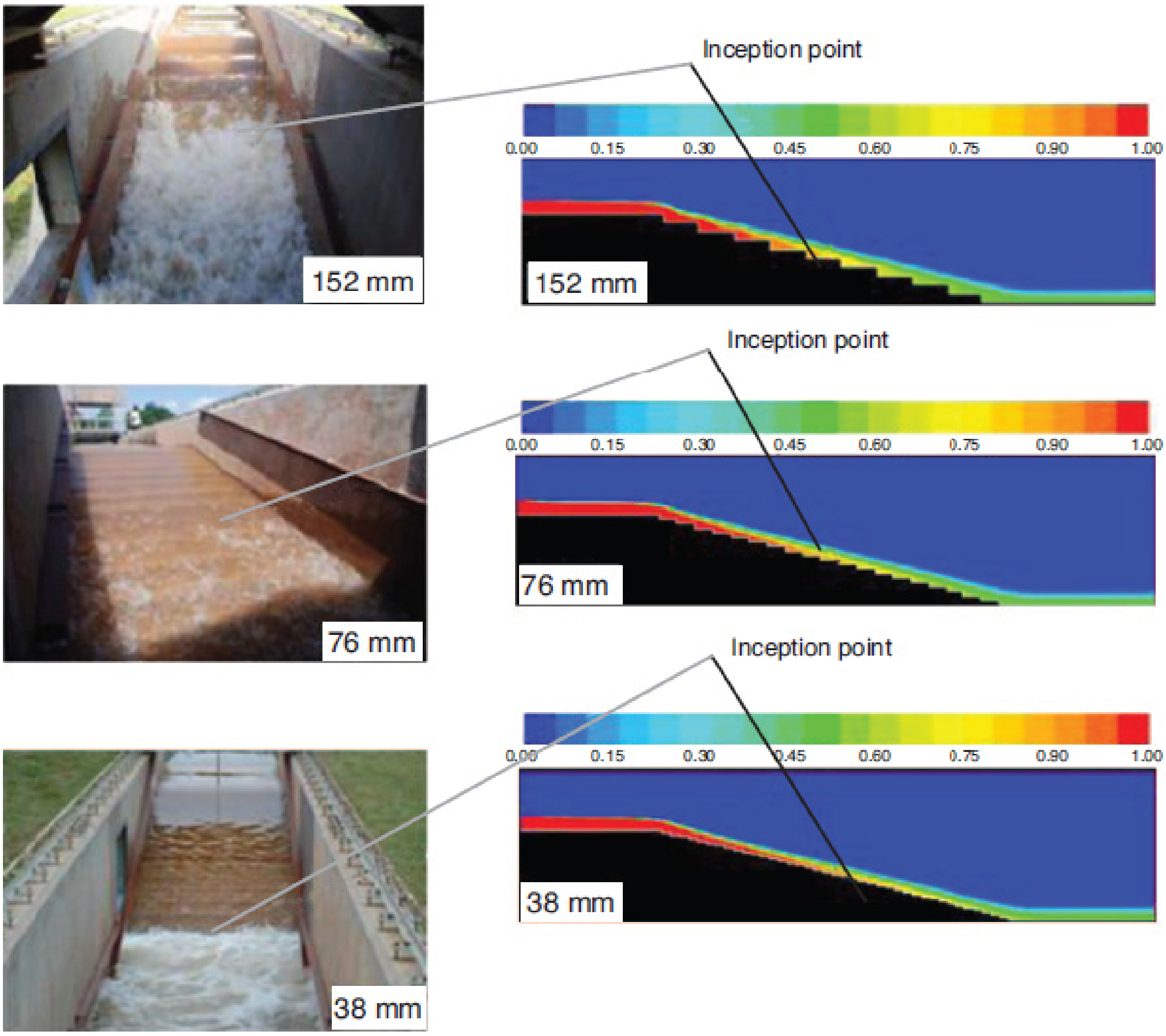

Figure III.6: Measured and computed inception point for q=0.28m^2/s

The results of numerical computation volume fraction of water over flat sloped stepped spillway for different discharges were depicted in Figure III.7. This figure indicates that the inception point moves toward the basin floor when the discharge increases. Same remark can be seen from figure (III.5). At lower discharges, the inception point was more defined than at higher discharges because in high discharges, the boundary layer cannot reach the free surface at little distances, and the non-aerated region dominates large portions of the flow in the spillway.

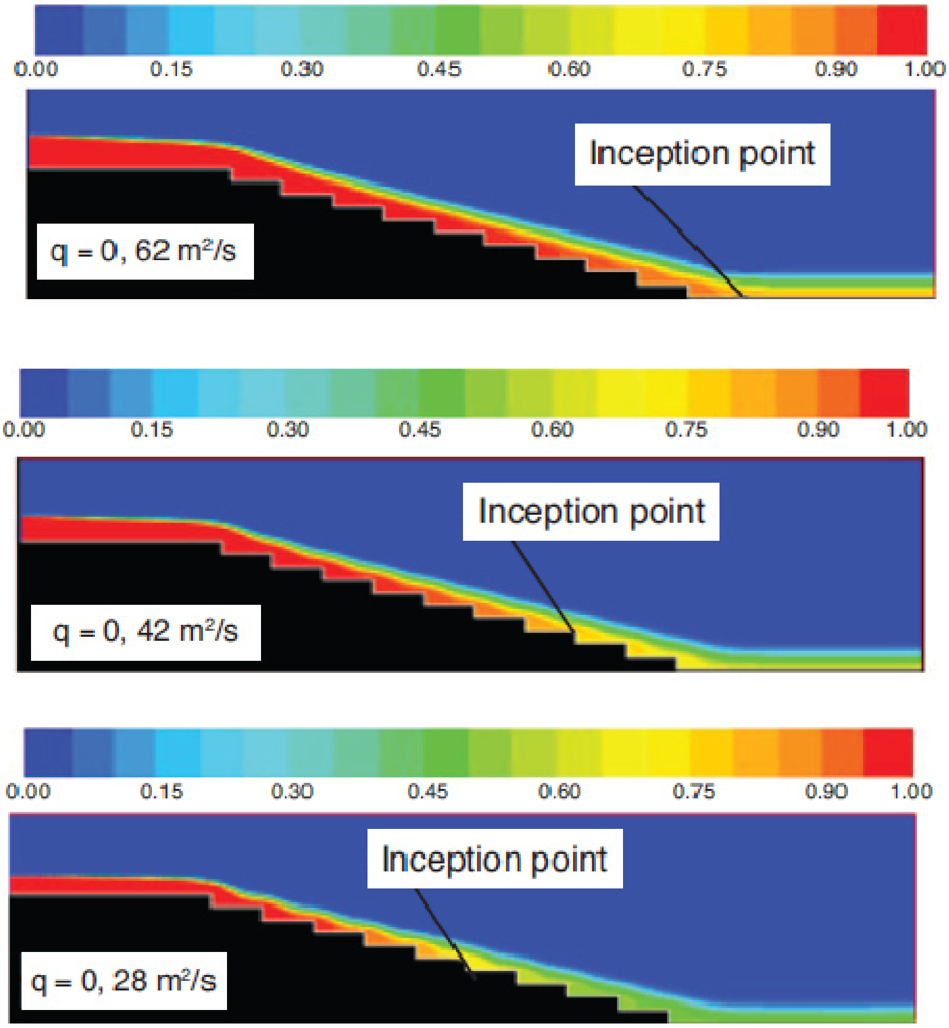

Figure III.7: Numerical computation volume fraction of water for different discharges

In this study, several positions of the inception point are computed and compared with the existing experimental results (Hunt and Kadavy 2009) as well as with those predicted by the formula of Chanson (1994a, 2001). The latter is a function of unit discharge, gravitation acceleration, channel slope ($\theta \geq 22°$) and step height:

$$L_{i^*} = 9.719\,(\sin\theta)^{0.0796}(\mathrm{F}^*)^{0.713}\,\mathrm{k_s} \qquad (\mathrm{III}-5)$$

Where:

L_{i*} = distance from the crest spillway to the inception point

$k_s = h\ cos\theta$

h = step height

θ = channel slope

F* = Froude number defined in terms of the roughness height:

$F^* = q/[g(\sin\theta)\{\mathrm{k_s}\}^3]^{0.5}$

q = unit discharge

g = gravitational constant

Table III.2 summarises the position of the inception point found by Hunt and Kadavy (2009), Chanson (1994a,2001) and by using fluent, for unit discharge equal to 0.11, 0.20, 0.28, 0.42, 0.62, 0.82 m^2/s. In Table III.2 and Figure III.8 the comparison of computed inception point with those from experimental equation of chanson and observed by Hunt and Kadavy **(2009)** is presented.

Table III.2: Observed, calculated and computed inception point location

q (m^2/s)	h (mm)	F*	Hunt and kadavy (2009)	Chanson (1994a,2001)	Computed inception point
			L_i (m)	**L_{i*}(m)**	**L_{i**} (m)**
0.82	38	75.2	7.1	7.0	No air entrainment
0.62	38	56.3	6.6	5.7	6.4
0.42	38	38.3	4.6	4.3	4.4
0.28	38	25.7	3.5	3.2	3.3
0.20	38	18.6	2.7	2.6	2.5
0.11	38	9.8	1.4	1.7	1.3
0.82	76	26.3	6.28	6.61	6.5
0.62	76	19.9	5.32	5.41	5.7
0.42	76	13.5	3.76	4.12	4.1
0.28	76	9.1	2.82	3.11	3.1
0.20	76	6.6	1.87	2.47	2.1
0.11	76	3.5	1.09	1.55	1.3
0.82	152	9.4	5.62	6.34	6.1
0.62	152	7.1	4.39	5.17	4.9
0.42	152	4.8	3.12	3.94	3.7
0.28	152	3.2	2.20	2.94	2.50
0.20	152	2.3	1.57	2.36	1.9
0.11	152	1.2	0.94	1.48	1.1

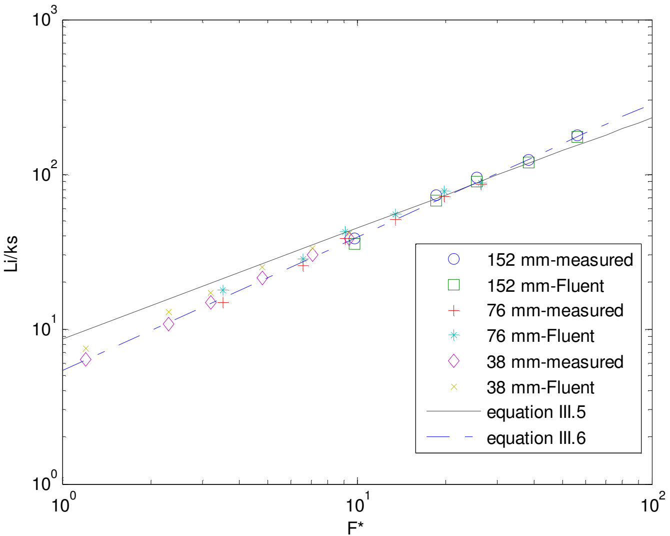

Figure III.8: Normalized L_i versus Froude surface roughness, F^*

Table III.2 and Figure III.8 show good agreement between the observed and computed inception point locations. As can be seen from this table, by increasing of the step heights, the difference between calculated inception point and computed inception, and measured inception point also increased. Figure 5 illustrates that Chanson's relationship appears to more closely predict the distance from the crest to the inception point when Froude surface roughness (F*) ranging from 10 to 100 correspond to step heights of 38 mm and 76 mm. Hunt and Kadavy (2009) proposed new relationships for determining the inception point for F_* ranging from 1 to 100 with slopes little or equal than 22°. This formula was plotted in figure III.8:

$$L_{i^*} = 6.1\,(\sin\theta)^{0.08}(\mathrm{F}^*)^{0.86}\,k_s \qquad (\mathrm{III}-6)$$

III.3.3 Air concentration

Downstream of the inception point of free-surface aeration, air and water are fully mixed, forming a homogeneous two-phase flow. In skimming flow, the air concentration distribution may be described by an analytical solution of the air bubble advective diffusion equation:

$$C = 1 - tanh^2\left(K'' - \frac{\frac{y}{Y_{90}}}{2D_0} + \frac{\left(\frac{y}{Y_{90}} - \frac{1}{3}\right)^3}{3D_0} \right) \qquad (III-7)$$

where y is distance measured normal to the pseudo-invert, Y_{90} is the characteristic distance where C = 90%, K is an integration constant and D_o is a function of the of the mean air concentration C_{mean} (Chanson, 1995 and 2001).

In figure III.9, the computed air concentration profiles downstream of the inception point is compared with experimental data Chanson.H and Toombes.L (2001) and with equation (III-7) at different locations for discharge of 0.182 (m^3/s).

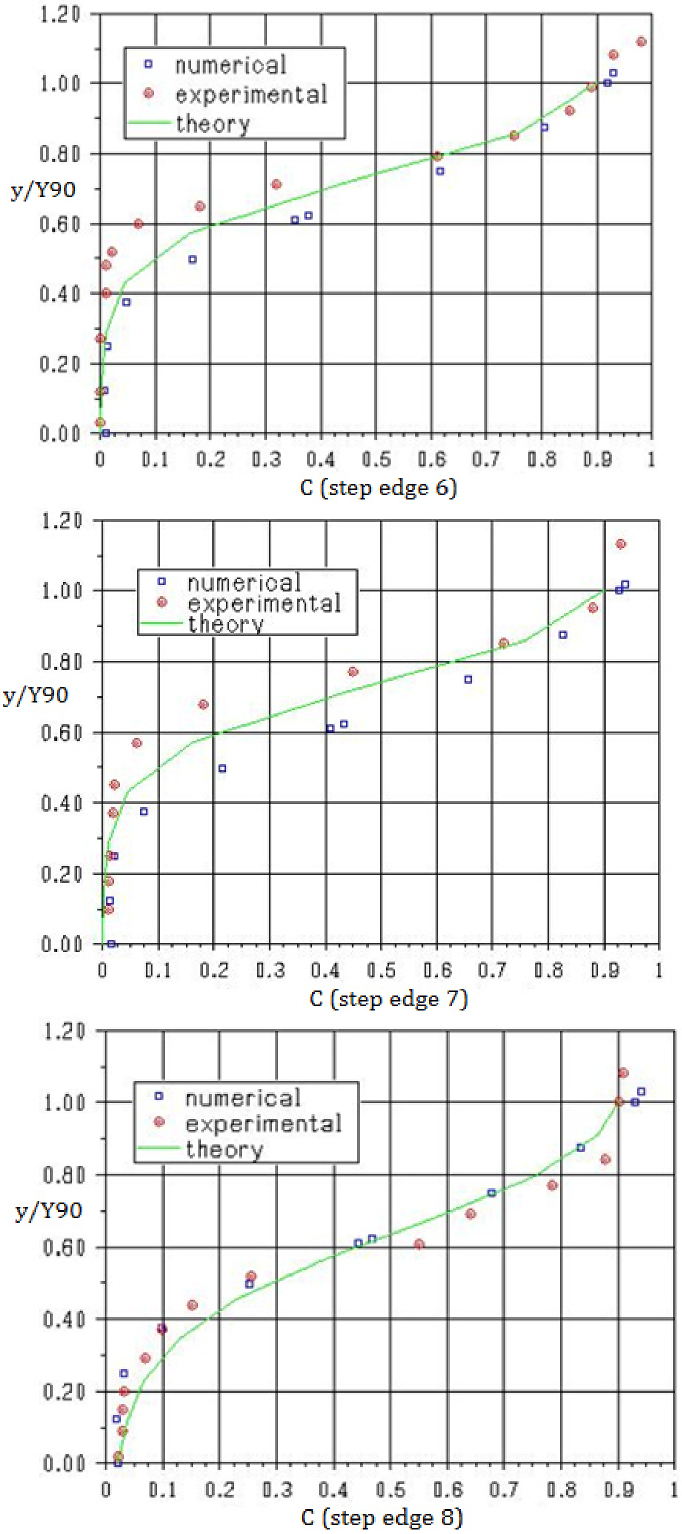

Figure III.9: Experimental and computational air concentration distribution compared with equation (III.7)

As can be seen, there are little differences between the numerical and experimental results because the VOF model underestimate the value of air concentration (Afshin and Mitra 2012). Equation III-7 compares favourably with the numerical and experimental air concentration profiles.

III.3.4 Velocity distribution

The velocity distribution in stepped spillway of Hunt and Kadavy (2009) and Chanson and Toombes (2001) is shown in figure III.10 and III.11 respectively. The velocity is higher in aerated region because the entrained air reduces wall friction; also the fluid is accelerated by the gravity along the chute. The recirculation flow which dissipates the energy in step corner is presented in figure III.12. Most of the energy is dissipated by momentum transfer between the skimming flow and the eddy in the interior of the step.

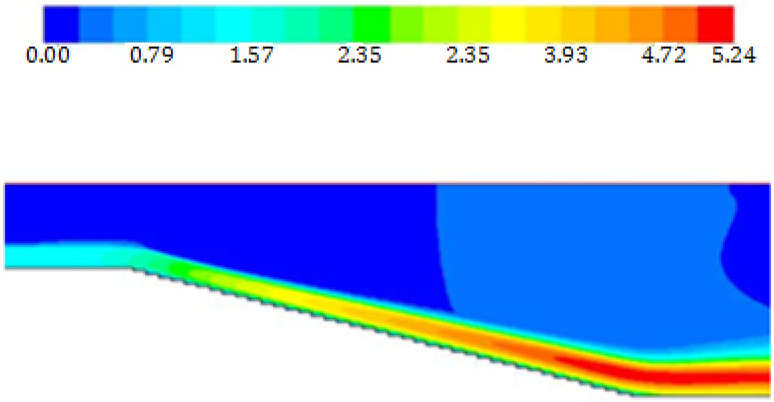

Figure III.10: Velocity distribution along the stepped spillway of Hunt and Kadavy for $q=0.28m^2/s$

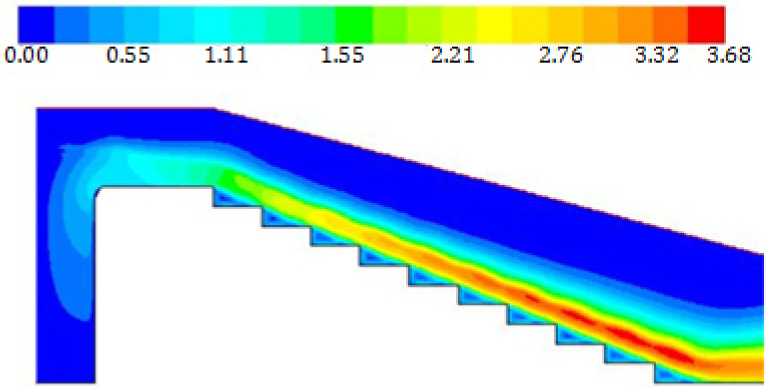

Figure III.11: Velocity distribution along the stepped spillway of Chanson and Toombes for $q=0.128m^2/s$

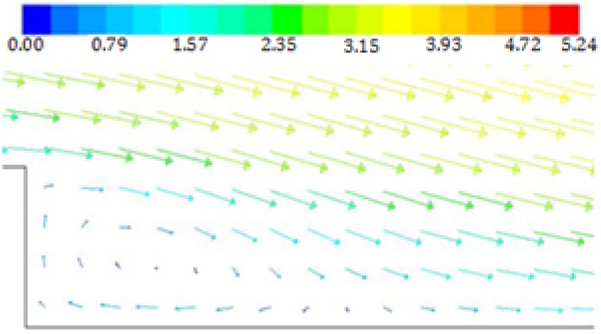

Figure III.12: Velocity vectors on one step for q=0.28m^2/s and h=38 mm

III.3.4.1 Velocity profile upstream of the inception point

In figure III.13, the one sixth power law with velocity was compared by velocity profiles obtained with fluent and the experimental velocity profiles measured by Hunt and Kadavy(**2010a**) at different distances from spillway crest 0.0, 1.22 and 3.05m respectively for q=0.28m^2/s.

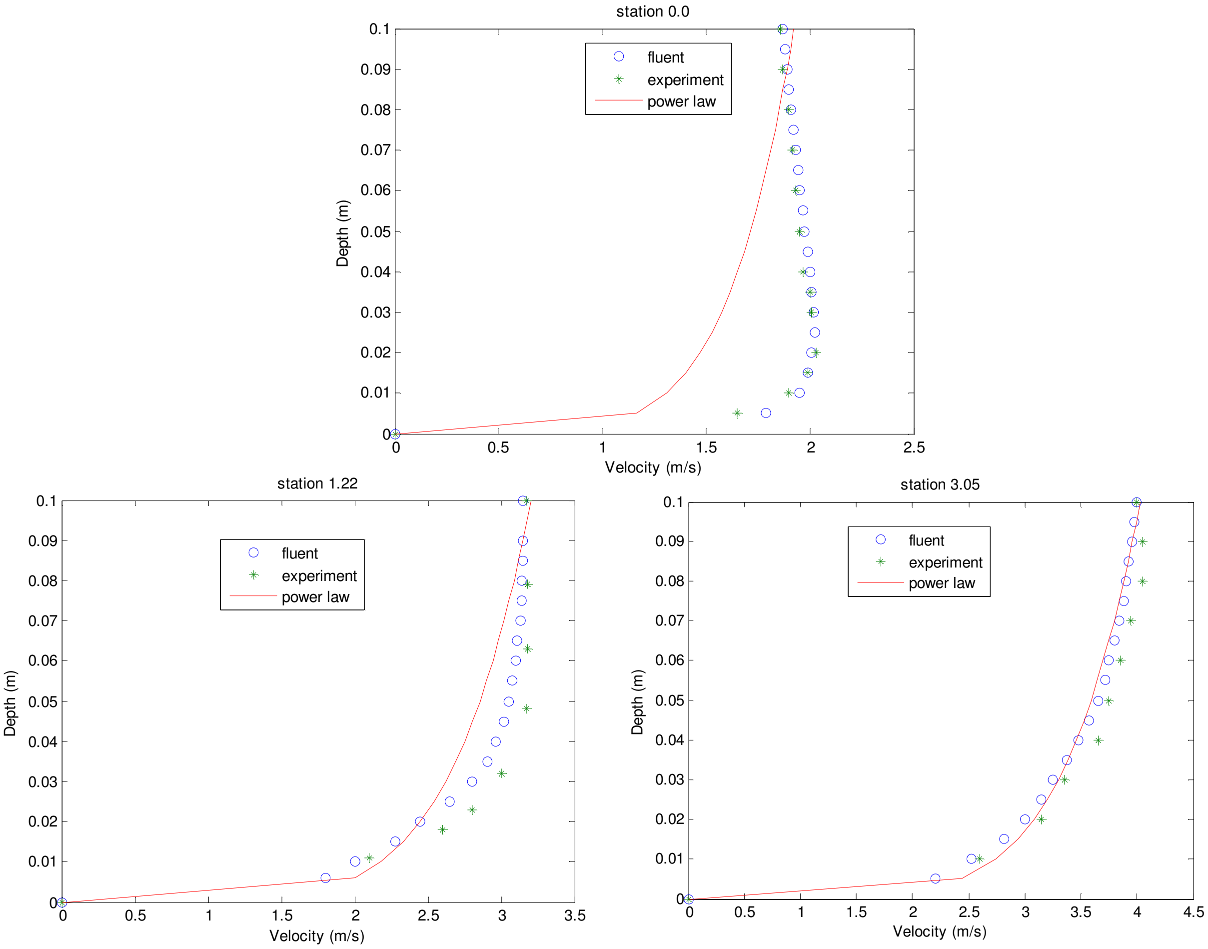

Figure III.13: Comparison of the one sixth power law with a Velocity obtained by simulation and measurement in Hunt and Kadavy, for q=0,28 m^2/s and h=38mm

This figure shows good agreement between experiments and simulations. The velocity profiles are uniform at the crest and trend toward a one sixth power law distribution near the inception point. Chanson (2001) found from experiments that the velocity profiles tended to follow a one-sixth power law distribution:

$$\frac{V}{V_{max}} = \left(\frac{y}{\delta}\right)^{1/6} \quad 0 \leq y/\delta \leq 1 \qquad (\text{III} - 8)$$

Where V_{max} is the free-stream velocity; *y* is the transverse coordinate originating at the pseudo-bottom and δ is the boundary layer thickness defined as the perpendicular distance from the pseudo-bottom to the point where the velocity is 0.99 V_{max}

III.3.4.1 Velocity profile downstream of the inception point

The air- water velocity profile at step edge is presented in figure III.14 for q=0,182 m^2/s. The percentage difference between numerical and experimental data was less than 13%. In the skimming flow, the velocity profile increase from the pseudo bottom at the free surface flow.

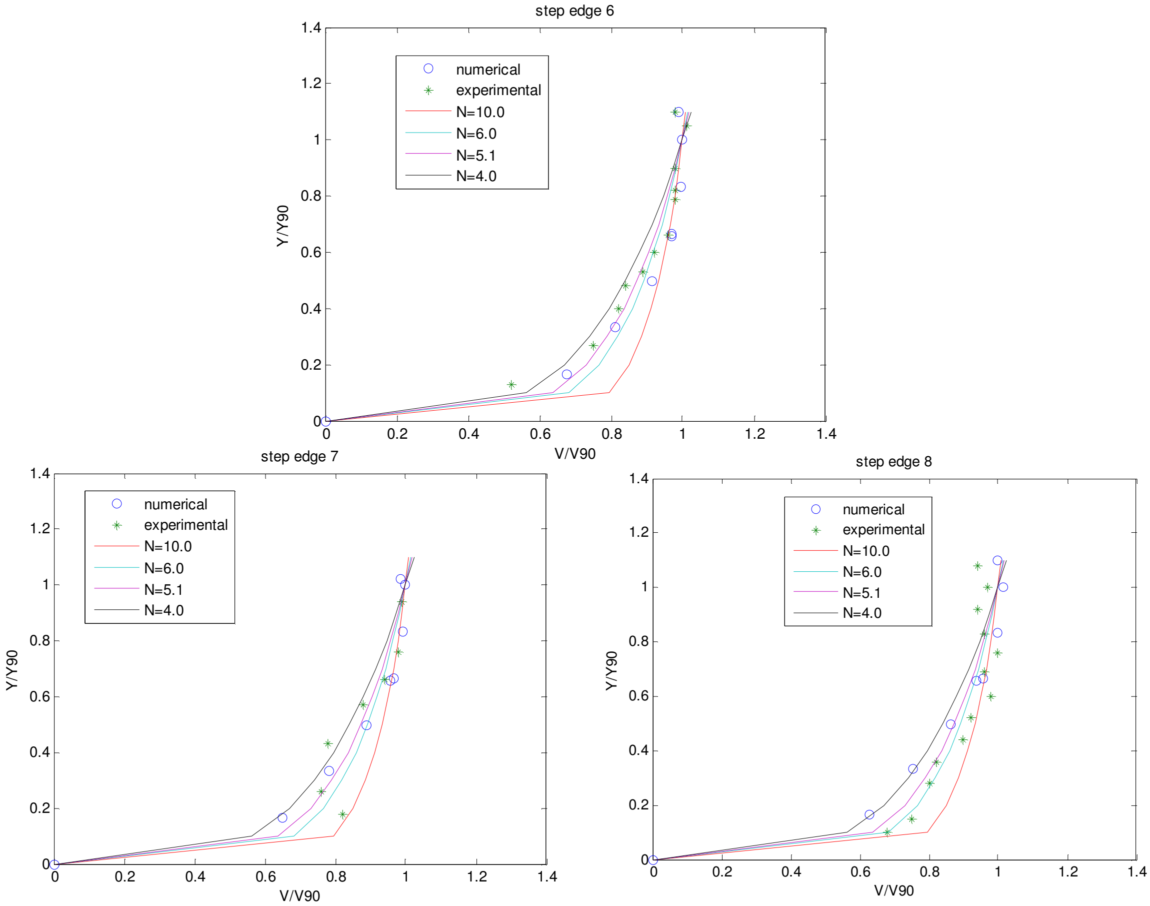

Figure III.14: Comparison of the power law with a Velocity obtained by simulation and measurement in Chanson and Toombes, for q=0,128 m^2/s

Based on previous study's **[3, 11, and 13]**, the distribution of air-water velocity follows a power law given by:

$$\frac{V}{V_{90}} = \left(\frac{y}{Y_{90}}\right)^{1/n} \qquad (III-9)$$

Where V_{90} is the characteristic velocity for C = 90%.The exponent n is obtained from experiments data. Chanson and Toombes (2001) found n = 5.1 and 6 for y_c/h values of 1.5 and 1.1, respectively. Hunt and Kadavy(2010b) taken n=6.0 with slope 14°. Matos (in Chanson and Toombes 2001) obtained n = 4. Felder and Chanson (2011) proposed n=10 for y/Y90<1. This figure showed that the velocity profiles follow a power law distribution with n=6.0 and n=5.1 at and downstream of the inception point.

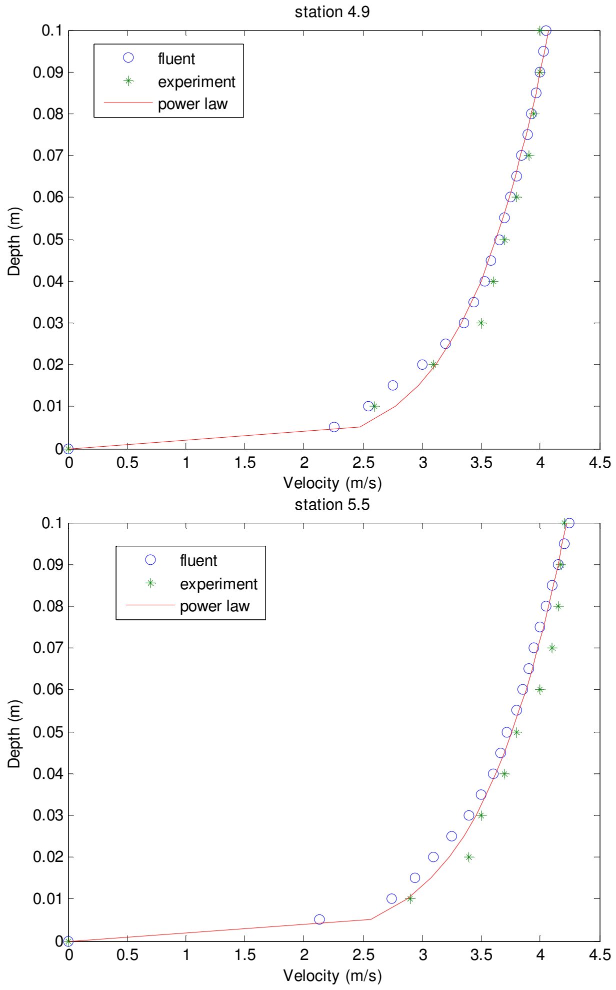

Figure III.15: Comparison of the one sixth power law with a Velocity obtained by simulation and measurement in Hunt and Kadavy, for q=0,28 m^2/s and h=38mm

A one-sixth power law is compared successfully with experimental results obtained by Hunt and Kadavy (2010b) and numerical results at different distances from spillway crest 4.9 and 5.5m respectively for $q=0,28m^2/s$ (e.g figure III.15).

III.3.5 Turbulence kinetic energy and turbulence dissipation

The figure III.16 and III.17 are the contours of Turbulence kinetic energy (k) and turbulence dissipation (ε) respectively. As shown in them, the distribution of the turbulence kinetic energy is nearly the same as that of turbulence dissipation. As can be seen from figure (III.16), the maximum of k is located near the pseudo-bottom as a region of formation and growth of recirculating vortices. Also it can be observed the increasing of turbulent kinetic energy along the stepped spillway which is the result of the development of the boundary layer. A gradual decrease of *k* is observed near the water surface, where the flow can be considered irrotational. This result is qualitatively similar to those presented by Bombardelli et al. (2010).

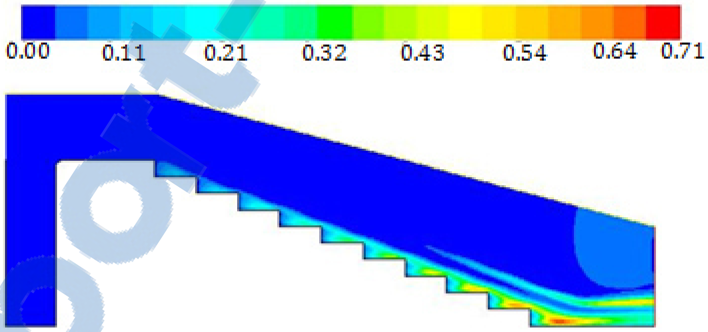

Figure III.16: Kinetic turbulent energy distribution

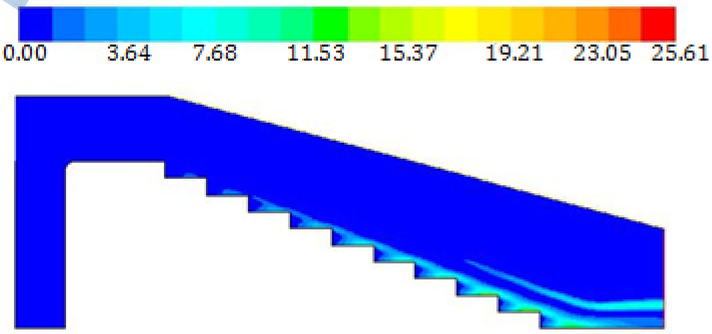

Figure III.17: Turbulent dissipation distribution

III.3.6 Pressure distribution

The pressure distributions down the steps are important to study the risk of cavitation in stepped channel; figure III.18 illustrates the contours of pressure in step corner. This figure indicate that the minimum value of pressure is located in the vertical wall of the step, is due by separation flow between skimming flow and the eddy in this region. Also maximum pressure exists in the horizontal surface of the step. This maximum pressure is caused by the impact of the skimming flow coming from upper step.

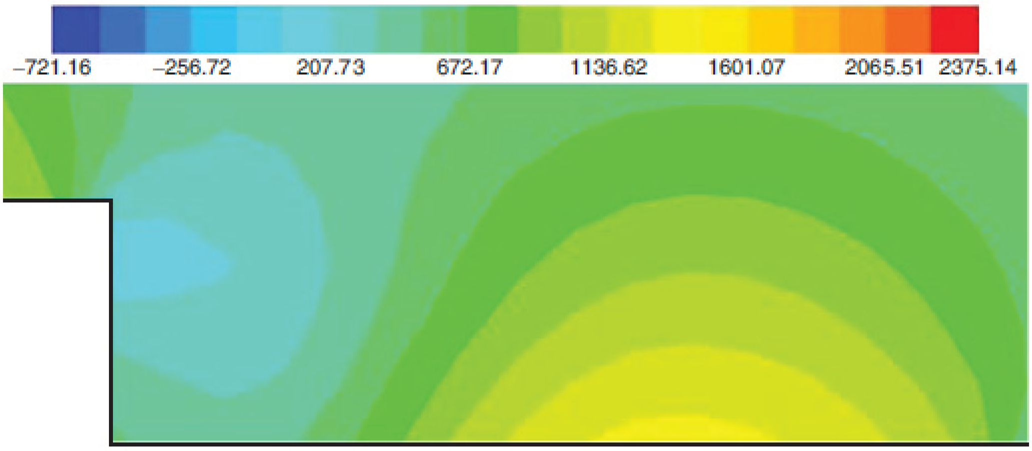

Figure III.18: Pressure contours on one step

Introduction

Many experimental studies have been conducted on stepped spillways with uniform flat steps to quantify the energy dissipation and to study some characteristic flow regime. But some spillways are equipped with non uniform step heights. Stephenson (in Felder and Chanson 2001) observed an increase in energy dissipation of 10% in experimental test of non uniform step height. This chapter presents the results of numerical simulation flow in stepped spillway with non uniform step height obtained by using Fluent computational fluid dynamics (2006) to show these effects on the air-water flow properties.

IV.1 Description of physical model

A physical model of stepped spillway provided by Felder (2013) is shown in figure IV.1. The non-uniform stepped spillways were equipped with a combination of steps with 5 & 10 cm step heights and is characterised by regular alternation of one 10 cm step followed by two 5 cm steps. The channel slope is 26.6°.

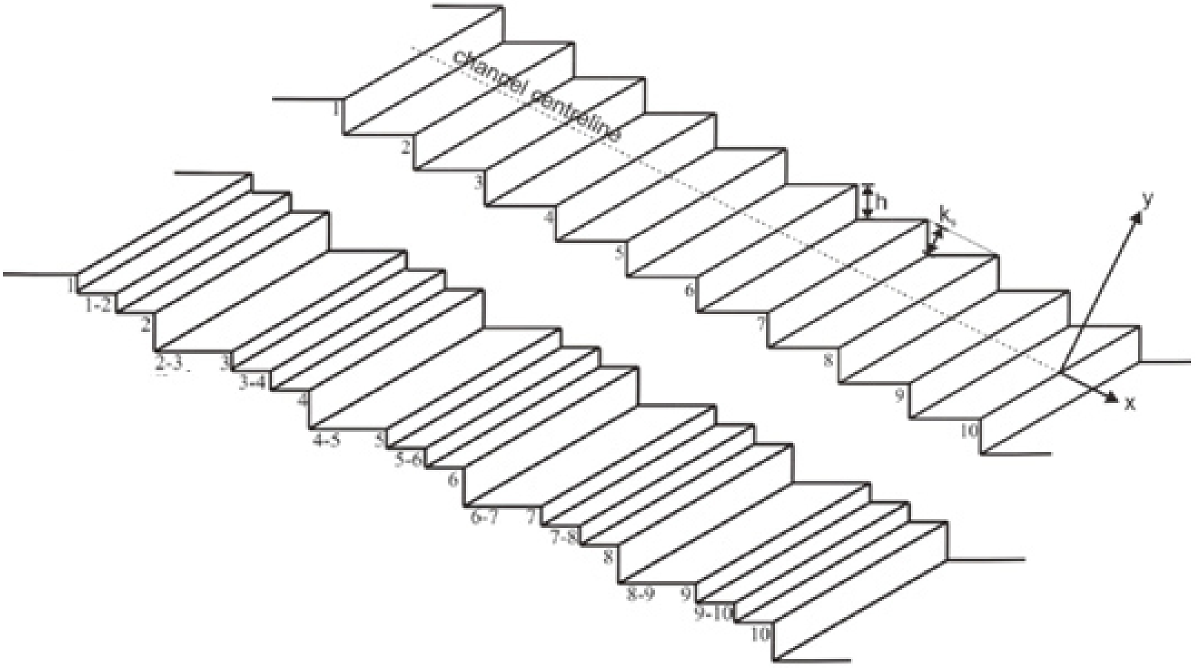

Figure IV.1: Uniform and non-uniform stepped spillway configuration

IV.2 Meshing the Geometry and boundary conditions

The GAMBIT software was used to create and mesh the geometry. The physical model of Felder.S (2013) was divided into unstructured grids (triangular cell) that had a high adaptability to the complex geometry and boundary. Triangular meshes with 0.015 m^2 are used (**figure IV.2**). The boundary conditions in this study are shown in figure IV.2.

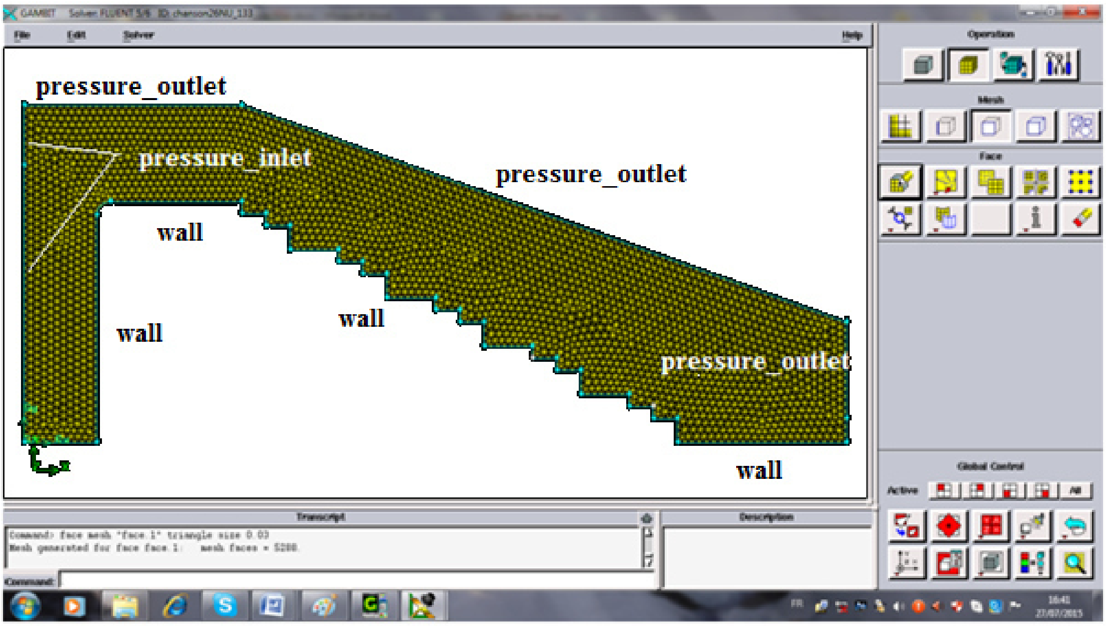

```
Command> face mesh "face.1" triangle size 0.03
Mesh generated for face face.1:   mesh faces = 5200
```

Figure IV.2: Grid and boundary condition

Fluent computational fluid dynamics (CFD) is used to solve Navier-Stokes equations. The standard $k - \varepsilon$ model is used to simulate turbulence. The volume fraction, momentum and turbulence closure equations were discretized by employing a conservative, second-order accurate upwind scheme. The pressure-velocity coupling algorithm is the pressure-implicit with splitting of operators (PISO). The viscosity layer near to the wall dealt with the standard wall function. The numerical values of boundary conditions are listed in Table IV.1.

Table IV.1: Inflow conditions

model	**q (m^2/s)**	**U (m/s)**	**h (m)**	**I (-)**	**k $\times 10^{-4}$ (m^2/s^2)**	**ε$\times 10^{-6}$ (m^2/s^3)**
Felder (2013)	0,025	0.024	1.05	0.0451	0.0173	0.00508
	0,069	0.063	1.099	0.0397	0.0933	0.06096
	0,116	0.101	1.14	0.0372	0.2154	0.2059
	0,122	0.108	1.145	0.0366	0.2673	0.235
	0,133	0.115	1.15	0.0369	0.2394	0.2814

IV.3Results and discussion

On uniform stepped spillway, nappe flow occurs for the smallest flow rates. For an intermediate range of flow rates, a transition flow regime is observed. For higher discharge value, the water skims over the pseudo-bottom formed by the step edges as a coherent stream. Beneath the pseudo-bottom, intense recirculation vortices fill the cavities between all step edges. The aim of this work is assess the effects of non-uniform step heights on the air-water flow properties down a stepped chute.

In the present study, The CFD solver FLUENT is used to simulate flow over stepped spillway of non uniform step heights. Three flow regimes over non-uniform steps are shown in figures IV.3.

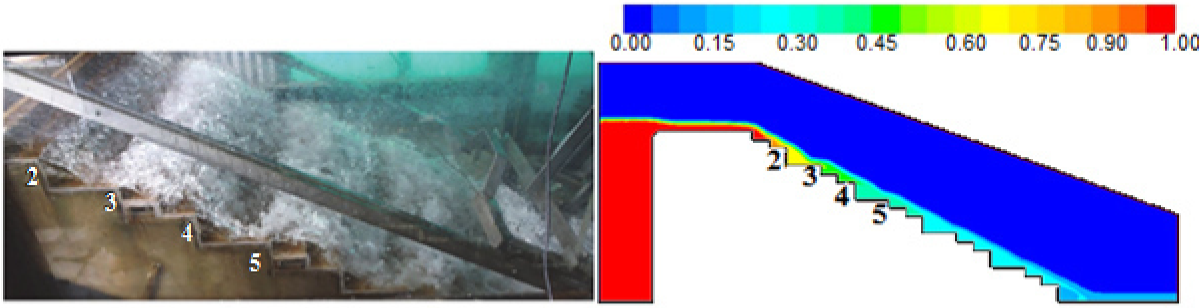

(A) Nappe flows: q = 0.025 m^2/s;

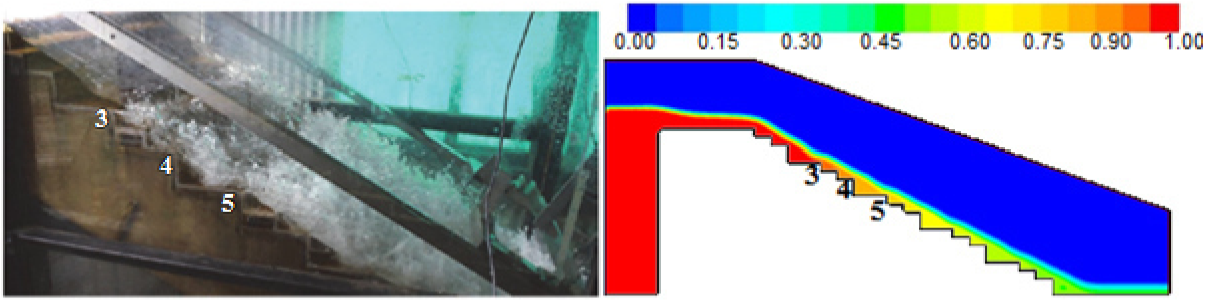

(B) Transition flows: q = 0.069 m^2/s

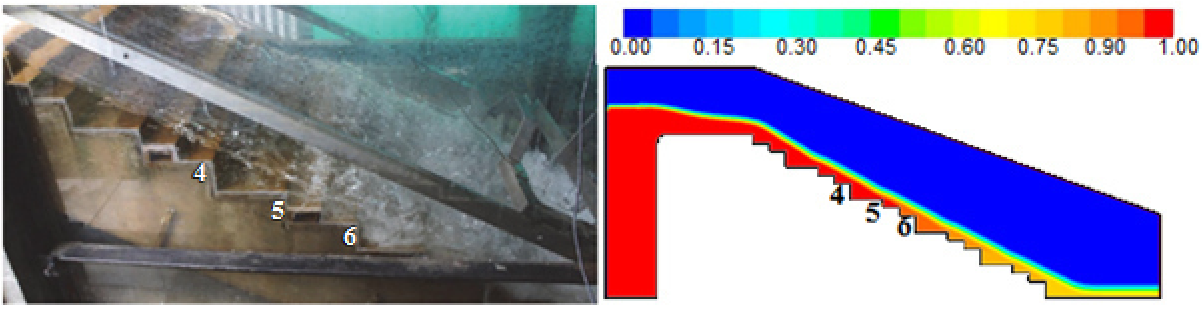

(C) Skimming flows: q = 0.133 m^2/s

Figure IV.3: Observed and computed flow regime on non uniform step height

Seen from these figures, good agreement between observed and computed flow regime, also the simulated inception point is well agreed with that of measurement. Figure IV.3 indicates that, the air entrainment started on step edge N°2, for nappe flow and on step edge N° 3 for transition flow. In skimming flow, the location of the inception point is clearly shown between step N° 5 and N°6. It is clear that, the inception point moves toward the basin floor when the discharge increases.

Figure IV.4 gives numerical void fraction of water on the uniform and non uniform stepped spillways with 26.6° slope.

The observations of the air-water flow patterns on the non-uniform stepped spillways showed that the non uniform configurations were close to the uniform stepped spillway with 10 cm high steps. The results indicated that the non uniform stepped configurations did not have any impact on the location of the inception point of air entrainment.

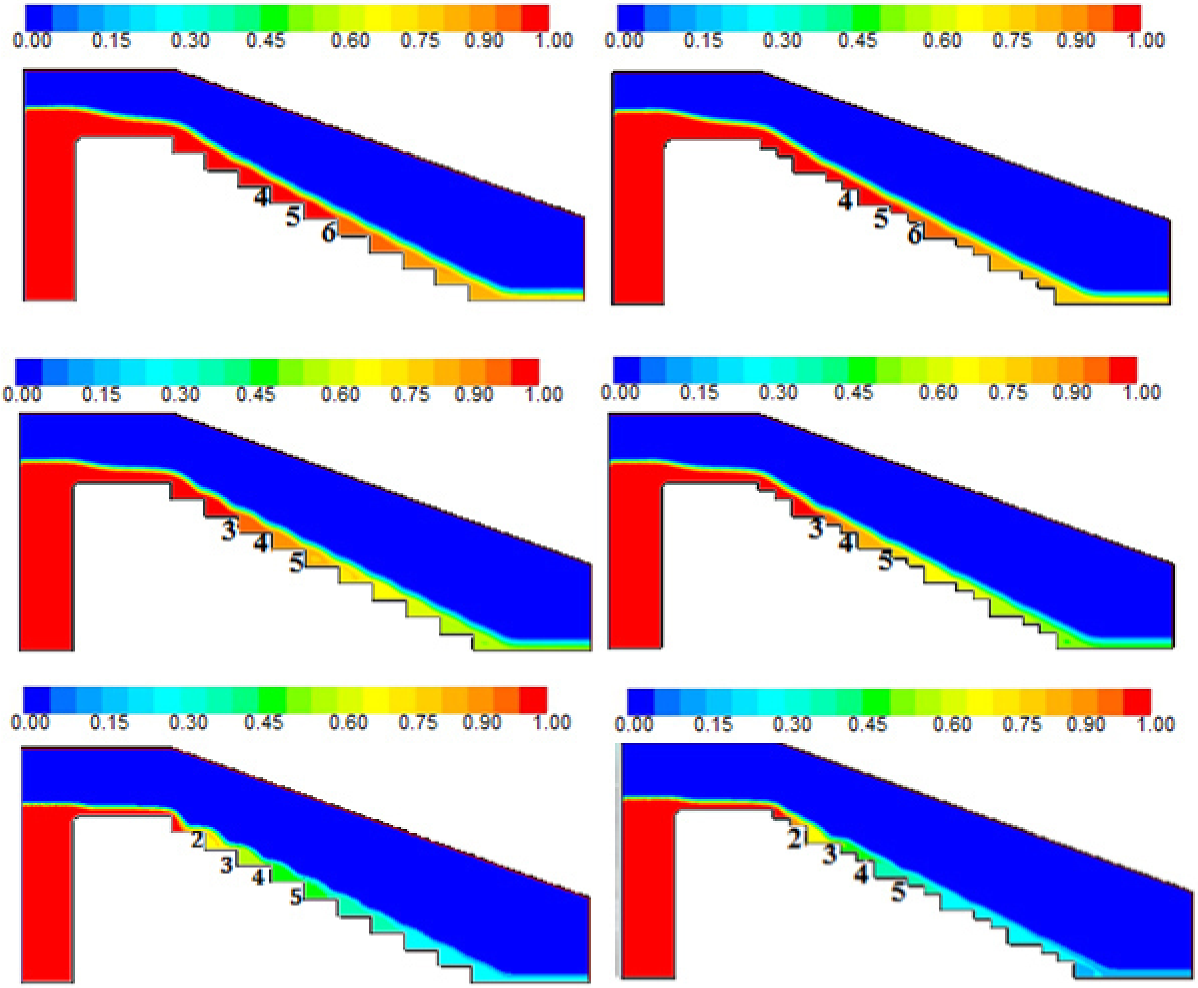

Figure IV.4: Numerical void fraction of water on the uniform and non uniform stepped spillways

III.3.1 Void fraction and velocity profile

The non-uniform distributions of void fraction were compared with the corresponding uniform stepped spillway results (Figure IV.5).

The void fraction distributions for the non-uniform and the corresponding uniform steps with h = 10 cm were in relatively close agreement, but scatter of the void fraction distribution shapes was observed for the non-uniform stepped spillways. The configurations with the non-uniform step heights showed some larger air concentration compared to the uniform stepped spillways which might be caused by stronger instabilities of the flow.

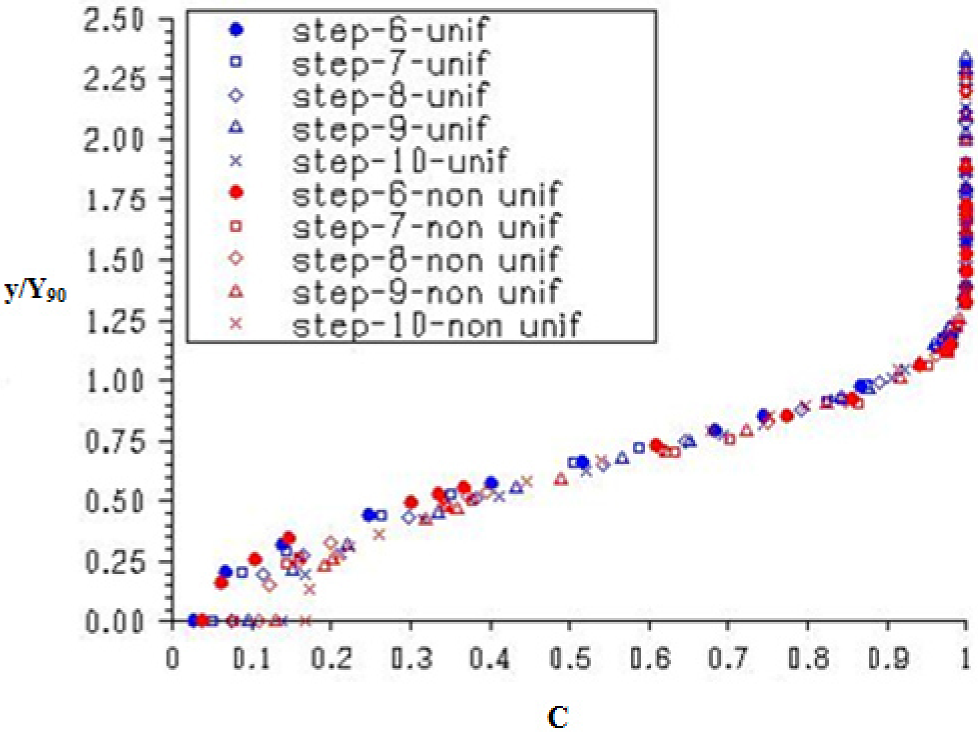

Figure IV.5: Computational air concentration distribution on uniform and non uniform configurations

The air- water velocity profile at step edge is presented in figure (IV.6) for q=0,122 m^2/s. This figure show same profile of velocity on the uniform and the non uniform configurations and it increases from the pseudo bottom at the free surface flow.

Felder and Chanson (2011) compared the velocity profile with 1/10th power law correlation for $y/Y_{90} < 1$ and a uniform profile for $y/Y_{90} \geq 1$. We found that, the Velocity profile matched well with one-sixth power law (seen figure IV.6).

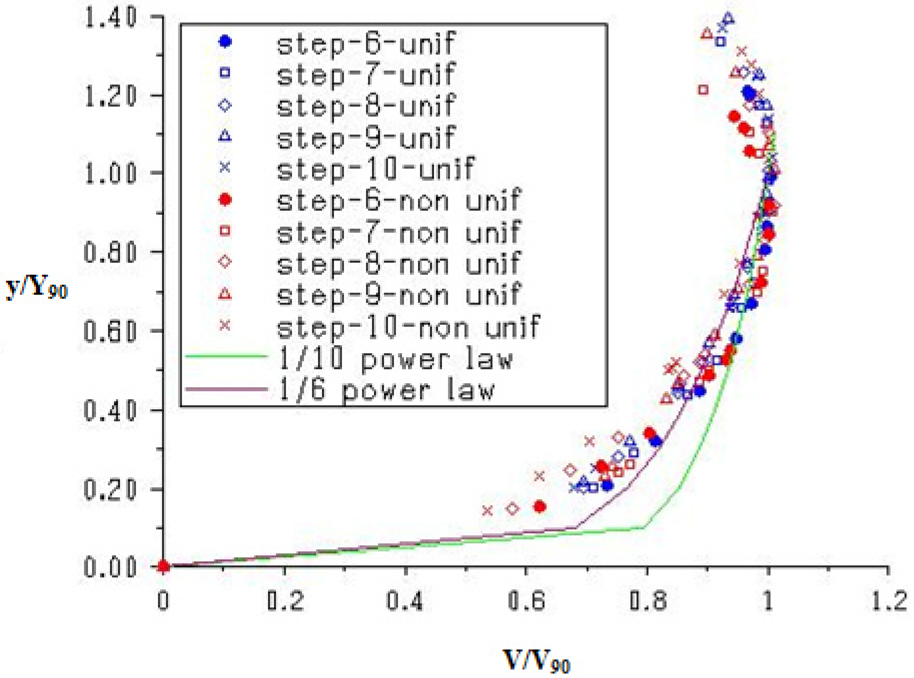

Figure IV.6: Dimensionless velocity on uniform and non uniform configurations

Air concentration distributions and velocity profile, measured by Felder and Chanson (2011) is presented in Figure (IV.7). The air concentration distributions obtained by simulation (figure IV.5) agree with measurement results.

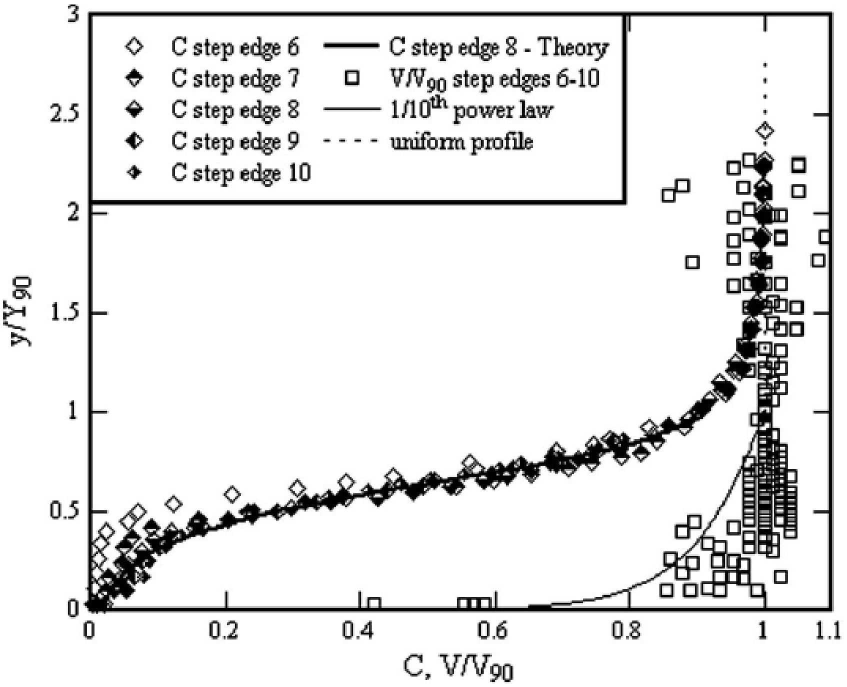

Figure IV.7: Dimensionless velocity and air concentration measured by Felder and Chanson (2011)

For the velocity profile, there is some difference between the simulation and measurement when $y/Y_{90}<0,5$. The numerical solution seems to produce slightly more uniform velocity profiles than observed, which could in principle be associated with the pseudo-bottom normal diffusion generated by the turbulence closure. Differences may also stem from three-dimensional flow structures and effects that are not captured in a 2D simulation such as vortex stretching and self-induced velocity which contributes to “dissipate” eddies in 3D (Bombardelli et *al* 2010).

IV.3.2 Velocity distribution

The velocity distribution on the uniform and the non uniform stepped spillway are compared in figure (IV.8).

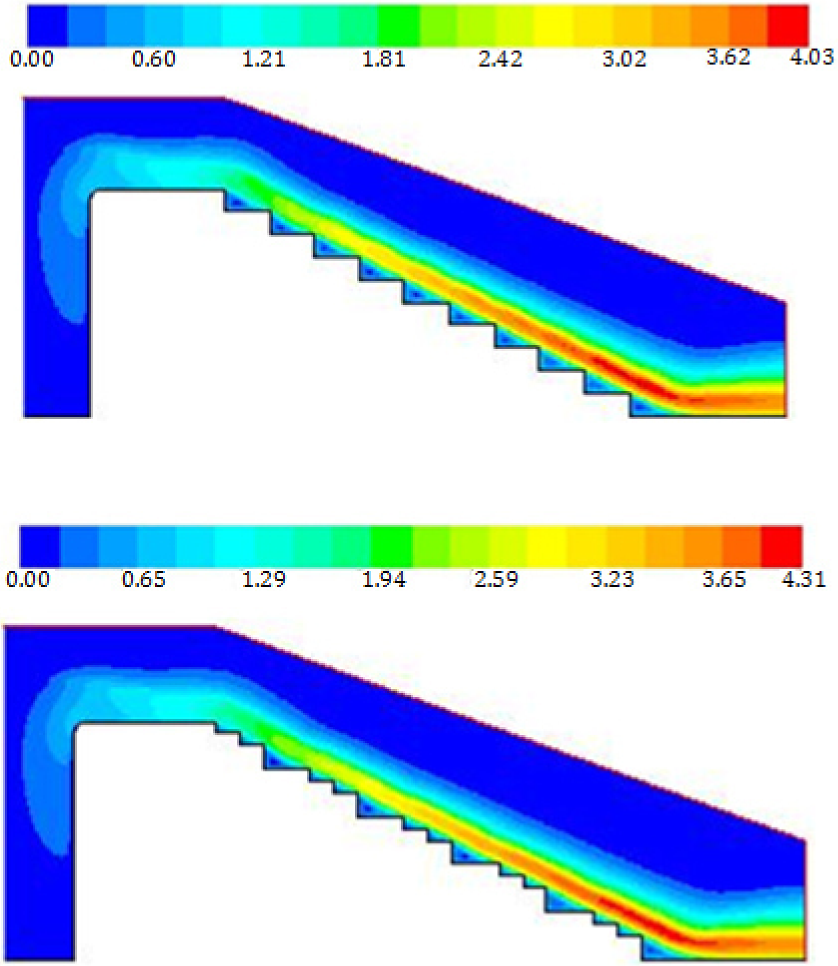

Figure IV.8: Velocity distribution on uniform and non uniform configurations

The maximum velocity from non uniform configuration is some great than in uniform configuration which the recirculating vortices are more developed (seen figure IV.9). Thus, the stepped spillway with uniform step heights is more efficient than with non uniform step heights in reducing the flow velocity and in dissipation of energy. Felder and Chanson (2011) showed from experiment that, the configuration with non-uniform step heights did not yield any advantages in terms of energy dissipation performances.

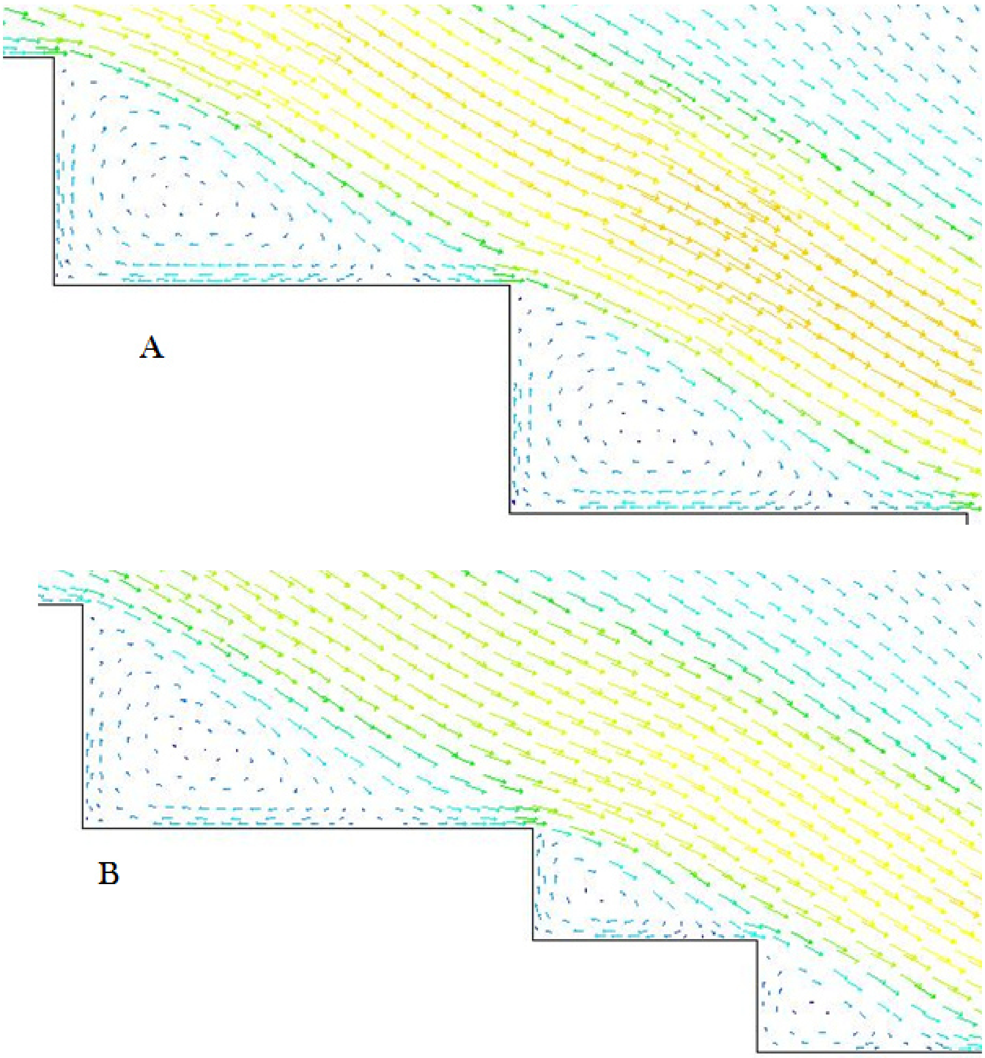

Figure IV.9: Recirculation flow in step corner, A: uniform configuration, B: non uniform configuration

IV.3.3 Turbulence kinetic energy

Figure (IV.10) present a comparison of turbulence kinetic energy on the uniform and non uniform stepped spillway.

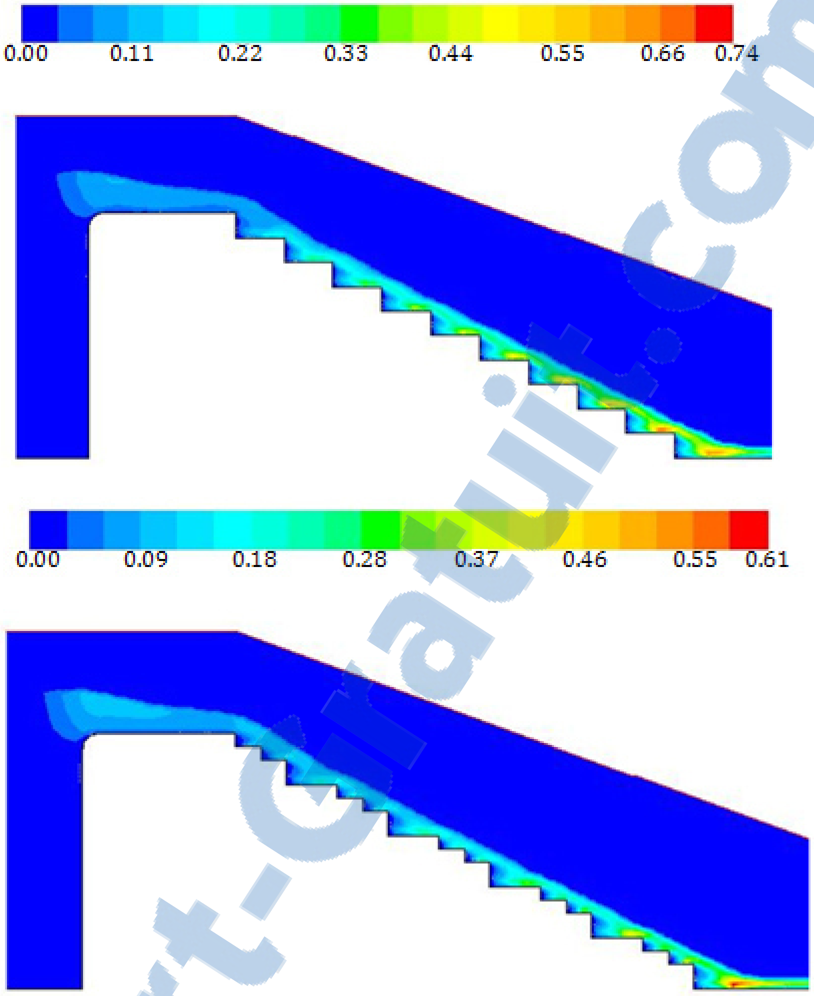

Figure IV.10: Turbulence kinetic energy on uniform and non uniform configurations

The kinetic energy of turbulence on the uniform stepped spillway was largest for most step edges. The roughness height which is $k_s = h \cos\theta$ is great on uniform configuration and the kinetic energy of turbulence increased with the surface roughness. It means that, the recirculating vortices located in the triangular zone of the step corner are higher in uniform stepped spillway.

IV.3.3 Pressure distribution

In order to evaluate the risk of cavitation in stepped channel; figure (IV.11) and figure (IV.12) show the contour of pressure on the uniform and non uniform stepped spillway for q=0.133 m^2/s. According to figure (IV.11) and (IV.12), the maximum value of negative pressure is appeared in non uniform configuration and is located in the steps edges for the 5 cm high. The cavitation on chutes is initiated for high velocity flows and it is known that the velocity in non uniform configuration is higher than the uniform configuration. Thus, the stepped spillway with uniform step heights is more protect than with non uniform step heights in risk of cavitation.

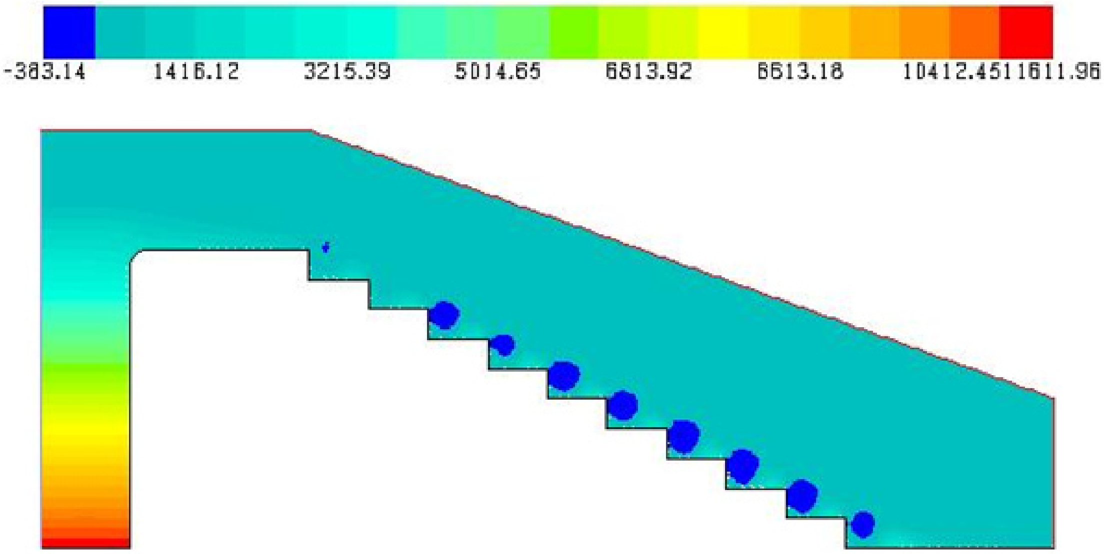

Figure IV.11: Contour of static pressure on uniform stepped spillway

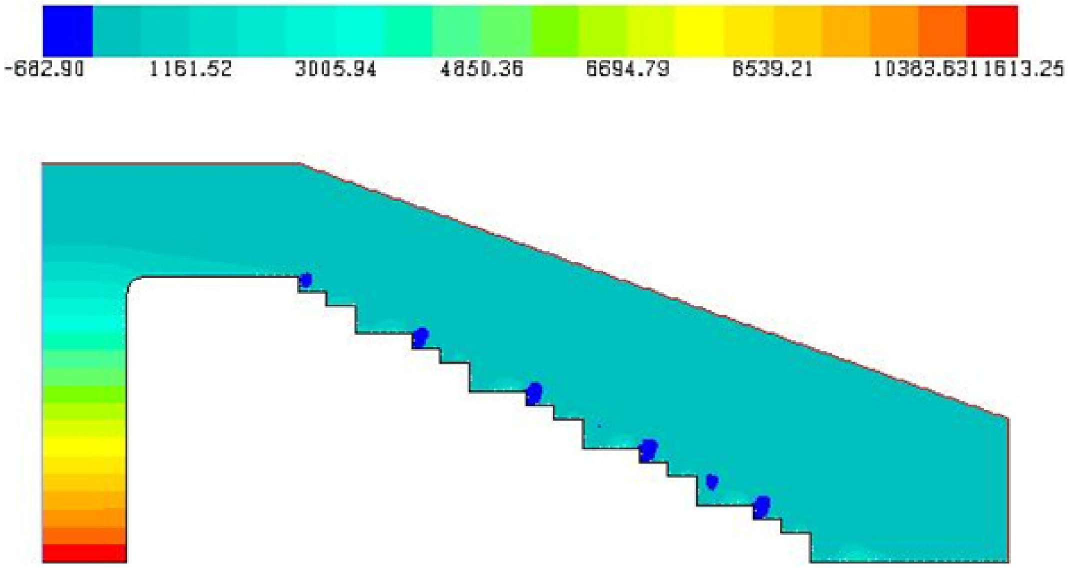

Figure IV.12: Contour of static pressure on non uniform stepped spillway

Stepped spillways are characterised by a large energy dissipation and aeration performance. These features can be advantageous for designs of flood release facilities of hydraulic structures decreasing the size of the downstream stilling basin. The topic of the flow over stepped spillway was the object of several experimental works, with the development of computational fluid dynamics (CFD) branch, flow over stepped spillway can be simulated to validate experimental results.

In the present numerical study, flow over stepped spillway was simulated by using fluent. Free surface was treated by VOF model and turbulence flow was estimated by k-ε Standard Model. This work focused on the uniform and non uniform steps height. The experimental studies are used to validate the numerical results of the air-water two-phase flow over the stepped spillway. The experimental data by Hunt and Kadavy (2009,2010a) and Chanson, H. and Toombes, L. (2001) were used for validation of flow simulation over the stepped spillway with uniform step height and the experiments study's of Felder (2013) and of Felder and Chanson (2011) are used for the non uniform configuration.

Good agreement is found between numerical and experimental results. On the basis of results, the following conclusions can be drawn:

1. The transition flow observe for the low range of water discharge and the skimming flow occur for upper range of water discharge;
2. The formula developed by Chanson (1994a, 2001) can be used to determine the location of the inception point on flat sloped stepped chute with Froude surface roughness (F*) ranging from 10 to 100;
3. The air concentration distribution may be described by an analytical solution of the air bubble advective diffusion equation;
4. The velocity profiles obey the one sixth power law distribution near the inception point and downstream of the inception point for the uniform step height;
5. The maximum of turbulent kinetic energy is found near the pseudo-bottom. Also, the kinetic energy turbulent increases along the stepped spillway which is the result of the development of the boundary layer;

6. Minimum and maximum pressure is located in the vertical and horizontal face of step;
7. The non uniform stepped configurations did not have any impact on the location of the inception point of air entrainment;
8. The configurations with the non-uniform step heights showed some larger air concentration compared to the uniform stepped spillways which might be caused by stronger instabilities of the flow;
9. The maximum velocity from non uniform configuration is some great than in uniform configuration;
10. The configuration with non-uniform step heights did not yield any advantages in terms of energy dissipation performances;
11. The maximum value of negative pressure is appeared in non uniform configuration and is located in the small steps edges, so, the stepped spillway with uniform step heights is more protect than with non uniform step heights in risk of cavitation;
12. The kinetic energy of turbulence on the uniform stepped spillway was largest for most step edges.

Lastly, the findings from this work are an indication that the FLUENT software is powerful tool to simulate the air-water flow and to help in the design of stepped spillway together with the physical model.

REFERENCES

Afshin Eghbalzadeh and Mitra Javan. (2012): “Comparison of Mixture and VOF Models for Numerical Simulation of Air–entrainment in Skimming Flow over Stepped Spillways”. Journal of Science Direct. Procedia engineering Vol.28, pp 657 – 66.

Benmamar,S. Kettab, A. and Thirriot, C. (2003): “Numerical simulation of turbulent flow upstream of the inception point in a stepped channel”. Proceedings,30th IAHR Congress. Auth, Thessaloniki, Greece: 679-686.

Boes, R. M. and W. H. Hager, (2003):”Two-phase flow characteristics of stepped spillways”. Journal of Hydraulic Engineering, ASCE, Vol.129, N°9, pp 661-670.

Bombardelli FA, Meireles I, Matos J, (2010): “Laboratory measurements and multi-block numerical simulations of the mean flow and turbulence in the non-aerated skimming flow region of steep stepped spillways”. Environ. Fluid Mech Vol.11, N°3, pp 263-288.

Carvalho, R. and Amador, A., (2008): “Physical and Numerical Investigation of the Skimming Flow over a Stepped Spillway”, Proceedings of the 16th IAHR-APD Congress and the 3rd Symposium of IAHR-ISHS, 20-23 October, Nanjing, China.

Chanson, H. (1994a): “Hydraulics of Nappe Flow Regime above Stepped Chutes and Spillways”. Australian. Civil Engineering. Transactions. I.E.Aust. CE36(1), 69–76.

Chanson, H, (1994b): “Hydraulics of skimming flows over stepped channels and spillways”. IAHR, Journal of Hydraulic. Research. Vol 32, N°3, pp 445-460.

Chanson, H. (1995): "Hydraulic Design of Stepped Cascades, Channels, Weirs and Spillways." Pergamon, Oxford, UK, Jan., 292 pages (ISBN 0-08-041918-6).

Chanson. H, (1997): “Air Bubble Entrainment in Free-Surface Turbulent Shear Flows”. Academic Press, London, UK, 401 pages ISBN 0-12-168110-6.

Chanson,H. (2000): “Characteristics of skimming flow over stepped spillways: Discussion”. Journal of Hydraulic Engineering, ASCE. Vol. 125, N°4, pp 862-865.

Chanson, H. (2001): "The Hydraulics of Stepped Chutes and Spillways." Balkema Publ., Rotterdam, The Netherlands. ISBN 90 5809 352 2.

Chanson, H. (2004): “The Hydraulics of Open Channel Flows: An Introduction.” Butterworth- Heinemann, Oxford, UK, 2nd edition,630 pages (ISBN 0750659785).

Chanson, H. and Toombes, L. (2001): “Experimental Investigations of Air Entrainment in Transition and Skimming Flows down a Stepped Chute. Application to Embankment Overflow Stepped Spillways,” Research Report No.CE158, Dept. of Civil Engineering., University of Queensland, Brisbane, Australia, July.

Chanson, H. and Toombes. L, (2002): “Air–water flows down stepped chutes: turbulence and flow structure observations”. International Journal of Multiphase Flow. Vol 28. pp 1737–1761.

Chanson, H. and Toombes, L.(2004): “Hydraulics of stepped chutes: the transition flow”. Journal of Hydraulic Research, Vol 42, N°1, pp 43–54.

Charles E.Rice and Kem C.Kadavy,(1996): “Model of A roller compacted concrete stepped spillway”. Journal of Hydraulic Engineering, ASCE, Vol 122, N°6,

pp 292-297.

Chen, Q., G.Q. Dai and H.W. Liu. (2002): “Volume of Fluid Model for Turbulence Numerical Simulation of Stepped Spillway Over Flow”. Journal of Hydraulic Engineering, ASCE. Vol. 128, N°7, pp 683-688.

Cheng Xiangju, Chen Yongcan and Luo Lin, (2006): “Numerical simulation of air-water two-phase flow over stepped spillways”. Science in China Series E, Technological Sciences, Vol 49, N° 6 ,pp 674-684

Chinnarasri. C, Kositgittiwong.K and. Julien. PY,(2012):” Model of flow over spillways by computational fluid dynamics”, Proceedings of the Institution of Civil Engineers, pp 1-12

Christodoulou,G.C. (1993): “Energy dissipation on stepped spillways”. Journal of Hydraulic Engineering, ASCE. Vol 119, N°5, pp 644-650.

Dermawan.V and Legono, D,(2011): “Residual energy and relative energy loss on stepped spillway”. Journal of Applied Technology in Environmental Sanitation, Vol. 1, N° 4, pp 381-392.

Duangrudee, K., (2012): “Validation of numerical model of the flow behaviour through smooth and stepped spillways using large-scale physical model” PHD Thesis, King Mongkut’s University of Technology Thonburi, Thailand

Felder, S. (2013): “Air-Water Flow Properties on Stepped Spillways for Embankment Dams: Aeration, Energy Dissipation and Turbulence on Uniform, Non-Uniform and Pooled Stepped Chutes”, Ph.D. thesis, School of Civil Engineering, The University of Queensland, Australia.

Felder, S. and Chanson, H. (2009): " Energy dissipation, flow resistance and gas-liquid interfacial area in skimming flows on moderate-slope stepped spillways." Environmental Fluid Mechanics, Vol. 9, N°4, pp. 427-441.

Felder, S. and Chanson, H. (2011): "Energy Dissipation down a Stepped Spillway with Non- Uniform Step Heights." Journal of Hydraulic Engineering, ASCE, Vol. 137, N° 11, pp. 1543- 1548 .

Fluent, (2006): “Manuel and user guide, Fluent Inc”

Gonzalez, C.A. and Chanson, H. (2007): “Hydraulic Design of Stepped Spillways and Downstream Energy Dissipators for Embankment Dams”, Dam Engineering,Vol 17, N°4, pp 223-244

Hager, W.H. (1983): “Hydraulics of a Plane Free Overfall.” Journal of Hydraulic. Engineering , ASCE, Vol. 109, N° 12, pp. 1683-1697.

Hirt, C.W. and Nichols, B.D. (1981): “Volume of Fluid (VOF) Method for the Dynamics of Free Boundaries”, Journal of Computational Physics, Vol. 39, N°1, pp. 201-225.

Hunt SL, Kadavy KC.(2009): “Inception point relationships for flat-slopped stepped spillways”. ASABE Annual international meeting. Reno, Nevada.

Hunt, S. L., and K. C. Kadavy., (2010a): “Energy dissipation on flat-sloped stepped spillways: Part 1. Upstream of the inception point”. Trans. ASABE, Vol 53, N°1, pp 103-109.

Hunt, S. L., and K. C. Kadavy., (2010b): “Energy dissipation on flat-sloped stepped spillways: Part 2. Downstream of the inception point”. Trans. ASABE, Vol. 53, N°1, pp 111-118

Iman Naderi Rad and Mehdi Teimouri., (2010): “An Investigation of Flow Energy Dissipation in Simple Stepped Spillways by Numerical Model”. European Journal of Scientific Research. ISSN 1450-216X Vol.47 N°4, pp 544-553.

Keller R.J. and Rastogi, A.K (1977): “Design chart for predicting critical point on spillways”. Journal of Hydraulic Division, ASCE, Vol. 103, pp. 1417-1429.

Launder, B.E. and Spalding, D.B., (1974): “The Numerical Computation of Turbulent Flows”, Computer Methods in Applied Mechanics and Engineering, Vol. 3, N°2, pp. 269-289.

Kim, S.E. and D. Choudhury. (1995): “A Near-Wall Treatment Using Wall Functions Sensitized to Pressure Gradient”. In ASME FED 217 ASME.

Mohammad S, Jalal. A and Michael. P, (2012): “Numerical Computation of Inception Point Location for Steeply Sloping Stepped Spillways” 9th International Congress on Civil Engineering, Isfahan University of Technology (IUT), May 8-10,Isfahan, Iran

Menter, F.R., (1993): “Zonal Two Equation k-ω Turbulence Models for Aerodynamic Flows. Proceedings of 24th Fluid Dynamics Conference, 6-9 July, Florida, USA, paper no. AIAA 93-2906.

Ohtsu, I. and Yasuda, Y.(1997): “Characteristics of Flow Conditions on Stepped Channels”. Proc. 27th IAHR Congress, Theme D, San Francisco, USA, pp. 583-588.

Patankar, S. V. (1980):” Numerical Heat Transfer and Fluid Flow”, Hemisphere Publishing Corporation, Taylor & Francis Group, New York. ISBN 0-89116-522-3

Patankar, SV and Spalding, DB (1972): “A calculation procedure for heat, mass and momentum transfer in three-dimensional parabolic flows”. International Journal of Heat and Mass Transfer, 15, 1787.

Peyras, L., Royet, P., and Degoutte, G. (1992): “Flow and Energy Dissipation over Stepped Gabion Weirs.” Journal of Hydraulic Engineering ,ASCE, Vol. 118, N° 5, pp. 707-717.

Rajaratnam, N, (1990): Skimming flow in stepped spillways. Journal of Hydraulic Engineering, ASCE. Vol 116, N°4, pp 587-591.

Roshan, R., Azamathulla, H.M., Marosi, M., Sarkardeh, H., Pahlavan, H. and Ghani, A. A., (2010): “Hydraulics of Stepped Spillways with Different Numbers of Steps”, Dams and Reservoirs, Vol. 20, N° 3, pp. 131-136

Shih, T.H., W.W. Liou., A. Shabbir, Z. Yang and J. Zhu. (1995): “A New $k - \varepsilon$ Eddy-Viscosity Model for High Reynolds Number Turbulent Flow-model development and validation”. NASA Technical Memorandum 106721

Toombes, L., (2002): “Experimental study of air–water flow properties on low-gradient stepped cascades”. Ph.D. Thesis, Department of Civil Engineering, University of Queensland, Brisbane, Australia

Usman. G., (2010): “Investigation of various sediment and flow parameters upon three dimensional flow using numerical model”. PHD Thesis, university of engineering & technology, taxila

Versteeg, H.K. and W. Malalasekera. (2007):” An Introduction to Computational Fluid Dynamics, Finite Volume Method”, 2nd Edition, Pearson Prentice Hall, England. ISBN: 978-0-13-127498-3

Wood, I. R., P. Ackers, and J. Loveless., (1983): “General method for critical point on spillways”. Journal of Hydraulic Engineering ASCE, Vol 109, N°2, pp 308-312

Numerical Simulation of Air Entrainment for Flat-sloped Stepped Spillway

B. Chakib and H. Mohammed

Reprinted from

The Journal of
Computational Multiphase Flows

Volume 7 · Number 1 · 2015

Multi-Science Publishing

Numerical Simulation of Air Entrainment for Flat-sloped Stepped Spillway

Bentalha Chakib* **and Habi Mohammed**
Department of Hydraulic, Faculty of Technology, Abou Bakr Belkaid University,
Tlemcen, Algeria

Received: 29 October 2014, Accepted: 18 January 2015

Abstract

Stepped spillway is a good hydraulic structure for energy dissipation because of the large value of the surface roughness. The performance of the stepped spillway is enhanced with the presence of air that can prevent or reduce the cavitation damage. Chanson developed a method to determine the position of the start of air entrainment called inception point. Within this work the inception point is determined by using fluent computational fluid dynamics (CFD) where the volume of fluid (VOF) model is used as a tool to simulate air-water interaction on the free surface thereby the turbulence closure is derived in the $k-\varepsilon$ turbulence standard model, at the same time one-sixth power law distribution of the velocity profile is verified. Also the pressure contours and velocity vectors at the bed surface are determined. The found numerical results agree well with experimental results.

Keywords: Inception Point, Fluent, VOF Model, Stepped Spillway, Standard k–ε Model.

INTRODUCTION

Stepped spillway is a good hydraulic structure for energy dissipation because of the large value of the surface roughness. Rice and Kadavy [1] found from experiments on a specific model study of a stepped spillway on a 2.5(H):1(V) slope that the energy dissipated with steps was two to three times as great as the energy dissipated with a smooth surface, the studies of Rajaratman [2] and Christodoulou[3] demonstrated also effectiveness the stepped chute for dissipation of kinetic energy, thereby reducing the required size of the stilling basin at the toe of the dam. The compatibility of stepped spillways with roller compacted concrete (RCC) and gabion construction techniques results in low additional cost for the spillway [4].

It is known that the flow over a stepped spillway can be divided into nappe flow regime and skimming flow regime. Nappe flow occurs at low discharge and can be characterized by a succession of free falling nappes. By increasing of discharge, the skimming flow appears and is characterised by highly turbulence and the water flows as a coherent stream.

The performance of the stepped spillway is enhanced with the presence of air that can prevent or reduce the cavitation damage. In the skimming flow regime, air entrainment occurs when the turbulent boundary layer thickness coincides with the water depth [5]. This location is called the inception point (e.g. **Figure 1**). At the inception point upstream, the flow is smooth and glassy whereas at the downstream of the inception point the flow becomes uniform as the depth of the air-water mixture grows.

The inception point of aeration of stepped spillways is placed further upstream than on smooth spillways. On smooth spillway, the location of the inception point is a function of the discharge and the roughness of the spillway. Wood et al. [6] proposed an approach for determining the distance between the spillway crest and the inception point. On stepped spillway, the position of the inception point is a function of the discharge, spillway roughness, step geometry and spillway geometry. Chanson [7, 8] developed a method to determine the position of the start of air entrainment with slopes greater or equal than 22°. Boes and Hager [9] also derived a mathematical formula enabling the determination of the distance between the start of the turbulent boundary layer and the inception point.

---

*Corresponding author: E-mail: c_bentalha@yahoo.fr

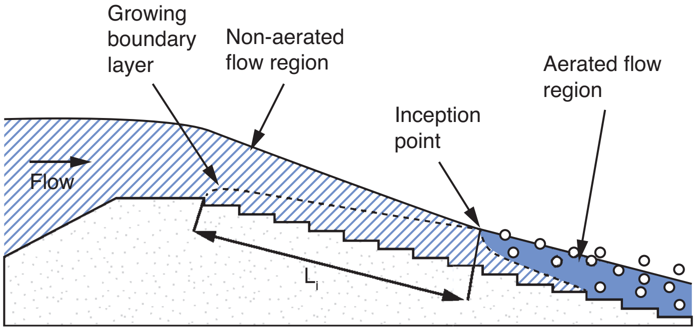

Figure 1: Position of the inception in stepped spillway.

The position of the inception point is important element in determining the energy dissipation. Consequently, this position is a component in the dimensions of the stilling basin. At the downstream of the inception point, the dissipation of energy is very large. Hunt and Kadavy [10] found that the energy dissipation increases linearly from 0 to 30% upstream of the inception point.

The topic of the flow over stepped spillway was the object of several experimental works, with the development of computational fluid dynamics (CFD) branch, flow over stepped spillway can be simulated to validate experimental results. Chen et al.[11], simulated flow over a stepped spillway using the k –ε turbulence model. Benmamar et al.[12] developed a numerical model for the two-dimensional flow boundary layer in a stepped channel with steep slope, which was based on the implicit finite difference scheme. Bombardelli et al.[13] Simulated non-aerated region of the skimming flow in steep stepped spillways using 3D-FLOW. Afshin and Mitra [14], and Cheng et al [15] used FLUENT commercial software for examining the performance of the volume of fluid (VOF) and mixture models in simulating skimming flow over stepped spillway. Iman and Mehdi [16] evaluated energy dissipation in stepped spillways by taking into account parameters such as; number of steps, step height, horizontal step length, characteristic height of the step, flow discharge per unit and overall slope of stepped spillway by numerical method.

In this study, flow over flat-sloped stepped spillway was simulated by using FLUENT software and VOF model was applied to evaluate air-water flow hydraulic characteristics. The aims of this work are to evaluate the effect step height on the position of inception point and to validate the relationships developed by researchers for determining the distance from the spillway crest to the inception point. Also to compare the velocity profile with one-sixth power law distribution and to present pressure contours and velocity vectors at the bed surface. The found numerical results are compared with the existing experimental results [10, 17].

NUMERICAL MODEL

Fluent computational fluid dynamics (CFD) is used to solve Navier-Stokes equations that are based on momentum and mass conservation of multi-phase flow over stepped spillway. Because the standard *k* – ε model is still a good tool for numerical simulation of flow in stepped spillways and verified by experimental and field data [11], it is used to simulate turbulence.

Continuity equation:

$$\frac{\partial \rho}{\partial t}+\frac{\partial \rho u_i}{\partial x_i}=0 \tag{1}$$

Momentum equation:

$$\frac{\partial \rho u_i}{\partial t}+\frac{\partial}{\partial x_j}\left(\rho u_i u_j\right)=-\frac{\partial p}{\partial x_i}+\rho g_i+\frac{\partial}{\partial x_j}\left\{\left(\mu+\mu_t\right)\left(\frac{\partial u_i}{\partial x_j}+\frac{\partial u_j}{\partial x_i}\right)\right\} \tag{2}$$

Turbulence kinetic energy equation (k):

$$\frac{\partial}{\partial t}(\rho k)+\frac{\partial}{\partial x_i}\left(\rho k u_i\right)=\frac{\partial}{\partial x_j}\left[\left(\mu+\frac{\mu_t}{\sigma_k}\right)\frac{\partial k}{\partial x_i}\right]+G_k-\rho\varepsilon \tag{3}$$

Turbulence dissipation rate energy equation (ε):

$$\frac{\partial}{\partial t}(\rho\varepsilon)+\frac{\partial}{\partial x_i}(\rho\varepsilon u_i)=\frac{\partial}{\partial x_j}\left[\left(\mu+\frac{\mu_t}{\sigma_\varepsilon}\right)\frac{\partial\varepsilon}{\partial x_i}\right]+C_{\varepsilon 1}\frac{\varepsilon}{k}G_k-C_{\varepsilon 2}\rho\frac{\varepsilon^2}{k} \tag{4}$$

Where, G_k is production of turbulent kinetic energy which can be given as

$$G_k=\mu_t\left(\frac{\partial u_i}{\partial x_j}+\frac{\partial u_j}{\partial x_i}\right)\frac{\partial u_i}{\partial x_j} \tag{5}$$

μ_t is the turbulent viscosity that satisfies

$$\mu_t=\rho C_\mu\frac{k^2}{\varepsilon} \tag{6}$$

$C_\mu = 0.09$ is a constant determined experimentally;
σ_k and σ_ε are turbulence Prandtl numbers for k and ε equation respectively, $\sigma_k = 1.0$, $\sigma_\varepsilon = 1.3$,
$C_{1\varepsilon}$ and $C_{2\varepsilon}$ are ε equation constants, $C_{1\varepsilon} = 1.44$, $C_{2\varepsilon} = 1.92$.

The volume of fluid (VOF) method is applied to simulate the free surface between water and air [18]. In this approach, the tracking interface between air and water is accomplished by the solution of a continuity equation for the volume fraction of water:

$$\frac{\partial\alpha_w}{\partial t}+\frac{\partial\alpha_w u_i}{\partial x_i}=0;\ 0\le\alpha_w\le 1 \tag{7}$$

Where, α_w is volume fraction of water.

In each cell, the sum of the volume fractions of air and water is unity. So, volume fractions of air denote α_a can be given as

$$\alpha_a=1-\alpha_w \tag{8}$$

The geometry of numerical model and boundary conditions are shown in figure 2. The channel was 10.8 m long and 1.5 m vertical drop. The channel slope is 14°. The stepped spillway contains 40 steps with 38 mm height and 152mm length by step for case 1. In the second case the stepped spillway contains 20 steps with 76 mm height and 304mm length by step. For the last case the stepped spillway contains 10 steps with 152mm height and 608mm length by step. For each case studied, the two-dimensional numerical domain was discretised into structured grid with size of 0.01×0.01 m^2. The boundary conditions in this study are pressure inlet as water inlet and air inlet, outlet as a pressure outlet type. All of the walls as a stationary, no-slip wall. The viscosity layer near to the wall dealt with the standard wall function. The boundary conditions for the turbulent quantities such as k and ε can be calculated from [18]:

$$k=\frac{3}{2}\left(U_{avg}I\right)^2 \tag{9}$$

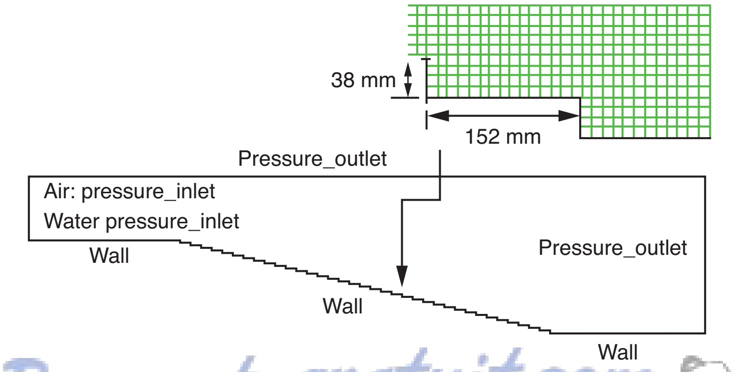

Figure 2: Boundary conditions and numerical model of a stepped spillway.

$$\varepsilon = C_u^{3/4} \frac{k^{3/2}}{0.07 D_H} \tag{10}$$

Where, I is turbulence intensity can be estimated from the following formula derived from an empirical correlation for pipe flows:

$$I = 0.16\left(\mathrm{Re}_{DH}\right)^{-1/8} \tag{11}$$

U_{avg} is the mean velocity of water flow inlet and D_H is the hydraulic diameter.

In this study, several positions of the inception point are computed and compared with the existing experimental results [17] as well as with those predicted by the formula of Chanson [7,8]. The latter is a function of unit discharge, gravitation acceleration, channel slope ($\theta \geq 22°$) and step height:

$$L_{i^*} = 9.719\left(\sin\theta\right)^{0.0796}\left(F_*\right)^{0.713}\mathrm{k_s} \tag{12}$$

Where:
L_{i*} = distance from the crest spillway to the inception point
$k_s = h\ cos\theta$
h = step height
θ = channel slope
F* = Froude number defined in terms of the roughness height:
$F^* = q/[g(\sin\theta)\{k_s\}^3]^{0.5}$
q = unit discharge
g = gravitational constant

RESULTS AND DISCUSSION

Figure 3 presents a comparison the air entrainment simulated by VOF model and in experiments for unit discharge equal to 0.28m^2/s with step heights are 38 mm, 76 mm and 158 mm. As can be seen from this figure, the calculated inception point is well agreed with that of measurement. At the inception point, the degree of turbulence was large enough to entrain air into the black water flow [15], and then the volume fraction of water becomes less than unity. The inception point can be determined by the comparison between the variation of water flow depth and boundary layer thickness [13]. This figure shows that the step heights increases, the inception point was noted to move further upstream of the spillway crest.

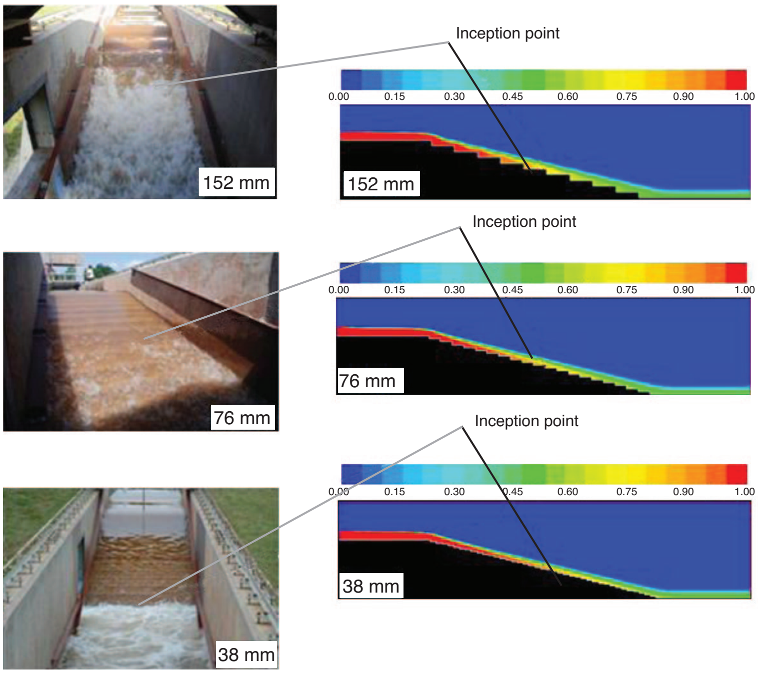

Figure 3: Measured and computed inception point for q = 0.28m^2/s.

The results of numerical computation volume fraction of water over stepped spillway for different discharges were depicted in Figure 4. This figure indicates that the inception point moves toward the basin floor when the discharge increases. At lower discharges, the inception point was more defined than at higher discharges because in high discharges, the boundary layer cannot reach the free surface at little distances, and the non-aerated region dominates large portions of the flow in the spillway.

Table 1 summarises the position of the inception point found by Hunt and Kadavy [17], Chanson[7,8] and by using fluent, for unit discharge equal to 0.11, 0.20, 0.28, 0.42, 0.62, 0.82 m^2/s.

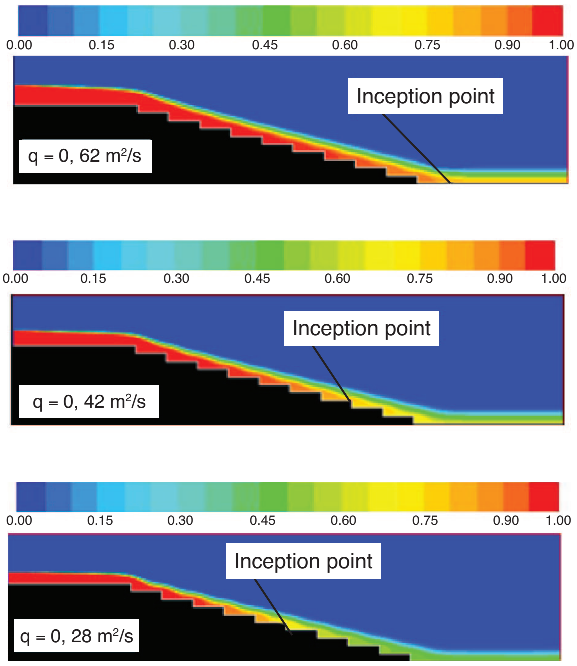

Figure 4: Numerical computation volume fraction of water for different discharges.

Table 1. Observed, calculated and computed inception point location

q	h		Hunt and kadavy [17]	Chanson [7,8]	Computed inception point
(m^2/s)	(mm)	F_*	L_i (m)	L_{i*}(m)	L_{i**} (m)
0.82	38	75.2	7.1	7.0	No air entrainment
0.62	38	56.3	6.6	5.7	6.4
0.42	38	38.3	4.6	4.3	4.4
0.28	38	25.7	3.5	3.2	3.3
0.20	38	18.6	2.7	2.6	2.5
0.11	38	9.8	1.4	1.7	1.3
0.82	76	26.3	6.28	6.61	6.5
0.62	76	19.9	5.32	5.41	5.7
0.42	76	13.5	3.76	4.12	4.1
0.28	76	9.1	2.82	3.11	3.1
0.20	76	6.6	1.87	2.47	2.1
0.11	76	3.5	1.09	1.55	1.3
0.82	152	9.4	5.62	6.34	6.1
0.62	152	7.1	4.39	5.17	4.9
0.42	152	4.8	3.12	3.94	3.7
0.28	152	3.2	2.20	2.94	2.50
0.20	152	2.3	1.57	2.36	1.9
0.11	152	1.2	0.94	1.48	1.1

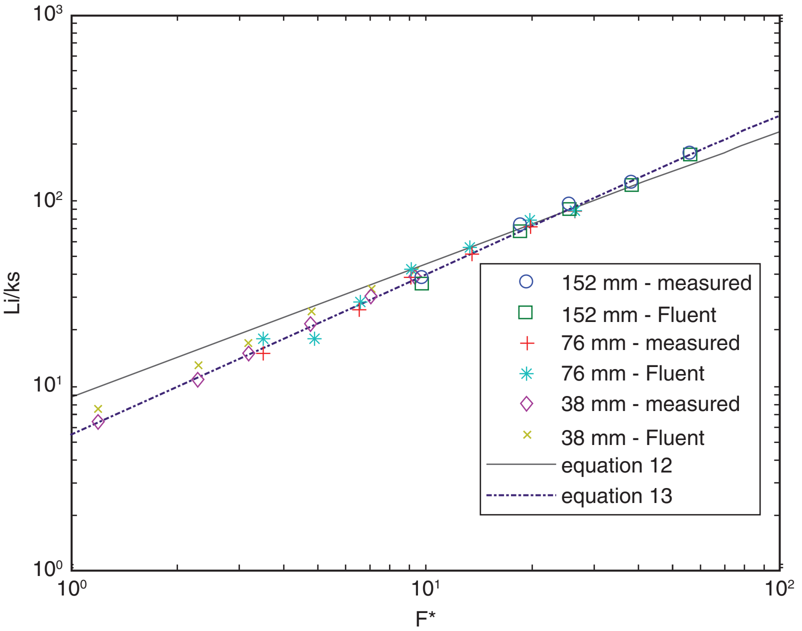

Figure 5: Normalized L_i versus Froude surface roughness, F_*.

In Table 1 and Figure 5 the comparison of computed inception point with those from experimental equation of chanson and observed by Hunt and Kadavy [17] is presented. Table 1 and Figure 5 show good agreement between the observed and computed inception point locations. As can be seen from this table, by increasing of the step heights, the difference between calculated inception point and computed inception, and measured inception point also increased. Figure 5 illustrates that Chanson's relationship appears to more closely predict the distance from the crest to the inception point when Froude surface roughness (F*) ranging from 10 to 100 correspond to step heights of 38 mm and 76 mm. Hunt and Kadavy [17] proposed new relationships for determining the inception point for F_* ranging from 1 to 100 with slopes little or equal than 22°. This formula was plotted in figure 5:

$$L_{i^*} = 6.1(\sin\theta)^{0.08}(F_*)^{0.86}k_s \tag{13}$$

In Figure 6 numerically-derived air concentration distribution at the 20th step edge for h = 38 mm is presented. It is clear that by increasing discharge, bottom and mean air concentration decreases.

The velocity distribution in stepped spillway is shown in figure 7. The velocity is higher in aerated region because the entrained air reduces wall friction; also the fluid is accelerated by the gravity along the chute. The recirculation flow which dissipates the energy in step corner is presented in figure 8. Most of the energy is dissipated by momentum transfer between the skimming flow and the eddy in the interior of the step.

The pressure distributions down the steps are important to study the risk of cavitation in stepped channel; figure 9 illustrates the contours of pressure in step corner. This figure indicate that the minimum value of pressure is located in the vertical wall of the step, is due by separation flow between skimming flow and the eddy in this region. Also maximum pressure exists in the horizontal surface of the step. This maximum pressure is caused by the impact of the skimming flow coming from upper step.

In figure 10, the one sixth power law with velocity was compared by velocity profiles obtained with fluent and the experimental velocity profiles measured by Hunt and Kadavy 10] at different distances from spillway crest 0.0, 1.22 and 3.05m respectively for $q = 0.28m^2/s$. This figure shows good agreement between experiments and simulations. The velocity profiles are uniform at the crest and trend toward a one sixth power law distribution near the inception point. Chanson [8]

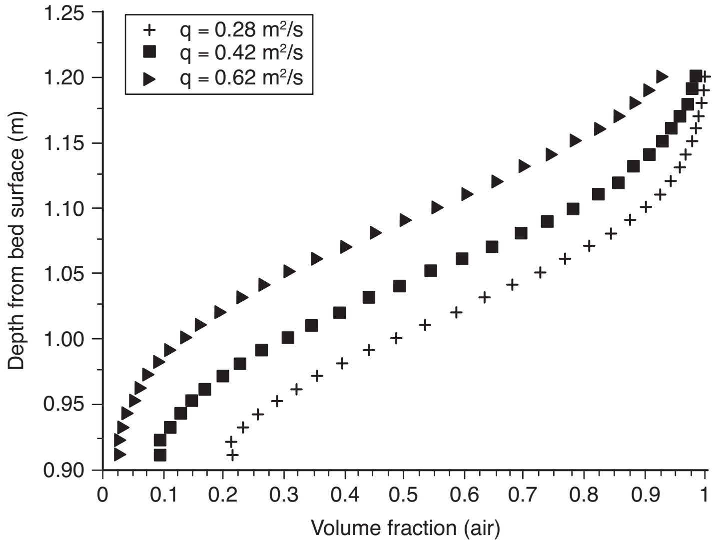

Figure 6: Computed air concentration for different discharge.

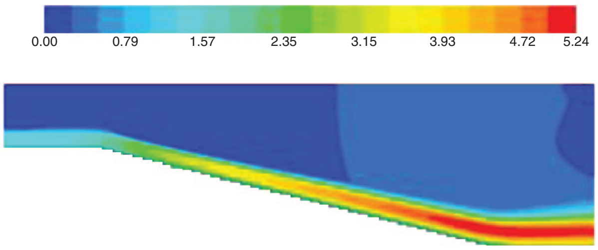

Figure 7: Velocity distribution along the stepped spillway for q = 0.28m^2/s and h = 38 mm.

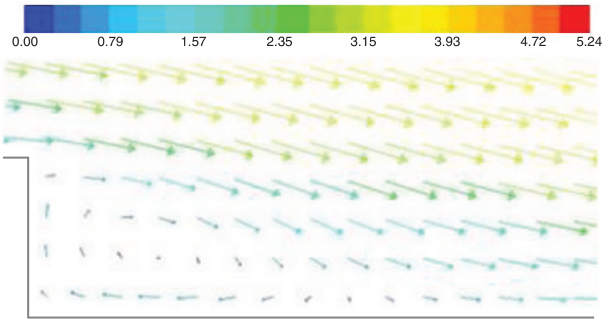

Figure 8: Velocity vectors on one step for q = 0.28m^2/s and h = 38 mm.

found from experiments that the velocity profiles tended to follow a one-sixth power law distribution:

$$\frac{V}{V_{\max}} = \left(\frac{y}{\delta}\right)^{1/6} \quad 0 \le y/\delta \le 1 \tag{14}$$

Where V$_{\max}$ is the free-stream velocity; *y* is the transverse coordinate originating at the pseudo-bottom and δ is the boundary layer thickness defined as the perpendicular distance from the pseudo-bottom to the point where the velocity is 0.99 V$_{\max}$.

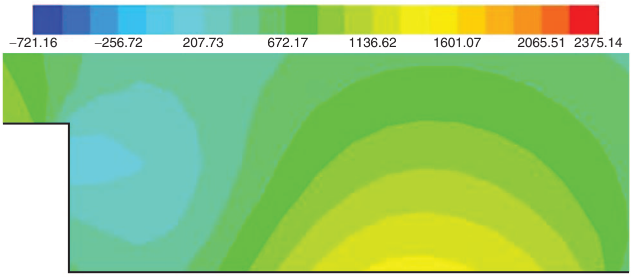

Figure 9: Pressure contours on one step for q = 0.28m^2/s and h = 38 mm.

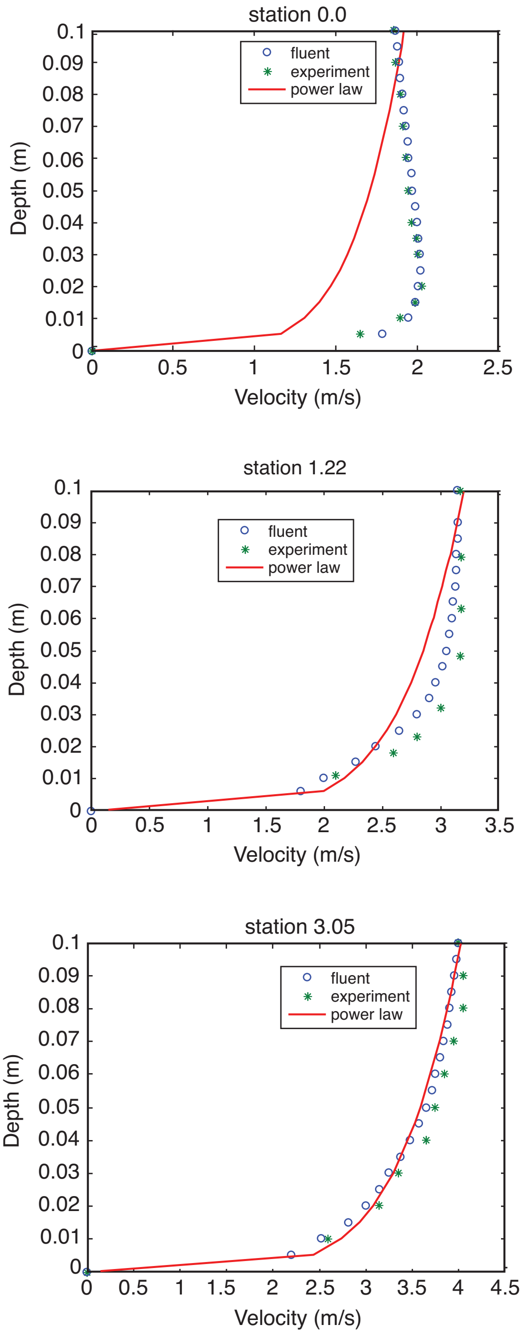

Figure 10: Comparison of the one sixth power law with a Velocity obtained by simulation and measurement in Hunt and Kadavy, for q = 0.28 m^2/s and h = 38 mm.

CONCLUSION

In the present numerical study, flow over flat sloped stepped spillway was simulated by using fluent. Free surface was treated by VOF model and turbulence flow was estimated by k-ε Standard Model. Good agreement is found between numerical and experimental results. It was found that the inception point moves toward the basin floor when the discharge increases and that the step height decreases. This study proved that the formula developed by Chanson [7,8] can be used to determine the location of the inception point on stepped chute with Froude surface roughness (F*) ranging from 10 to 100. It has been verified that the velocity profile obey the one sixth power law distribution near the inception point. Minimum and maximum pressure is located in the vertical and horizontal face of step.

Lastly, the findings from this paper are an indication that the FLUENT software is powerful tool to simulate the air-water flow and to help in the design of stepped spillway together with the physical model.

REFERENCES

[1] Charles E.Rice and Kem C.Kadavy., Model of A roller compacted concrete stepped spillway. *Journal of Hydraulic Engineering, ASCE*, 1996, 122(6), 292–297.

[2] Rajaratnam, N., Skimming flow in stepped spillways. *Journal of Hydraulic Engineering, ASCE,*1990, 116 (4), 587–591.

[3] Christodoulou,G.C., Energy dissipation on stepped spillways. *Journal of Hydraulic Engineering, ASCE*, 1993, 119 (5), 644–650.

[4] CHANSON, H., Stepped Spillway Flows and Air Entrainment. *Canadian Journal of Civil Engineering*, 1993, 20(3), 422–435 (ISSN 0315–1468).

[5] Chanson. H., *Air Bubble Entrainment in Free-Surface Turbulent Shear Flows. Academic Press, London, UK*, 1997, 401 pages ISBN 0-12-168110-6.

[6] Wood, I. R., P. Ackers, and J. Loveless., General method for critical point on spillways. *Journal of Hydraulic Engineering ASCE*, 1983, 109(2), 308–312

[7] Chanson, H, Hydraulics of skimming flows over stepped channels and spillways. IAHR, *Journal of Hydraulic Research.,* 1994, 32(3), 445–460.

[8] Chanson H., *The hydraulics of stepped chutes and spillways. Balkema* Publisher,2002, ISBN 90 5809 352 2, 384 pages.

[9] Boes, R. M. and W. H. Hager., Two-phase flow characteristics of stepped spillways, 2003, *Journal of Hydraulic Engineering, ASCE*, 129(9):661–670.

[10] Hunt, S. L., and K. C. Kadavy., Energy dissipation on flat-sloped stepped spillways: Part 1. Upstream of the inception point, *Trans. ASABE, 2010,* 53(1): 103–109.

[11] Chen, Q., G.Q. Dai and H.W. Liu., Volume of Fluid Model for Turbulence Numerical Simulation of Stepped Spillway Over Flow, *Journal of Hydraulic Engineering, ASCE, 2002,* 128 (7), 683–688.

[12] Benmamar, S. Kettab, A. and Thirriot, C., Numerical simulation of turbulent flow upstream of the inception point in a stepped channel. *Proceedings, 30th IAHR Congress*. Auth, Thessaloniki, Greece, 2003, 679–686.

[13] Bombardelli FA, Meireles I, Matos J, Laboratory measurements and multi-block numerical simulations of the mean flow and turbulence in the non-aerated skimming flow region of steep stepped spillways. *Environ. Fluid Mech,, 2010,* 11(3), 263–288.

[14] Afshin Eghbalzadeh and Mitra Javan, Comparison of Mixture and VOF Models for Numerical Simulation of Air–entrainment in Skimming Flow over Stepped Spillways *,J. of Science Direct. Procedia engineering, 2012, (28) 657–66.*

[15] CHENG Xiangju, CHEN Yongcan and LUO Lin,, Numerical simulation of air-water two-phase flow over stepped spillways. *Science in China Series E, Technological Sciences*, 2006, 49 (6), 674–684

[16] Iman Naderi Rad and Mehdi Teimouri., An Investigation of Flow Energy Dissipation in Simple Stepped Spillways by Numerical Model, *European Journal of Scientific Research*, 2010, ISSN 1450-216X Vol.47 No.4:544–553.

[17] Hunt SL, Kadavy KC., Inception point relationships for flat-slopped stepped spillways, *American Society of Agricultural and Biological Engineers Annual International meeting, 2009, N0 096571*

[18] Fluent, Manuel and user guide, Fluent Inc, 2006.

ملخص

إن قناة تصريف الفائض الذي يتشكل سطحه من مدرجات هو عبارة عن منشأ هيدروليكي جيد لتبديد الطاقة نظرا لخشونة السطح. أهمية هذه القناة كذلك تكمن أنه يساعد على دخول الهواء إلى الماء مم يقلل من مخاطر التجويف. الباحث Chanson وضع معادلة تسمح بتحديد نقطة بداية التهوية.

الهدف من هذا البحث هو استعمال نماذج عددية للتحقق من صحة محاكاة جريان السائل على نوعين من القناة: الأول يتشكل سطحه من مدرجات ذو ارتفاع ثابت و الثاني يتشكل سطحه من مدرجات ذو ارتفاع متغير.

في هذا العمل تم تحديد نقطة بداية التهوية و طبيعة جريان السوائل باستعمال البرنامج دينامكية ميكانيكا الموائع الحسابية " FLUENT " . استخدم في هذا العمل النموذج متعدد الأطوار " VOF " لتحديد التفاعل بين الماء والهواء و كذلك النموذج "k–ε" المتعلق بالحركة المضطربة لإغلاق نظام المعادلات، وفي الوقت نفسه تم التعريف بقانون تغير السرعة و قانون توزع الهواء إضافة إلى ملامح الضغط و دوران أشعة السرعة على سطح الدرج. النتائج الرقمية ملائمة للنتائج التجريبية.

مفتاح الكلمات: جريان السائل، نقطة بداية التهويه، البرنامج " Fluent "، النموذج " VOF "،النموذج "k–ε" ، السطح المدرج

Résumé

Le déversoir en marche escalier est un bon structure hydraulique pour la dissipation de l'énergie en raison de la grande valeur de la rugosité de surface. La performance du déversoir en marche escalier réside dans la présence d'air qui peut prévenir ou réduire la cavitation. Chanson a développé une méthode permettant de déterminer la position du début de l'entraînement d'air. Cette position est appelée le point d'inception.

L'objective de cette recherche est d'utiliser les modèles numériques pour valider la simulation d'écoulement sur deux types de déversoirs en marche escalier avec deux sortes de marches à savoir une marche dont la hauteur est uniforme et une marche dont la hauteur est non uniforme.

Dans ce travail, le point d'inception et les régimes d'écoulement sont déterminées à l'aide de logiciel FLUENT (CFD). Le modèle multiphasique VOF (Volume Of Fluid) est utilisé comme outil pour modéliser l'interaction eau-air prés de la surface libre et le modèle (k-ε) est utilisé pour fermer le système d'équation, en même temps la loi du profil de vitesse et la distribution de concentration d'air sont définies. De plus les contours de pression et vecteurs de vitesse au creux des marches sont présentés. Les résultats trouvés numériquement sont en bon accord avec les résultats expérimentaux.

Mots clés : Régimes d'écoulement, Point d'inception, Fluent, méthode VOF, marche escalier, modèle (k-ε)

Abstract

Stepped spillway is a good hydraulic structure for energy dissipation because of the large value of the surface roughness. The performance of the stepped spillway is enhanced with the presence of air that can prevent or reduce the cavitation damage. Chanson developed a method to determine the position of the start of air entrainment called inception point.

The aim of this research is to use a numerical model to validate the simulation of flow over two types of stepped spillway which are : uniform step height and non uniform step height.

Within this work the inception point and flow regimes are determined by using fluent computational fluid dynamics (CFD) where the volume of fluid (VOF) model is used as a tool to simulate air-water interaction on the free surface thereby the turbulence closure is derived in the $k-\varepsilon$ turbulence standard model, at the same time the law of velocity profile and air concentration distribution are defined. Also the pressure contours and velocity vectors at the bed surface are determined. The found numerical results agree well with experimental results.

Keywords: Flow regimes, Inception Point, Fluent, VOF Model, Stepped Spillway, Standard $k-\varepsilon$ Model.